Petrographic, whole-rock geochemical and $\delta^{34}S$ study of the Neoarchaean Black Reef at the Carletonville Goldfield, South Africa: Implications for fluid circulation and Au mobilisation

By

Hunadi Kebone Pelican Maselela

A dissertation submitted to the

Faculty of Science, University of the Witwatersrand

in fulfilment of the requirements for the degree of

Master of Science

School of Geoscience

2021

UNIVERSITY OF THE
WITWATERSRAND,
JOHANNESBURG

Declaration

I declare that this dissertation is my own, unaided work. It is being submitted for the Degree of Master of Science at the University of the Witwatersrand, Johannesburg. It has not been submitted before for any degree or examination in any other university.

Hunadi Kebone Pelican Maselela: Maselela

30 March 2021, at the **University of the Witwatersrand, Johannesburg**.

Abstract

Globally, gold-bearing quartz-pebble conglomerate known as “Witwatersrand-type”, owing their name to the Witwatersrand Basin gold province, occur throughout space and time. In South Africa, outside the Witwatersrand stratigraphy, two examples of the Witwatersrand-type gold deposits exist, namely, the Ventersdorp Contact Reef (VCR) and the Black Reef Formation. The Neoarchaean Black Reef Formation hosts the youngest gold-bearing reef on the Kaapvaal Craton and is mined with some Witwatersrand reefs in the Carletonville goldfield. Presently, little is known about the gold mineralisation mechanism/s in the Black Reef, specifically related to how gold was introduced and why the mineralisation is poorly developed in this part of the stratigraphy. To address these problems, this study uses a combination of petrography, geochemistry, fluid inclusions and S-isotope analyses from four drill cores that intersect the Black Reef in the Carletonville goldfield.

There are three main lithologies sampled from the Black Reef in this study: hanging wall carbonaceous shale, footwall quartz arenite and gold-bearing conglomerate commonly referred to as “reef”. The shale units contain a high abundance of total organic carbon, hence the name carbonaceous, and are generally unmineralised with gold. Some parts of these carbonaceous shale units contain graphite, and are embedded with highly fractured quartz-pebbles and authigenic pyrite and contain Au concentration of 1 g/t. They contain relatively high Cr and Ni contents, suggesting that their provenance may be related to mafic lithologies such as the Ventersdorp Supergroup lavas and/or mafic units of greenstone terranes. Quartz arenite units are generally low- to moderately-mineralised with gold (up to 2 g/t Au) but may contain high degrees of pyrite mineralisation (up to 15 % modal abundance) aligned as stringers at bedding foresets and cross-beds. Conglomerate units contain 2 – 28 g/t gold and host significant pyrite mineralisation (up to 30% modal abundance). They are described as well sorted and moderately packed. The matrix of these conglomerate units contain gold- and uranium-bearing, complex-shaped carbon nodules that are also located in some quartz fractures. Quartz arenite and conglomerate units contain Zr contents ($\bar{x}$ = 69.42 ± 16.10 ppm and $\bar{x}$ = 137.73 ± 85.55 ppm, respectively), Cr contents ($\bar{x}$ = 140.45 ± 151.85 ppm and $\bar{x}$ = 201.41 ± 117.33 ppm, respectively) and Al_2O_3/TiO_2 ratios similar to those of various felsic Archean rocks on the Kaapvaal Craton and the underlying sedimentary rocks of the Witwatersrand Supergroup.

The Black Reef contains carbonaceous material in the form of pyrobitumen, which is divided into four types: globular, nodular, irregular and fracture filling. The former three types are sub-rounded and complex shaped. The difference is that the globular and irregular pyrobitumen contain inclusions of gold and uranium while the nodular is massive. The irregular type is often surrounded by pyrite grains. Based on texture and morphology, five different grouping of pyrite are observed: massive detrital pyrite (DM), random inclusion-bearing detrital pyrite (DIR), concentrically laminated detrital pyrite (DIC), euhedral / subhedral authigenic pyrite (AE) and authigenic pyrite overgrowth (AO). The mean whole-rock $\delta^{34}S$ values of carbonaceous shale is 3.20 ‰ and 3.13 ‰ for conglomerate. These values coincide with $\delta^{34}S$ values from pyrite grains sourced from the VCR and Witwatersrand reefs. Gold is commonly located at boundaries of pyrite grains and occurs as irregular-shaped phases in quartz-pebble fractures. Microthermometry analysis showed two-phase Type I fluid inclusions (3:2 liquid to vapour ratio), two-phase Type II fluid inclusions (2:3 liquid to vapour ratio), monophase Type II fluid inclusions (one liquid phase) and three-phase Type IV inclusions. The mean entrapment temperature is 172 ± 30 ^{o}C with a low and medium salinity clusters. The composition of the fluids is aqueous, H_2O-CO_2, H_2O-CO_2-CH_4 and H_2O-H_2S-CH_4.

The presence of DIC pyrite indicates that they are sourced from the Witwatersrand reefs and the VCR. The VCR and Witwatersrand reefs contain the most of these concretionary pyrite grains, and their fractured nature in the Black Reef provides evidence for a source outside the Transvaal Basin by mechanical recycling, with a short distance travel for them to preserve their laminate texture. The detrital pyrite grains are also indicative of provenance from a local source, some containing inclusions of gold. The overlap of $\delta^{34}S$ values from whole-rock Black Reef samples with those obtained from previous studies on the Witwatersrand reefs and the VCR suggests that the Black Reef pyrite grains are locally sourced by mechanical recycling of pyrite grains from these precursors. Authigenic pyrite and pyrite overgrowths evoke the presence of hydrothermal fluids that entered the Black Reef Formation. Therefore, it is concluded that Black Reef sediments, pyrite and gold are locally sourced from the underlying strata by mechanical reworking of these sources. Hydrothermal fluids formed from prograde metamorphism due the emplacement of the Bushveld Igneous Complex and the Vredefort meteorite impact event. Previously reworked gold was dissolved in hydrothermal fluids containing H_2S derived from a volcanically active atmosphere and transported as $Au(HS)_2^-$ through fractures, faults and unconformities at the timing of the Vredefort meteorite impact event. Gold was chemically precipitated by reduction when sulphidation of iron-bearing rocks occurred, consuming the reduced sulphur causing pyritization, and precipitated hydrothermal gold at pyrite grain boundaries and trapped native gold in quartz fractures to further distances.

Dedicated to my parents:

My prayer warrior mother, Mavis Maselela

My supportive father, Lazarus Maselela

for encouraging me to further my studies and supporting me to be the best version of me

Acknowledgements

I would like to express my sincere gratitude to my supervisors, Dr. Glen Nwaila and Dr. Grant Bybee for their scientific expertise, tremendous amount of patience and understanding, and for their guidance throughout the duration of my MSc study. I am particularly appreciative to Glen who never gave up on me, uplifted and supported me, checked up on me when the student in me gave up, and who seemingly enjoyed challenging me every time I thought I have cracked the code. I am truly grateful. I thank you. I am honoured to have worked with both Grant and Glen who possess broad knowledge and skills in major aspects of geochemistry and economic geology, respectively.

I acknowledge the financial support from the DST-NRF Centre of Excellence for Integrated Mineral and Energy Resource Analysis (DST-NRF CIMERA) towards this research. Johan van Eeden from Sibanye Stillwater Ltd. is also acknowledged for providing the drill holes and Au assay data for the samples used in this study.

Sincere gratitude also goes out to the technicians from various laboratories who helped with sample preparation and conducting the various analyses: Bab Caiphus Majola and Bab Sam Tshabalala for making the thin sections, Marlin Patchappa for XRF and ICP-MS analysis, Dr Sabine Varryn for XRD analysis, Brayner with BSE and SEM analysis, Prof. Rudolph Erasmus for assistance with Raman spectroscopy, Prof. Gill Drennan and Priyal Daya for training me for fluid inclusion studies. Steven Zhang is thanked for assistance with constructing the δ^{34}S isotope figures and Julie Bourdeau is thanked for proofreading the thesis.

Special thanks go to my family: uncles, aunt and grandmother, who did not stop to remind me to rest and get enough sleep and encouraged me to always work hard. Of course, I would like to thank my friends and old classmates who were there to provide much-needed breaks when the going was getting tough, and for always encouraging me and debating with me on aspects of this study. Thank you for always encouraging me and motivating me to endure the hardships of my project and finish my degree.

Lastly, no words can describe the gratitude I have towards my mom and dad. This Master’s degree is dedicated to you since there is nothing more you wanted for me than being an educated, young, black woman. Thank you for your undying love, support, patience and motivation that “funda mntanam', kuzolunga”. I thank you and I love you.

Conference presentations and peer reviewed papers

Conference presentations

Nwaila, G. T., **Maselela, H. K.**, Khumalo, T., Bybee, G. M., Manzi, M. S. D., Durrheim, R. J. and Kirk, J. (2018) Evidence of local sourcing of gold and pyrite in the Black reef Formation of the Transvaal Supergroup, South Africa. In Abstracts: *Geocongress 2018*: University of Johannesburg, Biennial Congress of the Geological Society of South Africa, pp. 155

Maselela, H. K., Nwaila, G. T., Bybee, G. M., Durrheim, R. J. and Lehmann, J. (2019) New constraints on fluid composition of the Neoarchaean Black Reef, South Africa. *15th SGA Biennial Meeting 2019 – Life with Ore Deposits on Earth*, (2)

Peer reviewed papers

Nwaila, G. T., Manzi, M. S. D., Kirk, J., **Maselela, H. K.**, Durrheim, R. J., Rose, D. H., Nwaila, P. C., Bam, L. C. and Khumalo, T. (2019) Recycling of paleoplacer gold through mechanical and postdepositional mobilization in the Neoarchean Black Reef Formation, South Africa. *The Journal of Geology*. **127**, pp. 137 – 166

Nwaila, G. T., Durrheim, R. J., Jolayemi, O. O., **Maselela, H. K.**, Jakaite, L. and Burnett, M. (2020) Significance of granite-greenstone terranes in the formation of Witwatersrand-type gold mineralisation – a case study of the Neoarchaean Black Reef Formation, South Africa. *Ore Geology Reviews*. **121**, 19 pp.

Table of contents

Glossary

- Bitumen: sticky, black, highly viscous liquid or semi-solid form of petroleum; similar to a hydrocarbon
- Carbonaceous material: organic matter like coal or containing carbon – refers to the products of diagenetic and low temperature metamorphic coalification processes normally found in shale rocks
- Conglomeratic shale: carbonaceous shale with scattered quartz-pebbles that have fracture-filling pyrobitumen
- Graphite: pure, crystalline carbon transformed by high temperature metamorphism of non-crystalline carbonaceous material. Black with a dark grey/black streak
- Hydrocarbons: materials that contain H-C bonds, formed from source rocks with >5 % organic matter by weight
- Organic matter: >3 % of organic carbon in a sediment
- Pyrobitumen – solidified bitumen

List of equations

Equation 1: $Au_s + 2HS + H + /_4\ O_2 \rightleftharpoons Au(HS)_2 + /_2\ H_2O$

Equation 2: $4Au_s + 8SO_4^{2-} + 12H^+ \rightleftharpoons 4Au(HS)_2^- + 15O_2 + 2H_2O$

List of figures

List of tables

Chapter 1: Background

1.1 Introduction

The Witwatersrand Basin is the world's largest gold province and an estimated ~30 % of global gold production has been derived from palaeoplacer deposits (Frimmel and Minter, 2002; Frimmel, 2014; Tucker et al., 2016; Frimmel, 2018). The most exploited reefs have been the Carbon Leader and Main Leader reefs with ore grades between 20 and 40 g/t gold, followed by the Basal and Steyn reefs with 19 g/t and the Ventersdorp Contact Reef mined at 5 – 12 g/t (Frimmel, 2018). There has been considerable controversy over the origin of gold and the model for gold concentration in the Witwatersrand Basin because it contains features of both detrital and epigenetic mineralisation. Arguments for and against a palaeoplacer introduction of gold model with a later localised hydrothermal enrichment have been proposed by Robb and Meyer (1995), Frimmel (1997), Frimmel (2005, 2014), Frimmel et al. (2005) and Tucker et al. (2016) while arguments for a purely epigenetic formation by hydrothermal introduction of gold has been suggested by Barnicoat et al. (1997), Law and Phillips (2005) and Phillips and Powell (2011). Gold mining in South Africa has decreased over the past three decades because of energy and labour costs required to reach distal deposits, insufficient room for mechanised mining at kilometre depths and unsafe working environments for employees at those depths (Frimmel et al., 2005). These issues have given rise to studying alternative gold deposits that may have the potential for future gold mining. The base of the Palaeoproterozoic (2670 – 2100 Ma) Transvaal Supergroup is comprised of the 2618 ± 11 Ma Black Reef Formation (Els et al., 1995; Frimmel, 1997; Henry and Master, 2008; Zeh et al., 2020). It hosts an insignificant amount of gold compared to the Witwatersrand reefs, and its mineralisation is erratically developed with the average gold grades as low as 2 – 4 g/t (Sharpe, 1949; Henry and Master, 2008; Frimmel, 2018).

Significant quartz-pebble conglomerate gold occurrences around the world (Fig. 1.1), such as Witwatersrand in South Africa, Tarkwa in Ghana, Jacobina and Moeda in Brazil, Roraima in South America, Blind River-Elliot Lake in Canada, Hamersley in Australia and Bababudan in India show similar features (Frimmel, 2014; Taylor and Anderson, 2018). These features include the presence of iron-bearing phases such as pyrite and iron formations, presence of uranium and/or rarely hydrocarbon, a likely Archaean granite-greenstone source and formation in a foreland basin. Noticeable features of most Meso- to Neoarchaean (~3000 – 2500 Ma) gold- and uranium-bearing conglomeratic horizons is the presence of iron minerals such as abundant pyrite grains of various morphologies (Frimmel and Minter, 2002; Barton and Hallbauer, 1996). The Black Reef is no different and shows compact rounded, round concretionary, rounded porous and recrystallised authigenic pyrite morphologies (Barton and Hallbauer, 1996). These pyrite grains have been interpreted as an indication for either detrital or synsedimentary provenance because of their association with gold (Barton and Hallbauer, 1996; Agangi et al., 2013). High concentrations of gold and uranium are associated with these pyrite grains alongside rounded carbonaceous nodules (Agangi et al., 2013; Agangi et al., 2015). In the Black Reef Formation, gold mineralisation occurs in the conglomerate units and these units are regarded as the youngest gold-bearing reefs mined in most Witwatersrand goldfields (Law and Phillips, 2006; Pearton and Viljoen, 2017).

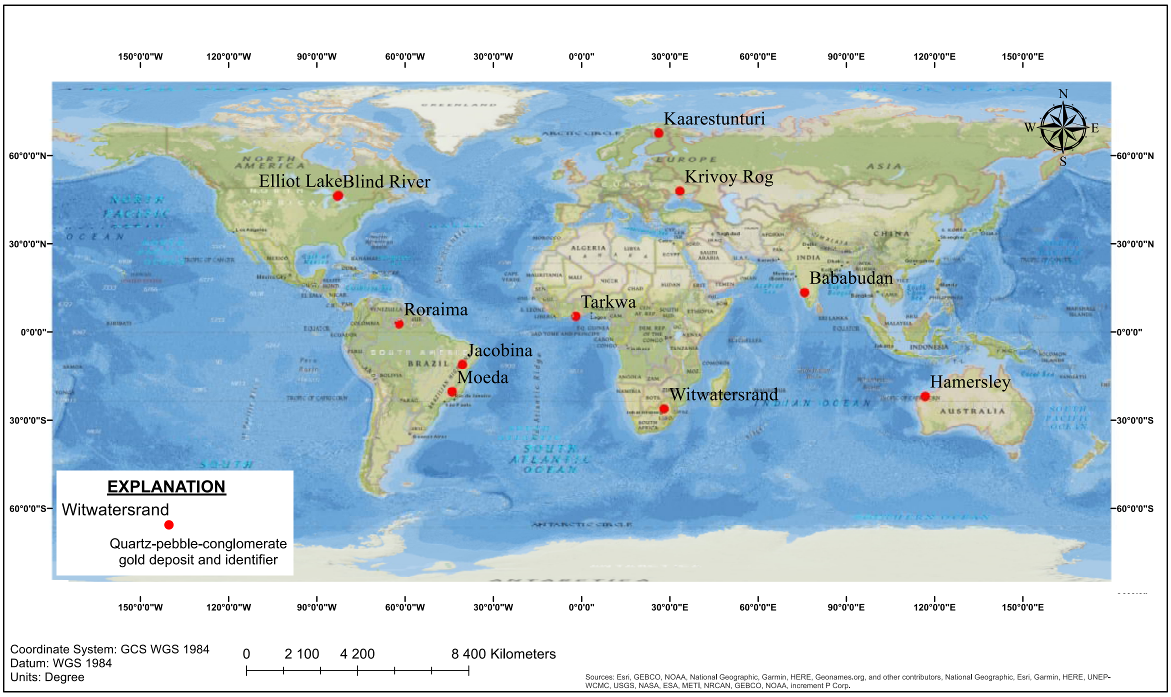

Figure 1.1: Global distribution of major quartz-pebble conglomerate gold deposits. The basin with the highest gold production is the Witwatersrand followed by Tarkwa, Jacobina, Moeda, Elliot Lake, Bababudan, Roraima, Hamersley and lastly Kaarestunturi as a prospect. Modified from Taylor and Anderson (2018).

Most literature on the Witwatersrand gold mentions the Black Reef gold deposit without much focus on its metallogenic processes. Except for a recent metallogenic study by Fuchs et al. (2016), there is little detailed literature for the gold mineralisation of the Black Reef. Mineralogically, the Neoarchaean Black Reef is similar to the gold-, uranium- and pyrite-bearing Mesoarchaean Witwatersrand reefs (Barton and Hallbauer, 1996). This was interpreted to indicate a reoccurrence of the depositional conditions in the Transvaal Basin that had prevailed during the formation of the gold-bearing Witwatersrand Basin (Els et al., 1995; Barton and Hallbauer, 1996; Frimmel, 1997). Mechanical recycling of the Kimberley Reef mined at the East Rand goldfield is the mechanism that is thought to provide detrital material and, by inference, the gold to the overlying Black Reef (Tucker et al., 2016). However, Black Reef detrital and recrystallised pyrite grains are larger than those from the Kimberly Reef. In addition, the trace element contents in these pyrite grains are different and indicate that these pyrite grains formed in different geochemical environments (Barton and Hallbauer, 1996). Black Reef detrital pyrite grains also have an unradiogenic Pb-isotope composition, which is unlikely to have developed from weathering and alteration processes from the Kimberly Reef with an enriched radiogenic Pb-isotope composition (Barton and Hallbauer, 1996). Both detrital and syngenetic pyrite grains occur together in Black Reef sediments. The U-Pb and Re-Os isotope data in detrital pyrite grains in the Black Reef and Witwatersrand reefs, respectively, show that they were derived from a ~3000 – 2800 Ma auriferous granitic source in the hinterland, while data for the concretionary pyrite grains in the Black Reef indicates a synsedimentary formation before ~2500 Ma (Barton and Hallbauer, 1996; Kirk et al., 2001).

The distinct nomenclature of the carbon-bearing phases is crucial to avoid ambiguity. There are several names for solid organic constituents in sedimentary rocks. For simplification, definitions by Mossman and Thompson-Rizer (1993) and Mossman et al. (2008) are used to identify the names of solid organic constituents in the rocks of the Black Reef.

Kerogen: “Remains of former living organisms – a solid polymer-like organic substance which has remained *in situ* since deposition". However, it is noted that kerogen is a precursor to hydrocarbons but is not itself a hydrocarbon. The Black Reef does not have carbon seams; therefore, the term kerogen will not be used to describe its carbonaceous material.

Bitumen: "An organic, random-macromolecular substance, which is mobile as a viscous fluid or was once a mobile fluid but has since solidified". This term is used interchangeably with hydrocarbon.

Pyrobitumen: Any dark, hard, non-volatile substance composed of hydrocarbon complexes, which may or may not contain oxygenated materials, and often associated with mineral matter. On heating, pyrobitumens generally yield bitumen. This term will be used interchangeably with carbon nodules and bitumen. In this study, carbon seams and carbon nodules will not be used interchangeably due to differences in formation and morphology, and the Black Reef does not have any carbon seams. However, *carbon nodules*, *pyrobitumen*, *carbonaceous material* and *hydrocarbons* will be used interchangeably because of their similarities in formation and morphology.

1.2 Research aims and objectives

There is a lack of detailed sedimentological study in the Black Reef Formation. Therefore, this current study incorporates sedimentological, geochemical and δ34 sulphur isotope analyses. The source of metals (gold and uranium) and how they were transported into the Black Reef is also not clearly defined. This study will therefore provide insight into part of the of the Black Reef that has not been thoroughly tested, utilising combined methodologies to provide a metallogenic model, thus contributing to the scientific community and form the doorstep to further exploration and exploitation of gold mineralisation in this sequence. The overarching aim of this study is to test the mechanism for gold mineralisation and the processes responsible its erratic development in this sequence. Genetic models that define the style of gold mineralisation in conglomerate-hosted deposits have been addressed in the last two decades so that they may be used for exploration purposes (Frimmel et al., 2005; Frimmel, 2005). In hydrothermal systems, redox reactions are responsible for precipitation of gold in solution for conglomerate-hosted deposits: (1) gold precipitated from solution by reduction when fluids interact with Fe- and C-bearing phases (Law and Phillips, 2005; William-Jones, 2009; Heinrich, 2015; Fuchs et al., 2016) and (2) gold precipitation from solution by oxidation when photosynthesising micro-organisms release free-oxygen at their surface and decrease gold solubility (Frimmel and Hennigh, 2015; Frimmel, 2014). Several contesting factors may be at play for gold deposition processes in the Black Reef, such as physical (natural sorting of gold and uranium based on density), chemical (such as redox precipitation) and trapping mechanisms (such as carbonaceous material). The preservation mechanism or the lack of preservation is investigated to determine why gold mineralisation is poorly developed in this sequence. This study intends to find evidence for the conglomerate-hosted gold mineralisation processes at the Black Reef and identify potential sulphur source rocks by comparing $\delta^{34}S$ isotopes to existing data, which may provide implication to the redox conditions at the time of gold deposition. Understanding the palaeoenvironmental and physiochemical conditions responsible for gold mobilisation and mineralisation and how gold is situated in the Black Reef, will allow for better definition of the systems responsible at the timing and emplacement of gold. The sedimentological characteristics associated with gold mineralisation, pyrite mineralisation and carbonaceous material are used to define the preferential emplacement of ore minerals. The incorporation of petrographic assessment aims to describe mineral assemblages, textures and paragenesis. Geochemical parameters, including $\delta^{34}S$ isotopes, will be used to identify the source of Black Reef sediments, and by implication, the gold and pyrite grains. They will also be used to determine alteration processes that occurred in the Black Reef palaeoenvironment. Fluid inclusions studies are used to identify the nature of the gold mobilising and mineralising fluids and in combination with the mineral assemblage textures to determine fluid pathway and interaction.

1.3 Scope and limitations

Due to limited surface exposures of unoxidised Black Reef Formation, the study is limited to studying drill core samples from the Carletonville goldfield. Intersections of other Black Reef Formation rocks such as those from the East Rand goldfield have been sourced from the literature and are used for comparative purposes.

1.4 Thesis organisation

This thesis consists of six chapters. Chapter 1 introduces the Black Reef Formation and outlines the geological concerns in the literature associated with this part of the South African stratigraphy. Chapter 2 focusses on previous work done on the Black Reef in terms of stratigraphy, geology, geochronology and isotopic chemistry, mineralogy and the various mineralisation models for Black Reef. Chapter 3 provides the materials and methods used to achieve the research aims and objectives. Results are presented in Chapter 4 and were subdivided into sections that describe drill core logging of the sedimentary rock units, textural features of the primary lithologies from petrographic studies, fluid inclusion microthermometry and Raman spectroscopy, quantitative geochemistry and major and trace element geochemistry, and finally $\delta^{34}S$ isotope geochemistry of pyrite grains. Chapter 5 contains the interpretation and discussion of the results with foci on (1) association of gold with the rock units and their textures and structures, (2) the origin of the sediments and, by implication, gold in the Black Reef, (3) the origin and nature of the gold mineralising fluids and the mechanisms of gold transportation and deposition in the Black Reef and (4) the redox conditions in the Neoarchean. A general conclusion in Chapter 6 summarises the principal findings of this research and how they advance the current knowledge of Black Reef petrogenesis.

Chapter 2: Geological Background

2.1 Kaapvaal Craton

The Kaapvaal Craton of southern Africa represents old, thick, continental crust that is bound by major intracratonic lineaments (Laurent et al., 2019). It hosts well-known mineral provinces such as the Witwatersrand Basin gold province, the Transvaal Basin iron formation province and the PGE-enriched Bushveld Igneous Complex (Söhnge, 1986). Various Archaean tonalitic gneisses and greenstone belts intruded by granitic basement rocks have been studied by workers such as Anhaeusser (1976) and Anhaeusser and Viljoen (1986). Most of these Archean greenstone belts and basement granites host orogenic gold deposits and other ore minerals. The Thabazimbi-Murchison Lineament (Fig. 2.1) is a prominent suture zone that formed through convergence accompanied by subduction of the Pietersburg Block beneath the Witwatersrand Block, and convergence accompanied by subduction of the Witwatersrand Block beneath the Kimberley Block (Schmitz et al., 2004). The Witwatersrand Block is an old granitic basement that formed and stabilised between 3.4 and 3.1 Ga (Poujol et al., 2003).

The most prominent, well-studied and oldest basement terranes in the Kaapvaal Craton is the ca. 3.55 – 3.22 Ga old Barberton Greenstone Belt (Anhaeusser, 1976; Dirks et al., 2013). Other less well studied greenstone belts on the Witwatersrand Block are the Murchison, Pietersburg and Giyani greenstone belts while the Kimberley Block hosts the Kraaipan and Amalia greenstone belts (Poujol et al., 2002, Poujol et al., 2003, Brandl et al., 2006). These greenstone belts contain lode gold deposits and minor pegmatite-related mineralisation (Hammond and Moore, 2006; Laurent et al., 2019). The Kaapvaal Craton basement rocks contain several granite-greenstone domes with the 2023 ± 2 Ma (Kamo et al., 1995) Vredefort meteorite impact exposing deeply buried basement rocks. The Johannesburg Dome, northeast of the study area (the Carletonville goldfield) formed by development of tonalite-trondhjemite-granodiorite rocks (TTG), followed by mafic plutonism and later emplacement of extensive homogeneous granodiorite–porphyritic granodiorite batholiths (Poujol and Anhaeusser, 2001). It consists of 3340 ± 3 Ma to 3114 ± 2.3 Ma (Poujol and Anhaeusser, 2001) tonalite-trondhjemite-granodiorite gneisses (TTG gneiss suite) and minor mafic rocks.

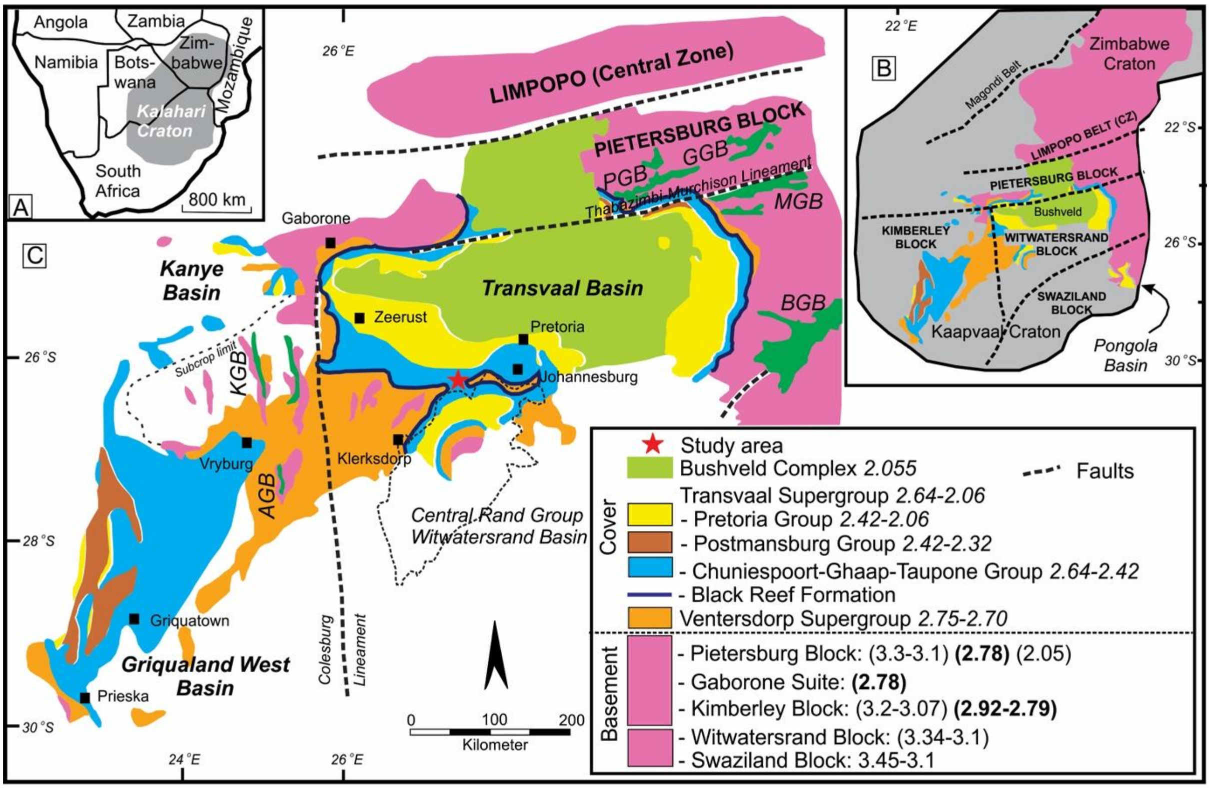

Figure 2.1: Geological map of the study area: (A) position of the Kalahari Craton in southern Africa, (B) basement blocks of the Kalahari Craton (composed of the Pietersburg Block, Kimberley Block, Witwatersrand Block and the Swaziland Block) and extension of the Neoarchaean to Palaeoproterozoic cover sequence of the Ventersdorp and Transvaal Supergroups, (C) position of the Transvaal, Griqualand West and Kanye basins on the Kaapvaal Craton. Outline of the Witwatersrand Basin is in the middle in dotted line. The Black Reef Formation (indicated by the blue line) is a thin and laterally extensive succession oat the base of the Transvaal Supergroup which youngs to the centre of the Kaapvaal Craton. A red star indicates sample location. Ages in the legend (in Ga). Predominant intrusion ages are bold and underlined (see text for references). BGB – Barberton Greenstone Belt, MGB – Murchison Greenstone Belt, KGB – Kraaipan Greenstone Belt, AGB – Amalia Greenstone Belt. Modified from Zeh et al. (2020).

Subsequent to the consolidation of the Kaapvaal Craton, epeiric basins developed, giving rise to the deposition of mixed volcanic and sedimentary deposits of the 3074 ± 6 Ma Dominion Group (Armstrong et al., 1991; Söhnge, 1986). The Dominion Group unconformably overlies the basement rocks and experienced greenschist to amphibolite facies metamorphism. The base of this group comprises pyrite-rich quartz-pebble conglomerate beds of the Dominion Reef with erratic uranium and gold concentration. In this reef, the concentration of uranium is higher than that of gold (Söhnge, 1986).

This epeiric basin enlarged to form the Witwatersrand Basin (Fig. 2.1) which was filled with clastic sediments to form the Witwatersrand Supergroup, and was interbedded with the one volcanic sequence of the Crown Formation (Söhnge, 1986). The Meso- to Neoarchaean Witwatersrand Basin extends for 52 500 km^2 in the central Kaapvaal Craton and lies above the

Dominion Group and unconformably above the granite-greenstone basement (Gartz and Frimmel, 1999; Agangi et al., 2013). The Witwatersrand Supergroup is composed of the ≤5-km-thick West Rand Group (2985 ± 14 Ma to 2914 ± 8 Ma) (Kositcin and Krapez, 2004) and the unconformably overlying ≤2.8-km-thick Central Rand Group (2902 ± 13 Ma to 2840 ± 3 Ma) (Armstrong et al., 1991; Frimmel et al., 1993; Gartz and Frimmel, 1999; Frimmel and Minter, 2002; Safonov and Prokof'ev, 2006; Fuchs et al., 2015). It represents a thick sedimentary succession, which represents formation in a foreland to retroarc setting containing offshore marine sediments with fluvial inputs (sandstone, shale and mudstone) followed by subaerial (fluvial) to shallow marine sequences of sandstone and quartz-pyrite conglomerates with minor shales (Fig. 2.2; Els, 1998; Frimmel and Minter, 2002; Agangi et al., 2013; Large et al., 2013). In the Carletonville goldfield, most of the past gold production was centred in the Carbon Leader Reef which forms part of the basal section of the Johannesburg Subgroup, Central Rand Group, comprising higher concentrations of gold than uranium. It is described as a 1.2 m thick gold-uranium-pyrite bearing conglomerate unit with a 1.2 cm thick carbon seam (Kirk et al., 2001; Frimmel and Minter, 2002; Large et al., 2013; Fuchs et al., 2016). The average grade of the Carbon Leader Reef at the Carletonville goldfield is 22.53 g/t gold and 0.58 kg/t U_3O_8 (Fuchs et al., 2016).

The volcano-sedimentary succession of the Ventersdorp Supergroup (U-Pb zircon age of 2714 ± 8 Ma) overlies the Witwatersrand Supergroup unconformably. The unconformity is indicated by the 7 m thick Ventersdorp Contact Reef (VCR) of the Venterspost Conglomerate Formation, which is a fluvial conglomerate that is auriferous, uraniferous, pyritic and oligomictic (Fig. 2.2) de Kock, 1940; Antrobus et al., 1986; Els, 1998; Frimmel and Minter, 2002; Agangi et al., 2013). It is one of the significant gold-bearing conglomerates mined with the Witwatersrand reefs, with a 5-12 g/t Au concentration (Frimmel, 2005). The 1.5 km thick Klipriviersberg Group is composed of tholeiitic flood basalts that overly the VCR (de Kock, 1940; Gartz and Frimmel, 1999; Agangi et al., 2013).

2.2 Transvaal Supergroup

2.2.1 Stratigraphy

The Neoarchaean to Palaeoproterozoic Transvaal Supergroup (2640 to 2060 Ma) is an approximately 15 km thick succession (Button, 1986) that lies in the northern and western part of the Kaapvaal Craton (Fig. 2.1) (Eriksson et al., 1995; Barton and Hallbauer, 1996; Frimmel and Minter, 2002). Two large igneous provinces confine its deposition, i.e. it is underlain by the 2.750 Ga Klipriviersberg flood basalts of the Ventersdorp Supergroup (Armstrong et al., 1991) and is overlain by the 2.054 Ga Bushveld Igneous Complex (Zeh et al., 2015). South Africa hosts two vast intracontinental basins of the Transvaal Supergroup, namely the Transvaal and Griqualand West basins, while Botswana hosts one intracontinental basin called the Kanye basin as shown by Figure 2.1 (Els et al., 1995; Eriksson et al., 1995; Barton and Hallbauer, 1996). The sub-basins in South Africa cover an area of 250 000 km^2 (Button, 1986). The sequence is composed of generally unmetamorphosed clastic and chemical sedimentary and volcanic rocks (Eriksson et al., 1993).

The eastern domains of the Transvaal Supergroup rest unconformably on Archaean granites, gneisses and greenstones, while the western domains unconformably overly the volcanic rocks of the Ventersdorp Supergroup (Button, 1986). The Transvaal basin has a depositional history described as a shallow epicratonic sea that submerged the majority of the Kaapvaal Craton and comprises predominantly sedimentary rocks (Els et al., 1995). The Wolkberg Group is clastic sedimentary succession underlying the Transvaal Supergroup (Zeh et al., 2020). It consists of a basal conglomerate interbedded with mafic volcanics and sandstone interbedded with mudstone. On the basin margins, the Neoarchaean Black Reef Formation lies unconformably above the Ventersdorp Supergroup, the Witwatersrand Supergroup and older granite-greenstone basement (Sharpe, 1949; Button, 1986; Clendenin et al., 1991; Eriksson et al., 1993; Henry and Master, 2008; Tucker et al., 2016). The Black Reef fluvial deposits grade up into the thick package of epeiric marine carbonates of the Malmani Subgroup and are overlain by the deep marine, economically important Penge Iron Formation of the Chuniespoort Group (Button, 1986; Eriksson et al., 1993; Els et al., 1995; Obbes, 1995; Eriksson et al., 1995; Safonov and Prokof'ev, 2006). Thereafter, the sequence grades up into a 10 – 200 m ‘transition zone’ comprising Fe- and Mn-rich dolomite intercalated with carbonaceous shale of the Chuniespoort Group. Finally, thick clastic sediments of the Pretoria Group quartzite cap the sequence (Fig. 2.2; Button, 1986; Els et al., 1995; Eriksson et al., 1995; Safonov and Prokof'ev, 2006; Fuchs et al., 2016).

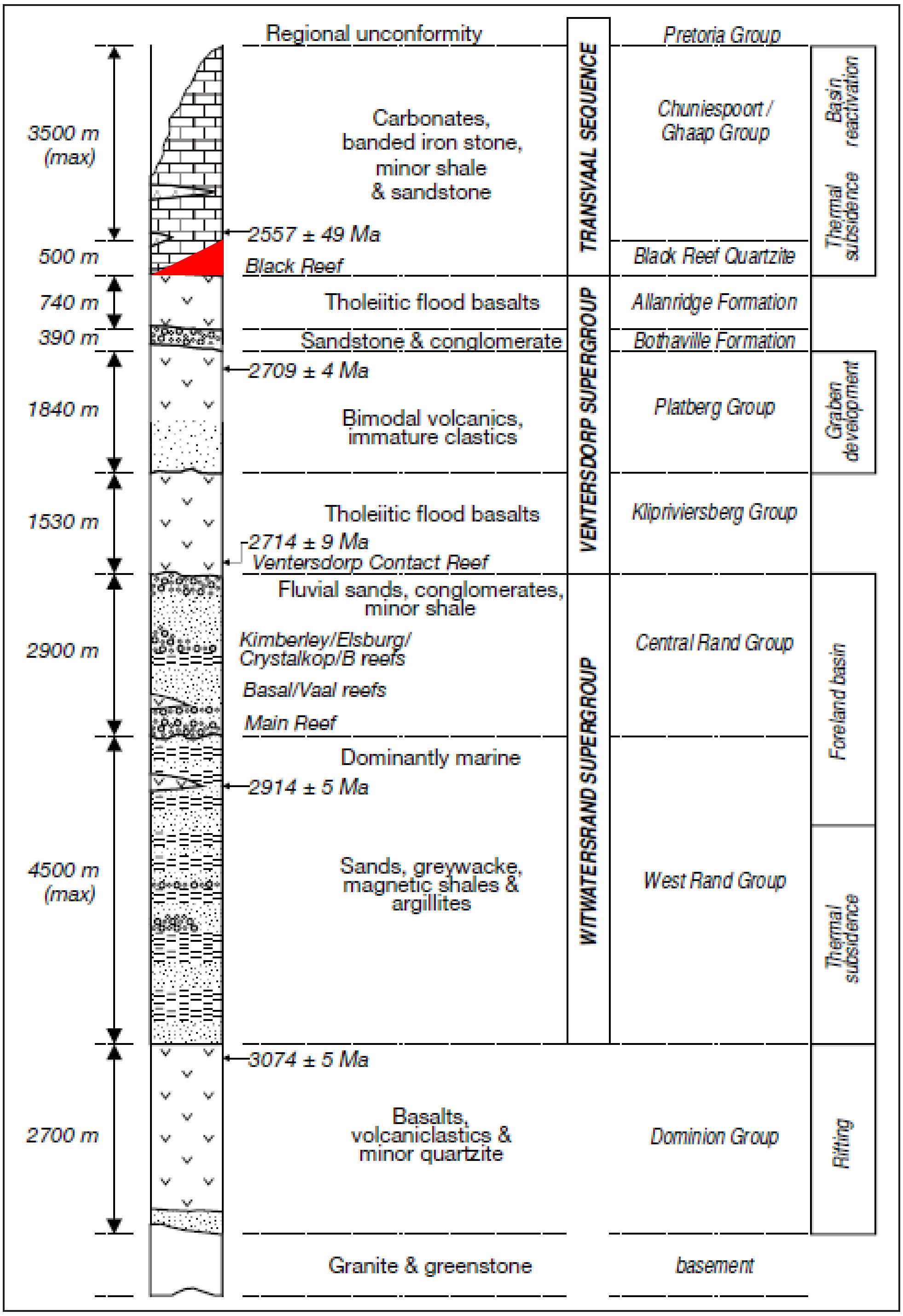

Figure 2.2: Generalised stratigraphic column summarizing the relativre relationship between Archaean basement rocks, Witwatersrand Supergroup units, Ventersdorp Supergroup units and Transvaal Supergroup units. The location of Black Reef Formation is indicated in red. Modified from Muntean et al. (2005).

2.2.2 The Black Reef Formation

The Black Reef Formation is a thin and laterally widespread sequence of fluvial siliciclastic rocks and forms the base of the Transvaal Supergroup (Clendenin et al., 1991; Eriksson et al., 1993; Obbes, 1995; Fuchs et al., 2016). Quartz arenites, carbon-rich shales and minor conglomerates form the main lithological package (Clendenin et al., 1991; Els et al., 1995; Eriksson et al., 1995; Fuchs et al., 2016). Obbes (1995) did a detailed study on the Black Reef and noted that the main sedimentary lithofacies are conglomerate, trough cross-bedded quartzite, horizontally laminated quartzite, planar cross-bedded quartzite and laminated siltstone and mudstone.

The Black Reef forms an upward-fining succession with a quartz arenite-rich lower unit containing pebble-bedded auriferous conglomerates to cross-bedded sandstones and arenites and grades up into the carbonaceous shale-rich unit (Sharpe, 1949; Button, 1986; Engelbrecht et al., 1986; Barton and Hallbauer, 1996; Eriksson et al., 1995; Fuchs et al., 2016). This upward-fining sequence represents a high-energy fluvial depositional palaeoenvironment able to transport pebble-sized particles (Barton and Hallbauer, 1996; Henry and Master, 2008). Therefore, the conglomerates and quartzite represent the transgressive clastic units deposited in a braided stream environment close to the shoreline (Obbes, 1995). Marine transgression flooded the shoreline and resulted in the deposition of black shales in a shelf environment (Obbes, 1995). The high-energy fluvial palaeoenvironment is overlain by a low energy beach and tidal flat palaeoenvironment able to deposit sand-sized particles, forming sedimentary structures such as trough cross-beds, planar cross-beds, plane beds and herringbone cross-beds. A shallow marine palaeoenvironment terminated the sequence by depositing fine-grained material, alongside carbonaceous material (Henry and Master, 2008). Economic deposits occur as the initial phase of a renewed sedimentation cycle (Sharpe, 1949).

The conglomerate bed (the Black Reef) is both petrographically and mineralogically similar to the Witwatersrand reefs (Frimmel and Minter, 2002). Sharpe (1949) distinguished that pebble accumulation occurs in areas where the unconformable underlying rocks are conglomerate beds. A narrow, ~90 cm ‘banket’ horizon exists with a high concentration of gold. The most prominent feature of the Black Reef is its abundant carbonaceous material, in the form of pyrobitumen, which is dispersed throughout the rocks as nodules, filling quartz-pebble fractures (<1 mm) and occurring in the cement (Safonov and Prokof'ev, 2006; Henry and Master, 2008; Tucker et al., 2016). More recent studies have provided evidence that the hydrocarbons represent residues of migrating liquids rather than remnants of *in situ* growth of algal mats and are based on the presence of oil inclusions in various generations of quartz (Gray et al., 1998; Fuchs et al., 2015).

2.2.3 Structure and basin analysis

The shape of the Transvaal Basin and the underlying strata within its vicinity was influenced by major events such as the emplacement of the mafic and ultramafic phases of the Bushveld Igneous Complex and from the Vredefort meteorite impact (Button, 1986). There is a homoclinal dip between 5 and 40^{o} around the Bushveld Igneous Complex where the dip increases towards this layered intrusion to accommodate the large volume of incoming magma (Button, 1986). Previous studies by Button (1973) proposed that the Transvaal Basin has a depositional environment of a passive southern margin relative to an active northern margin. The formation reflects fluvial sedimentation in channels on the locally deeply incised palaeosurfaces of the underlying rocks (Frimmel and Minter, 2002). This indicates that the major Black Reef sediment source area is north and northeast of the basin. The Black Reef conglomerates in the East Rand area were transported in a north to south direction (Tucker et al., 2016), indicating that the Channel Facies were embedded with coarse boulders of Witwatersrand sediments (Fig. 2.3).

In the East Rand goldfield, the Black Reef has three different facies types: i) the Channel Facies, ii) the Blanket Facies – Basal Unit, and iii) the Blanket Facies – pyrite Leader Unit. These facies represent the mineralised horizons (Eriksson et al., 1995; Fuchs et al., 2016). The Channel Facies contains a medium-grained dark quartzite matrix embedded with large quartz boulders. Cross-bedded alternating bands of pyrite in medium-grained quartzite of the Basal Unit overlie the Channel Facies, which is in turn overlain by the pyrite Leader Unit characterised by an 80 vol % of pyrite (Barton and Hallbauer, 1996; Fuchs et al., 2016). The conglomerate suite of the Black Reef contains above 20 % pyrite while the shale unit has an abundance of pyrite veinlets (Safonov and Prokof'ev, 2006).

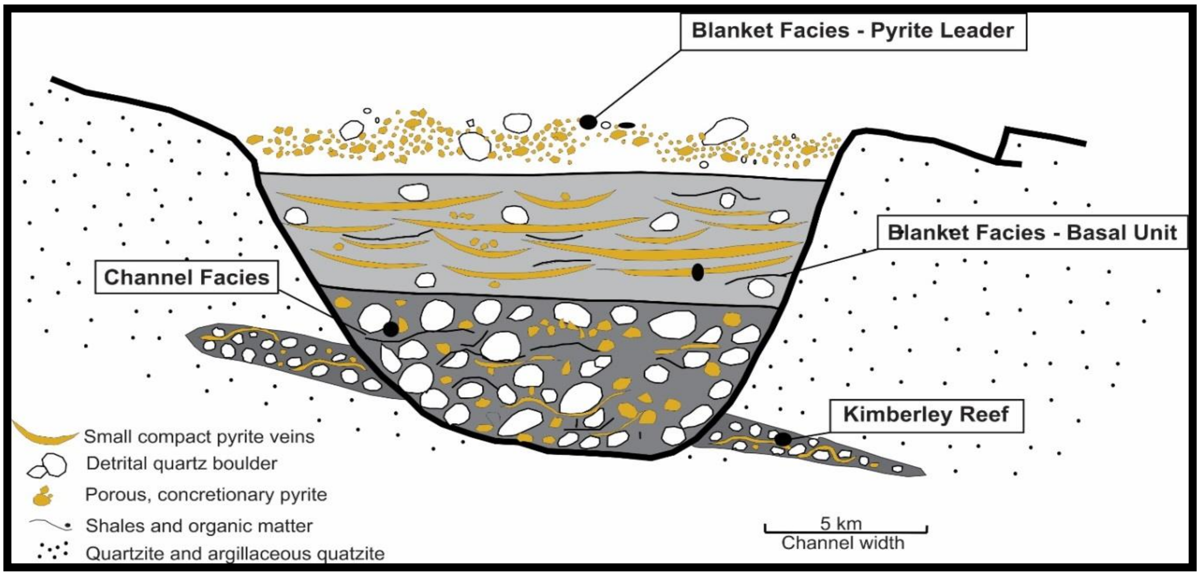

Figure 2.3: Black Reef facies types in cross-section shown to cut the underlying Kimberley Reef in the East Rand basin. The uppermost pyrite Leader is characterized by ~80 vol% pyrite and overlies the Basal Unit characterized by cross-bedded alternating bands of pyrite in a medium-grained quartzite and that is overlies the Channel Facies characterized by large quartz boulders in a medium-grained dark quartz matrix. Modified from Barton and Hallbauer (1996) and Fuchs et al. (2016).

Major gold deposits experience a structural control for gold deposition rather than a rheological control (Phillips and Powell, 1993). These structures include major shear zones, second- and third-order shear zones and cross-cutting faults. Specifically to the Black Reef, its unconformity with the underlying, gold-rich basement rocks, Witwatersrand reefs and VCR is the main control for economic concentrations of gold (Phillips and Powell, 1993).

2.2.4 Metamorphism and alteration

The Black Reef has experienced various metamorphic events since its deposition, which in turn has caused alteration of the sequence. Low-grade sub-greenschist metamorphic facies has been recorded in the Black Reef due to the presence of chlorite, muscovite, pyrophyllite and chloritoid-bearing mineral assemblages with peak conditions reaching 350 ± 50 ^{o}C and <3 kbar (Phillips and Powell, 1993; Frimmel, 1997; Law and Phillips, 2005). Loading of the Transvaal basin during the deposition of the ~2.100 Ga Pretoria Group caused burial diagenesis of the Black Reef, creating the first metamorphic event (Eriksson et al., 2006). After subsidence of the Pretoria Group, the emplacement of the 2.055 Ga Bushveld Igneous Complex ~45 My caused the second metamorphic event of the Black Reef (Zeh et al., 2015). The 2.023 Ga Vredefort meteorite impact ~32 My after emplacement of the Bushveld Igneous Complex caused the third metamorphic event (Kamo et al., 1996). The Vredefort meteorite impact caused a topographic ridge called the Rand Anticline, which exposes Black Reef Formation lithology on surface. The Bushveld Igneous Complex is concluded to have little effect on the distribution of the gold except to provide thermal metamorphism and a metasomatic overprint, causing alteration in the Black Reef sequence (Frimmel and Minter, 2002; Bose et al., 2012).

2.3 Carletonville goldfield

The Carletonville Goldfield (Fig. 2.4; location 7), previously known as the West Wits Line, is defined as an east-west line through the Middlevlei Inlier and Mooi River and between Wonderfontein Spruit and Fochville (Engelbrecht et al., 1986). The origin of the name was probably first used by de Kock (1964) and has been retained in literature until recent years in the mining industry. Stratigraphically, the Carletonville Goldfield falls in the Central Rand Group, except where different mines exploit the Black Reef belonging to the Transvaal sequence. The Randfontein Formation of the Central Rand Group in the Carletonville Goldfield consists of the Carletonville Member, Middlevlei Member and the Johnstone Member (Kent, 1980; Engelbrecht et al., 1986). The Carletonville Member contains the basal conglomerate North Leader Reef with erratic gold concentration, overlain by the Carbon Leader Reef that is enriched in carbon and contains economic gold concentration (Engelbrecht et al., 1986). A marker horizon "Green Bar", described as a soft compact green to black argillaceous quartzite or chloritoid shale, separates the Carletonville Member from the Middlevlei Member (Engelbrecht et al., 1986). The Middlevlei Reef rests on an erosional surface and is essentially quarzitic. The Livingstone Reef is also a small gold-rich quartz-pebble conglomerate (Engelbrecht et al., 1986). The Johnstone Reef of the Johnstone Member also contains a small, auriferous quartz-pebble conglomerate (Engelbrecht et al., 1986).

In the Carletonville Goldfield, the VCR is a <2.5 m thick quartz-pebble conglomerate and is an unconformity-bounded stratum composed of conglomerate and sandstone channeled deposits (Engelbrecht et al., 1986). The upper-most reef is the Black Reef with a sporadic development of the conglomerate at the base, with erratic gold concentration. Structure plays a vital role in defining the limits of the Carletonville Goldfield. The Witpoortjie Fault (Fig. 2.4) delineates the eastern boundary and is a normal fault with a downthrow displacement to the west (Els, 1987). The Mooi River Fault delineates the western boundary and is a normal fault with a downthrow displacement to the east (Els, 1987).

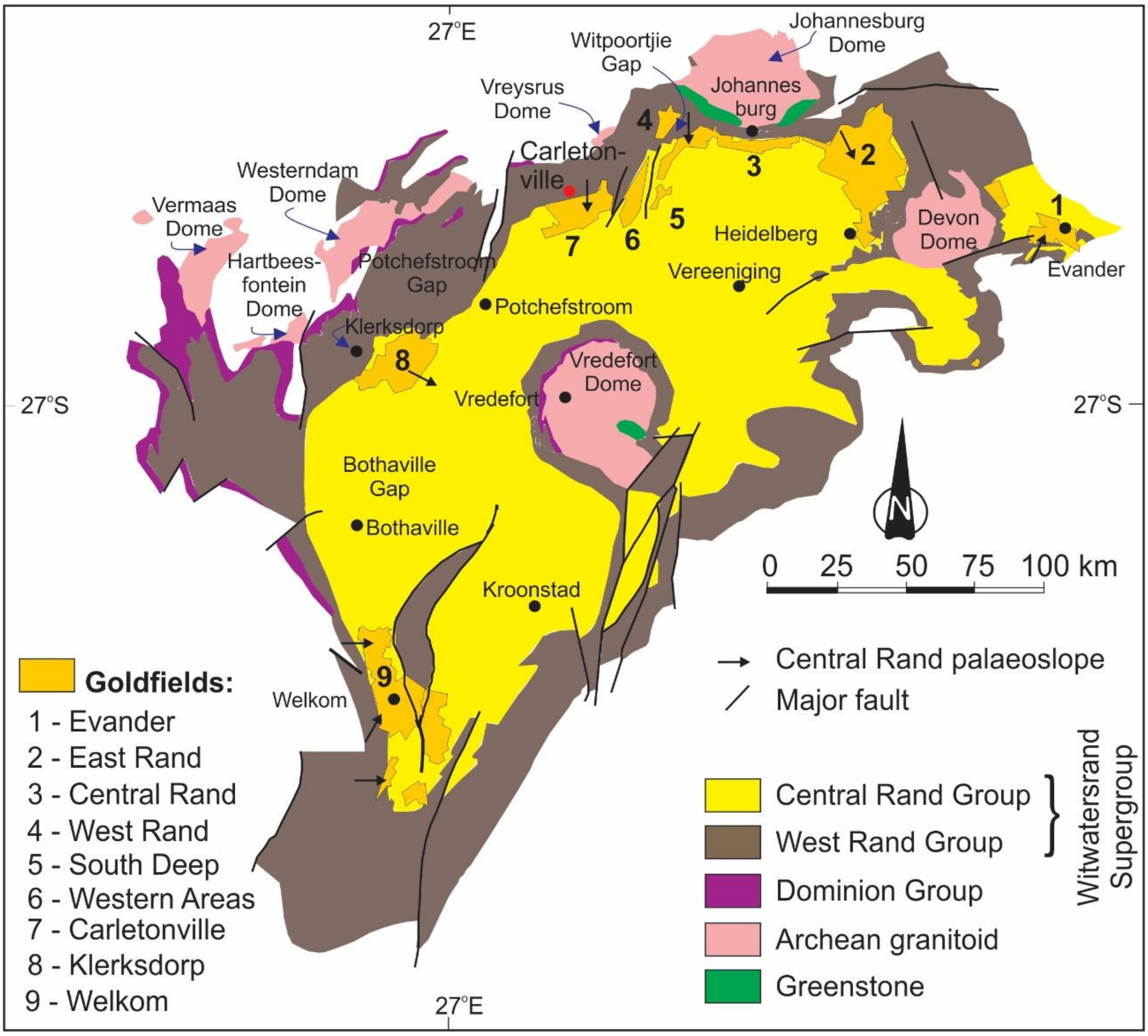

Figure 2.4: Surface and sub-surface geological map of the Witwatersrand basin. The distribution of Archaean granitoid domes and that of goldfields are shown. The study area is indicated by the red circle in Carletonville Goldfields – location 7. Modified from Frimmel et al. (2005).

2.4 Stable S-isotopes of the Black Reef Formation

The Archaean-Proterozoic boundary marks a significant period of Earth's history when the oceans and atmosphere transformed into conditions that are more oxic through the Great Oxidation Event (GOE). Mass-independent fractionation (MIF), a photolytic effect that induces isotope fractionation, is observed in sedimentary rocks that formed prior to the GOE, that is, older than 2.45 – 2.33 Ga. (Farquhar et al., 2000). $\delta^{34}S$ is defined as the standardized method of reporting measurements of ratio of stable isotopes of Sulphur, ^{34}S:^{32}S, in a sample against the equivalent ratio in a known reference, while $\Delta^{33}S$ is used to identify S-MIF, requiring a second reference isotope taken to be ^{34}S (Domalag-Goldman et al., 2011). Reference to the use of $\Delta^{33}S$ and $\delta^{34}S$ is to observe how pyrite preserves the signatures of their sulphur source. The MIF effect produces anomalous fractions of ^{33}S and ^{34}S relating to interaction of sulphur species in the atmosphere with high wavelength UV radiation only when the atmosphere contained 10 – 5 times less free oxygen than the present day atmosphere (Farquhar et al., 2000; Farquhar et al., 2013). These sulphur species separate to form pathways and reservoirs for positive MIF sulphur and negative MIF sulphur (Partridge et al., 2008). Therefore, positive $\Delta^{33}S$ arises from sulphides that formed by microbial or inorganic reduction of elemental sulphur while negative $\Delta^{33}S$ arises from sulphides formed by microbial or inorganic reduction of seawater sulphate (Partridge et al., 2008).

Before the GOE, the $\Delta^{33}S$ values showed great variability. The onset of the GOE caused the stability of MIF where $\Delta^{33}S$ values are preserved in the global sedimentary record. This was caused by the high oxygen levels in the terrestrial atmosphere, thus preventing photochemical reactions from occurring (Selvaraja et al., 2017). This MIF signature cannot be altered other than by extreme addition of a non-MIF bearing sulphur to dilute it, and therefore, acts as a powerful isotopic tracer of geological and ore-forming processes (Selvaraja et al., 2017). Costa et al. (2017) indicated that detrital pyrite is a redox-sensitive mineral occurring as an accessory phase in clastic sedimentary rocks that were deposited before the GOE. Mass-independent signals in the sedimentary rock record preserve the intensity of redox cycling of sulphur in surface environments due to high quantity of sulphide and sulphate rocks (Farquhar et al., 2013).

The material development of bacteria and other micro-organisms during Transvaal times could account for the high degree of pyritisation of the Black Reef deposits (Sharpe, 1949). Work conducted by Frimmel (2005) indicated that Witwatersrand-type mineralisation occurred during conditions that favoured S-isotope mass-independent fractionation and typical magmatic $\delta^{34}S$ values, which support a detrital origin for gold. Frimmel (2005) suggested that the Neoarchaean fO_2 was a factor of ~10^{-3} less than that of modern atmosphere and agreed with the preservation of mass-independent S-isotope fractionation, which supports an anoxic atmosphere prior to 2.3 Ga. Hofmann et al. (2009) conducted a multiple S ($\delta^{34}S$ and $\Delta^{33}S$) isotope study of rounded pyrite grains from 3.1 – 2.6 Ga conglomerates and revealed that they are of detrital origin, supporting anoxic surface conditions in the Archaean. These pyrite grains have both crustal and sedimentary sources with $\Delta^{33}S$ = -1.3 ‰.

In the VCR, Agangi et al. (2013) studied the zonation of pyrite as a record of mineralisation and found that porous and concentrically laminated pyrite grains are considered as generation

1 pyrite (detrital) and are enriched in Au (average of 6.4 ppm, maximum 70 ppm), in addition to Sb, Tl, Pb, Mn, Mo, Cu and Ag. The trace element composition of this generation 1 pyrite in the VCR and the detrital pyrite textures and S-isotopes of the Carbon Leader Reef in the Carletonville Goldfield (Large et al., 2013) resemble pyrite known to have formed in sub-oxic to anoxic environments associated with black shales.

2.5 Black Reef gold and uranium metallogenic models

Sedimentological studies by Els et al. (1995) revealed that the gold mineralisation in the Black Reef was derived by erosion of the underlying Witwatersrand Reefs containing detrital gold because gold in the Black Reef is restricted to the conglomerates. This is because parts of the Black Reef with economic concentrations of gold resemble those of the underlying Witwatersrand reefs enriched with gold (Henry and Master, 2008; Fuchs et al., 2016). A possible source of gold is, therefore, the recycling of the underlying and proximal reefs of the Central Rand Group in the upper Witwatersrand Supergroup (Frimmel, 2014; Tucker et al., 2016; Pearton and Viljoen, 2017). As such, the presence of erosional unconformities is an important control on mineralisation (Frimmel, 2018). This conclusion reiterates one proposed by de Kock (1940) that potentially exploitable VCR in the Far West Rand is confined to areas where the Ventersdorp Supergroup overlies tilted and eroded gold-bearing horizons of the Upper Witwatersrand Supergroup. This reveals a potential spatial distribution of gold in the Black Reef on top of post-Witwatersrand erosion surfaces (Frimmel, 2014; Tucker et al., 2016). Payable Black Reef deposits are found near, and downstream, of auriferous-related conglomerates suggesting a limited fluvial reworking of the placer (Sharpe, 1949; Barton and Hallbauer, 1996; Safonov and Prokof'ev, 2006). This indicates that the Kaapvaal Craton was able to upgrade gold content by mechanical and, in the case of the Black Reef, chemical reworking of gold-bearing strata (Frimmel, 2018).

This hypothesis has been ongoing since Sharpe (1949) also attributed the gold mineralisation of the Black Reef in the East Rand to being near the underlying Kimberley Reef while in the West Rand Black Reef gold mineralisation is restricted to where bankets in the Central Rand occur in its immediate footwall. This suggests that gold grades are retained at the original level with very little migration of gold. The sedimentary reworking hypothesis was nullified, however, by noting high variation in the nature and quantity of the pebbles relative to the heavy minerals and the differences in comparing the morphology and composition in detrital pyrite in the Black Reef to that of detrital and epigenetic pyrite in the underlying Witwatersrand reefs

(Barton and Hallbauer, 1996; Fuchs et al., 2016). Barton and Hallbauer (1996) showed that pyrite morphology and trace element content of detrital pyrite grains from the Black Reef indicate that the grains are derived from a ~3000 – 2800 Ma granitic, hydrothermally altered source rocks while the Pb-isotopic compositions of concretionary pyrite reflect synsedimentary formation in a tidal flat environment before ~2500 Ma. The Black Reef detrital pyrite grains are much larger - defined as porous, mud ball pyrite (Safonov and Prokof'ev, 2006) - and have lower proportions of radiogenic Pb and lower proportions of ^{238}U than those in the Kimberley Reef (Barton and Hallbauer, 1996). This has given rise to a model involving hydrothermal processes playing a role in the mineralisation of the Black Reef by remobilisation of gold in the underlying Witwatersrand reefs (Tucker et al., 2016).

According to Frimmel (1997) and Gauert et al. (2011), different degrees of true fineness, Hg and Cu concentrations and their S and Ni trace element contents, can distinguish the Black Reef and Witwatersrand gold reefs. Furthermore, elements such as Sn, Sb, Pd and Pt are correlatable with gold and are effective for gold source detection or serve as indicator minerals. To decipher the gold provenance problem, Gauert et al. (2011) fingerprinted Au using EPMA, SR-µ-XRF, TOF-SIMS and LA-ICP-MS. By fingerprinting Au, they characterized the Au based on its impurities or trace element content. This study was inconclusive and left an unresolved question about gold provenance for the Black Reef. They completed the study by proposing that similar heavy mineral content favours a reworked Witwatersrand gold origin of the Black Reef gold. However, the frequency of concretionary pyrite with non-radiogenic Pb isotope composition in the Black Reef and the more frequently occurring Ni-Co-Fe-sulpharsenides in the Black Reef argues against the reworking hypothesis. The Black Reef gold in the East Rand has a lower fineness and lower Hg and Cu contents compared to Witwatersrand gold. Therefore, the source of Black Reef gold can be attributed to alternative origins such as volcanic massive sulphide (VMS) deposits and older Archaean greenstone-hosted gold occurrences (Tucker et al., 2016).

The Black Reef experienced intensive post-depositional hydrothermal alteration by circulating aqueous fluids and liquid hydrocarbon that itself precipitated large volumes of native gold (Fuchs et al., 2016). Fuchs et al. (2015) strengthens the notion that the *in-situ* growth of uraninite and anatase nanocrystals in the pyrobitumen from the Carbon Leader Reef in the Carletonville Goldfield implies mobilisation and concentration of U and Ti by formerly mobile liquid hydrocarbons. This implies that the gold in the Black Reef is the product of chemically triggered precipitation from hydrothermal fluids. Since carbon seams have yielded ~40 % of the total Witwatersrand gold production, there seems to be a spatial relationship between gold and carbon seams, suggesting that organic matter plays an important role in precipitating gold from solution (Frimmel and Minter, 2002; Safonov and Prokof'ev, 2006; Drennan and Robb, 2006??).

In the Carletonville, Klerksdorp and Welkom Goldfields (Fig. 2.4 locations 7, 8 and 9), Phillips and Powell (2015) support a hydrothermal model for gold deposition based on alteration in the gold distribution at various scales. Metamorphism of mafic material adjacent to the Witwatersrand Basin produced auriferous, low salinity fluids at ~ 500 ^{o}C, shown by shale units from 40 major mines. Fluid pathways were large shear zones in the goldfield's footwall alongside unconformities, veins and reef packages. Gold precipitation occurred at about 350 ^{o}C and 10 km depth when this fluid reacted with carbon- and iron-bearing rocks. Phillips and Law (1994), Frimmel and Minter (2002), Fuchs et al. (2016) and Fuchs et al. (2017) concluded that the metamorphic replacement model for gold genesis in the Black Reef Formation implicates metamorphic fluids in the transport of gold. The gold was carried as a bisulphide complex ($Au(HS)^{2-}$) and was destabilised electrochemically either by a reduction in fO_2 or by Fe (on pyrite) and C (on pyrobitumen) during metamorphism. They demonstrated Black Reef gold was chemically recycled from the Witwatersrand reefs and subsequently chemically precipitated. Frimmel (2018) summarised that the Black Reef contains abundant detrital gold, uraninite, pyrite and pyrobitumen, and that Black Reef sourced gold from the Witwatersrand ore with an approximately 170 t gold endowment. A recent study by Nwaila et al. (2019) revealed that the Black Reef has both syngenetic and epigenetic gold grains but not all Black Reef sequences are mineralised. Therefore, sedimentary processes primarily control gold grade and the main mechanical processes are followed by hydrothermal activity.

Chapter 3: Samples and Methodology

This multidisciplinary study incorporates different aspects of geology, geochemistry and stable isotope geochemistry. The following methods were used to achieve this study's aims and objectives: core-logging and sampling, petrography, geochemical analysis (XRF and ICP-MS), fluid inclusion microscopy and Raman spectroscopy and S-isotope analysis.

3.1 Sample selection and core logging

Five diamond drill cores (32 mm diameter) obtained from Sibanye Stillwater Ltd in the Carletonville Goldfield were used for this study. The drill cores were logged in detail to record characteristics of the mineralised reefs and the overlying and underlying lithology. These characteristics were clast size, matrix component, pebble roundness and sphericity, clast packing, pebble assemblage and amount of pyrite mineralisation. The drill cores reach up to 68 m in length, intersecting the Black Reef and include rock types such as quartz arenite, conglomerate and carbonaceous shale interbedded with siltstone and at times, dolomite. Four of these drill cores (drill core IDs: D7P5047, D8P04251, D8P04252, D8P04281) covered intersections of the Black Reef Formation, and the fifth drill core (drill core ID: D8P04299) covered the Livingstone Reef of the upper Central Rand Group. The Livingstone Reef is included in this study because it is found in contact with the Black Reef in the study area and there are similarities in physical appearance and macro features such as pebble size, pebble roundness, lithology sequence and amount of pyrite mineralisation.

Sedimentological characteristics were classified using the Wentworth scale in Table 1.1. The number of pyrite grains determined the amount of mineralisation within the rock units. Pyrite mineralisation was described as massive, net-textured or disseminated, and was described if it occurred as pyrite stringers. Other features described in the rock units are grain size and roundness, matrix- versus clast-support, mono-, oligo- or polymictic clast types, sediment maturity and matrix colour.

Table 3.1: Modified Udden-Wentworth sedimentary grain-size scale to differentiate coarse sediment (modified after Blair and McPherson, 1999).

FRACTION		CLASS	GRADE	PARTICLE LENGTH
Lithified	Unlithified			(mm)
Conglomerate	Gravel	Boulder	very coarse	4096
			coarse	2048
			medium	1024
			fine	512
		Cobble	coarse	256
			fine	128
		Pebble	very coarse	64
			coarse	32
			medium	16
			fine	8
		Granule		4
Sandstone	Sand	Sand	very coarse	2
			coarse	1
			medium	0,5
			fine	0,25
			very fine	0,125
Mudstone or Shale	Mud	Silt	coarse	0,063
			medium	0,031
			fine	0,015
			very fine	0,008
		Clay		0,004
				0,002
				0,001
				0,0005
				0,0002
				0,0001

3.2 Petrographic and mineralogic analysis

3.2.1 Petrography

Thirty-four samples were selected for petrographic analysis to give a detailed insight into the mineral assemblages, textures and any related microstructures of the different rock types. These samples were selected based on their differences in mineralogy, their variation in matrix colour due to varying amounts of carbonaceous material, their variation in the amount of pyrite mineralisation and their macroscopic textures. This selection made it easier for comparison and to eliminate sample bias for further screening for other analyses ahead. Uncovered, polished thin sections (40 mm x 25 mm) were prepared at the School of Geosciences, University of the Witwatersrand. They were used to study the textures and association of ore minerals with the surrounding silicate minerals. The Olympus BX63 petrographic microscope from the Microscopy and Microanalysis Unit (MMU), University of the Witwatersrand, was used to obtain the overall view of the thin section in plane polarised light (PPL), cross-polarised light

(XPL) and reflected light and the Olympus BX41 petrographic microscope from the School of Geosciences was used to obtain higher-resolution images.

3.2.2 SEM analysis

A scanning electron microscope (SEM) from the School of Chemical and Metallurgical Engineering, University of the Witwatersrand, was used to obtain thin-section images of various samples by scanning the surface of interest with a focused beam of electrons. Ten samples were selected for SEM imaging to identify phases that are present within the carbonaceous material, identify the presence of gold and uranium phases and describe the association of the carbonaceous material with other silicate and sulphide phases. These samples were chosen because they showed variable amounts of carbonaceous material, carbonaceous material with different morphologies, and to confirm other phases that were complex to identify using traditional microscopic identification. The Carl Zeiss Sigma FE-SEM equipped with Oxford x-act EDS detector was used with a 30-micron spot size. The machine analyses two thin sections at a time with a 60 second analysis time per spot, first obtaining a backscattered electron (BSE) image and then a secondary electron image to show topography. Energy dispersive X-ray spectrometry (EDS) was used to acquire chemical compositions of phases of interest.

3.2.2 XRD

The first aliquot of samples was crushed then pulverised using a jaw crusher and agate mill and analysed by X-ray powder diffraction (XRD). This analysis was used to identify crystalline phases in pulverised samples. A *PANalytical* X'Pert Pro instrument at the XRD Analytical & Consulting Laboratories (South Africa) was used to identify phases. Scans were started at 5° and terminated at 90° relative to the incident X-ray beam. Samples were also spun dg analyses to mitigate for the potential presence of larger grains in the mixtures. The phases were identified using X'Pert Highscore 4 plus software. The Rietveld method (X'Pert Highscore 4 plus) was used to estimate the relative phase amounts (vol %). This analysis does not detect any present amorphous phases. XRD is only semi-quantitative and can only detect crystalline mineral phases with abundances of >3 vol %.

3.3 Fluid inclusion microthermometry and Raman spectroscopy analysis

3.3.1 Fluid inclusion microthermometry

Nine samples from all five drill cores were analysed for their fluid inclusion and microthermometric characteristics. Sample selection was limited to hydrothermal quartz grains that are white in colour, quartz grains with microfractures and quartz grains surrounded by high pyrite mineralisation. This selection was based on core logging and petrographic analyses. This analysis was performed to obtain physiochemical characteristics of the mineralising fluids in the Black Reef and compare these data with known Witwatersrand Supergroup fluid inclusion data. Samples were prepared as 150 µm doubly polished thin sections in School of Geosciences at the University of the Witwatersrand. The wafers were then studied using the BX41 petrographic microscope to locate the fluid inclusions for easier access under high resolution. The wafers were chipped with tweezers at the desired location and placed on a LINKAM THMS600 cooling stage connected to liquid N2 feeder in the School of Geosciences at the University of the Witwatersrand. The LINKAM stage was connected to a LINKSYS32 program to control the cooling and heating rates. The heating and cooling rates were generally set to 5 ^{o}C/min and were decreased to 1 ^{o}C/min when temperatures approached homogenisation. On cooling, the limit was set at -120 ^{o}C/min, and on heating, the limit was set at 20 ^{o}C higher than the homogenisation temperature.

3.3.2 Raman spectroscopy

Raman spectra were acquired using the 514.5 nm line of an argon-ion laser and a Horiba LabRAM HR Raman spectrometer equipped with an Olympus BX41 microscope at the MMU in the University of the Witwatersrand. The incident laser beam was focused onto the sample using a 100x objective, and the backscattered light was dispersed via a 600 lines/mm grating onto liquid nitrogen cooled CCD detector. The signal was acquired and processed by Lab Spec v5 software. The laser beam resolution for this configuration was about 1.5 cm^{-1}. The *HOKIEFLINCS_H2O-NACL* excel program was used to calculate the salinity and the density of these fluid inclusions.

3.4 Chemical analysis

Whole-rock compositions for forty-nine samples were obtained using X-Ray fluorescence spectroscopy (XRF) for major elements and Inductively coupled Plasma Mass Spectrometry

(ICP-MS) for trace elements. A hammer was used for crushing the samples since there were half-diameter core samples that were less than 30 cm in length. The crushed samples were milled for 2 minutes until pulverised. Samples were prepared at the Earth Lab at the University of the Witwatersrand. The post-Archaean Australian shale (PAAS) composite values of Taylor and McLennan (1985) was used to normalise all major and trace element data because of the absence of reliable Archaean shale reference data.

3.4.1 Major element analysis

Major elements were analysed using the *PANalytical* PW2404 XRF spectrometer in the Earth Lab at the University of the Witwatersrand. The detection limit of this machine is 0.01 %. Firstly, loss on ignition (LOI) was performed by weighing 1 g of each sample into a silica crucible and ignited at 1020 °C for 40 minutes, then the weight of the samples was recorded. Secondly, 1.75 g of a LiBO4 flux was added into Pt crucibles and ignited at 1020 °C for 40 minutes. Then 0.34 g of pre-ignited sample was added in the Pt crucibles with ignited flux and ignited at 1020 °C for 50 minutes. The ignited sample was then cooled, weighed and ignited again to make a liquid which was made into a fusion disk on a hotplate for 2 hours and left to anneal overnight. The reported Fe_2O_3 content in these data represents total Fe content. The standard performance data is presented in Figure 3.1.

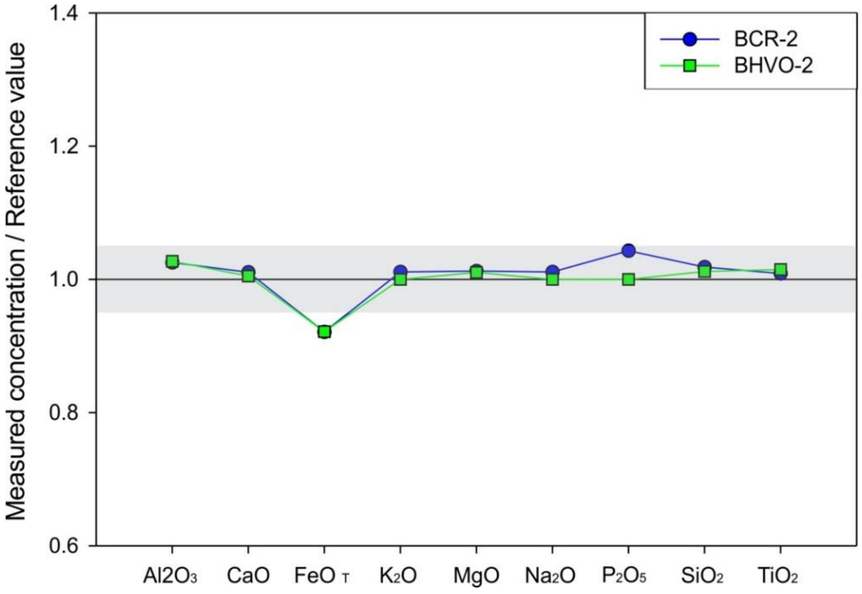

Figure 3.1: Major element standard performance data for measured BRC-2 and BHVO-2 for this study versus the reference values from USGS (2000). The horizontal line at 1.0 indicates values where the measured concentrations of the reference material are equal to the known concentrations of that material. Except for FeO_T, most of the elements from the measured reference material lie within 5 % error of the known value, indicated by the shaded area. FeO_T in the samples from the Black Reef correspond to values from previous studies (Blane, 2013; McLoughlin, 2015).

3.4.2 Trace element analysis including REE and Au

Whole-rock trace elements were analysed using the *Perkin Elmer Elan DRC* ICP-MS model equipped with a standard crossflow nebuliser in the Earth Lab at the University of the Witwatersrand. The detection limit of this machine is 0.01 ppm. Stock solutions were used as calibrators together with 50 mL of an internal standard. Calibration standards with increasing concentration with made sequentially by pipetting 50 µL of the standard, 300 µL of 5 % HNO_3, 10 µL of HF and the internal standard was added to make up to 50 mL of the measuring cylinder. Each of the 49 samples was dissolved by microwave digestion using 50 mg of sample dissolved in 6.1 mL of 2:1 HF:HNO_3 solution and left to dissolve for 55 minutes at 190 ^oC. The solutions were then rinsed with 10 % nitric acid and then dried down to 70 ^oC on a hotplate. Two final additions of 2 mL nitric acid were added then first let to dry down at 60 ^oC for 24 hours then secondly dried down to 70 ^oC then removed from the hotplate with a final addition of 300 µL nitric acid, capped and stored for analysis. The samples were also diluted under the same parameters of the solutions added to the measuring cylinders of the standards after they have undergone microwave digestion. Concentrations of 39 elements were recorded with procedural blanks and standard certified reference materials (BHVO-2 and BCR-2) to monitor data quality. The standard performance data is presented in Figure 3.2a.

Gold content was determined by fire assay following a dry procedure by furnace methods using the *Lead Collection Fire Assay, New Pot with ICP-MS Finish (Method FA25N/MS)* at Intertek Genalysis Laboratory, Perth. The most effective process of collecting gold is through PbO fire assay than the nickel sulphide (NS25) method. With this method, 25 g of the sample was pulverized, placed in new pots so that cross-contamination of gold is minimized, and mixed with a PbO-based flux. The PbO was reduced to molten Pb using an organic reducing agent, where the molten Pb mixes well with precious metals, sinks to the bottom of the melt to coalesce, and forms a button. Oxidation of the Pb button occurs in magnesia cupels in a furnace resulting in PbO absorbing in the cupel, and the precious metals are left behind to coalesce into a prill. The prill was transmitted into a test tube, digested in aqua regia, measured for volume then diluted for analysis by ICP-MS. This analytical procedure can detect low concentrations such as 1.00 ppb Au. Certified reference materials used were AMIS0192, and OREAS 25a, 45d and 45e, with the standard performance data is presented in Figure 3.2b. Sibanye Stillwater Ltd. provided other Au concentration data.

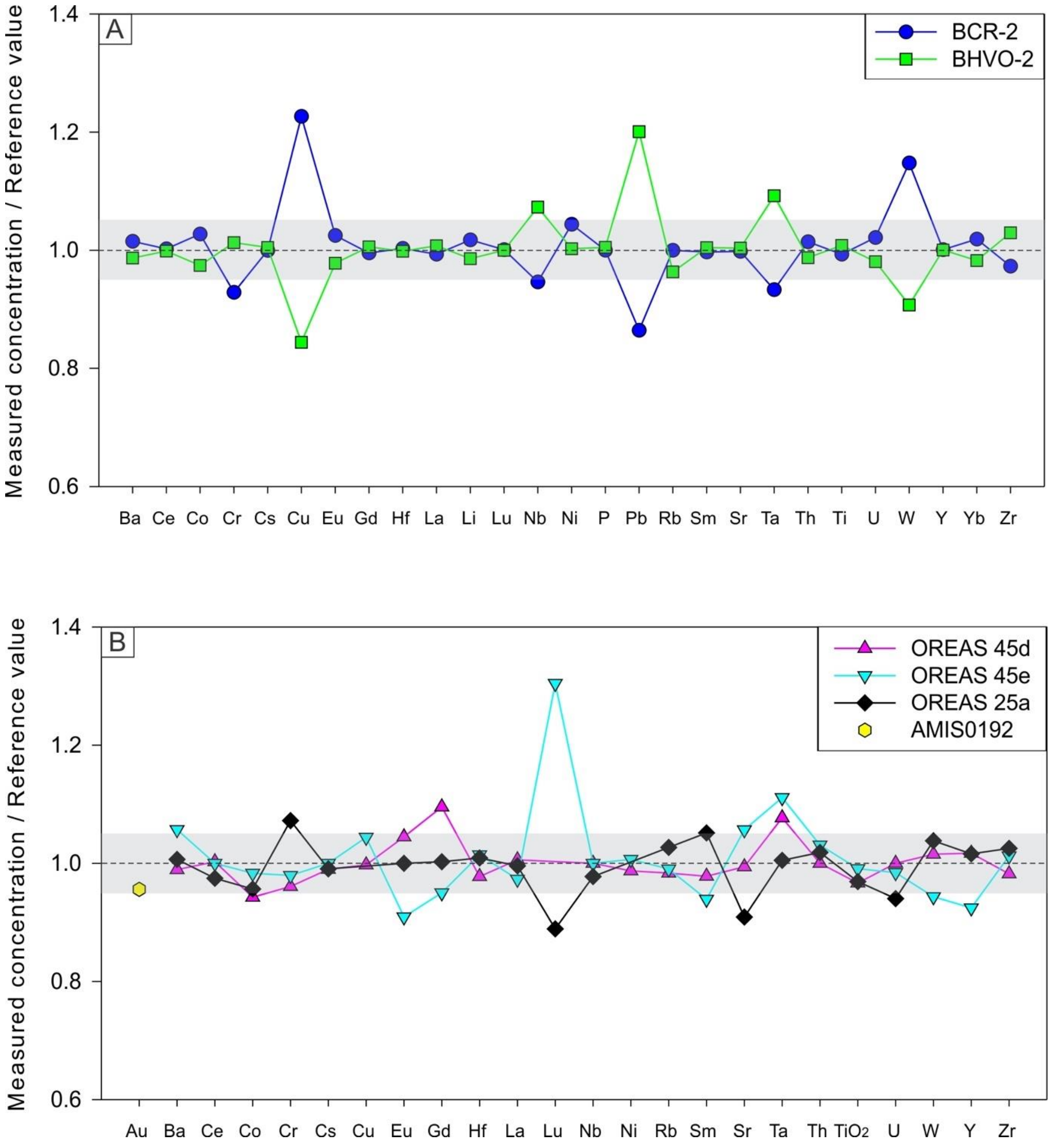

Figure 3.2 (A) Trace element standard performance data for BRC-2 and BHVO-2 for this study versus the reference values from USGS (2000). The dashed line indicates values where the measured concentration of the reference material is equal to the known concentration of that material. Most of the elements from the measured reference material lie within 5 % error of the known value, indicated by the shaded area, except for Cu, Nb, Pb, Ta and W. The errors are not traced to neither sample preparation, analysis or data handling. (B) Trace element standard performance data for OREAS-45d (pink), OREAS-45e (blue), OREAS-25a (black), and AMIS0192 (yellow dot – Au) for this study versus the reference values from assay certificates downloaded from https://www.ore.com.au/ (2020) and https://www.amis.co.za/ (2020). The dashed line indicates values where the measured concentration of the reference material is equal to the known concentration of that material, where several elements from the measured reference material lie within 5 % error of the known value, indicated by the shaded area. Lu lies over 20% error of the known value whereby the errors are not traced to neither sample preparation, analysis or data handling.

3.4.3 Use of major and trace metals and problematic elements

The major elements are mainly used to determine the amount of weathering and alteration. Trace element data will be used to map out the possible sources for the Black Reef Formation sediments. The most important elements are high field strength elements (HFSEs) which preferentially concentrate in felsic rocks because of their incompatible nature, and the X_{Mg} and Ni/Co ratios which is a proxy for mafic rocks in the source area. Problematic elements, such as Cu, Nb, Pb, Ta and W, are not used for this purpose. However, all other elements used for the purpose highlighted above are consistent with known values, indicating that the methods are effiecient and the hypotheses made in this study are made with high confidence data.

3.5 Total organic carbon and total sulphur analysis

Total organic carbon (TOC) and total sulphur (TS) were analysed at Intertek Genalysis Laboratory in Perth using the Eltra Infrared CS-2000 LECO analyser with a detection limit of 0.01 %. Pulped samples were weighed, placed in a ceramic crucible and mixed with a flux so that carbon and sulphur are oxidised. The sample and flux were heated in a furnace to oxidise the elements to CO_2 and SO_2, respectively. Elemental carbon or sulphur concentration in the sample is proportional to the wavelength at which these gases absorb infrared radiation. A standard (OREAS 45d) with known concentrations for C and S was used as the calibrator, and a control blank was used.

3.6 S-isotope analysis

Eighteen whole-rock pulp samples were converted into a mixture of SO_2, CO_2, N_2 and H_2O in a Costech Elemental Analyser (EA) at the University of Arizona, United States of America. This analyser is equipped with a Carlo Erba sulphur reactor. The mixture of the gaseous phases was carried on a stream of He gas. H_2O was removed in an Mg perchlorate trap while the other gases were separated in a gas chromatograph column. The remaining SO_2 + He gas was passed into a Thermo Finnigan Delta Plus Continuous Flow Isotope Ratio Mass Spectrometer (CFIRMS) where data are reported as per mil variation with respect to the Cañon Diablo troilite ($\delta^{34}S_{CDT}$ ‰) international sulphur isotope standard, as $\delta^{3x}S = 1000[(^{3x}S/^{32}S)\text{sample} - (^{3x}S/^{32}S)_{CDT} / (^{3x}S/^{32}S)_{CDT}]$.

Chapter 4: Results

4.1 Core logging and gold grade

Due to confidentiality issues, the mine concealed information of certain portions of two of the studied drill cores (D7P5047 and D8P04299) which resulted in incomplete logging details. For this reason, only three lithological logs were completed and are represented in Figure 4.1 to Figure 4.3. The logging descriptions of the incomplete drill cores are, however, included in Appendix A alongside the completed drill cores. The simplified lithology (Figs. 4.1 –4.3) show that the stratigraphy of the Black Reef begins with a medium- to coarse-grained quartz arenite in the hanging wall. The basal quartz arenite has Au grades <2 g/t and the associated pyrite grains are ~0.6 mm in diameter. Progressing up-section, the quartz arenite gradually changes to having scattered, sub-rounded quartz-pebbles defined as the pebbly quartz arenite. The pebbly quartz arenite are generally thick (1.6 m to 16.8 m), are mainly characterised by gold concentrations of ~2 - 5 g/t and have pyrite grains hosted in a black carbonaceous matrix.

There are also areas where these pebbly quartz arenites are interbedded with well-packed, matrix-supported conglomerate units. Conglomerate thickness can range from pebble-rich units that are 1.6 m to 6.4 m thick, alternating with quartz arenite units or occur as single ~8 m thick units. The gold concentration in these units ranges from 5 – 30g/t. The quartz pebbles are embedded in a black carbonaceous matrix with abundant pyrobitumen which frequently occur at the bottom contacts. The conglomerate eventually fines down to a carbonaceous shale with rounded pyrite nodules and pyrite oriented in stringers. The carbonaceous shale units gradually become light grey in colour and interbedded with fine-grained sand. In places, the carbonaceous shale is intercalated with gold-rich conglomerates (Fig. 4.2 and 4.3) with quartz-pebbles that are ~1.7 cm in diameter, and these carbonaceous shales contain graphite in the matrix. The quartz-pebbles have black wavy fractures and white quartz-pebbles surrounding grey quartz-pebbles (see later Fig. 4.4h).

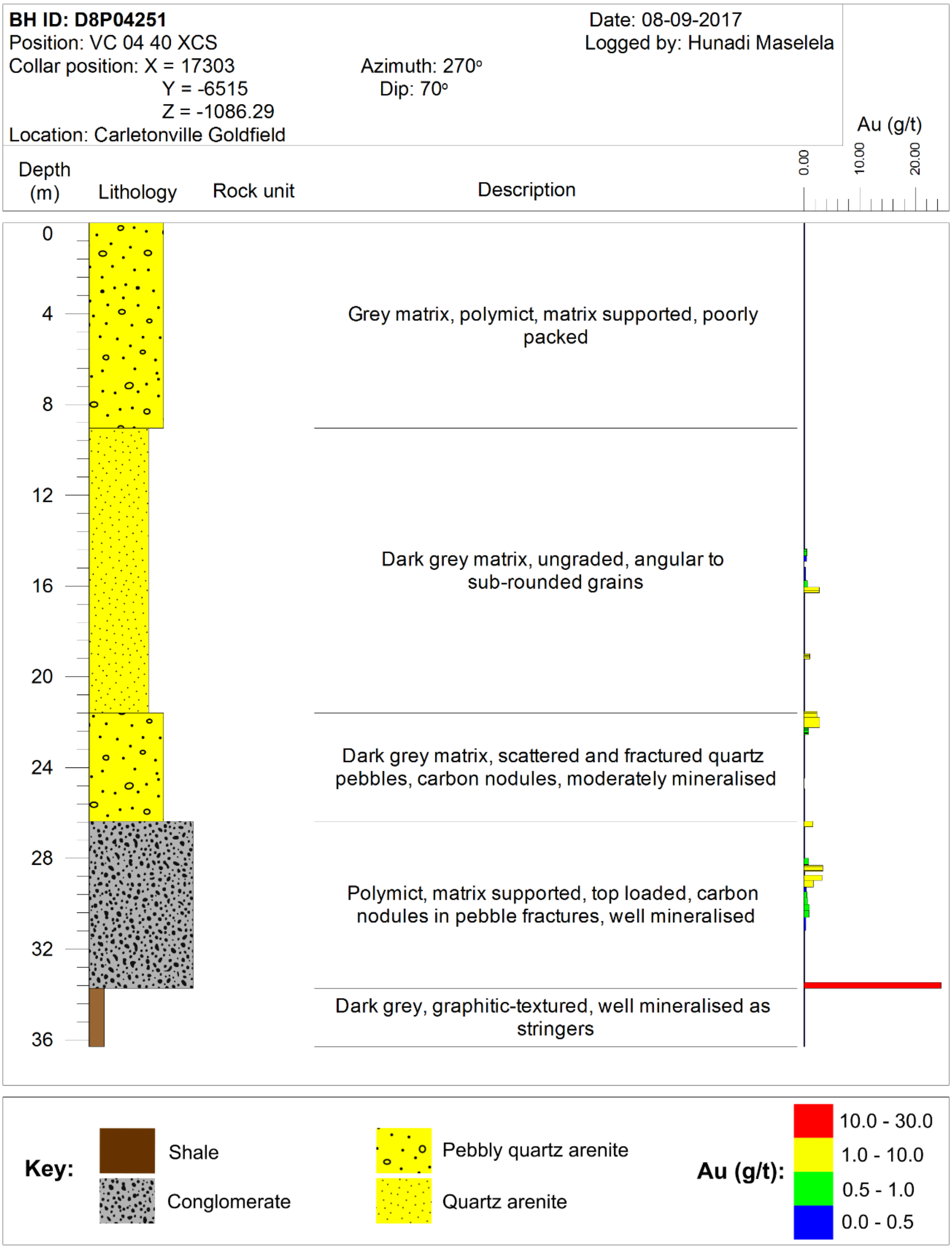

Figure 4.1: Borehole D8P04251 from the Carletonville Goldfield. The bottom contact of the conglomerate bed has the highest Au concentration (24.6 g/t) then grade decreases in the upward-fining sequence to 2.8 g/t and 2.7 g/t for the pebbly quartzite and quartz arenite, respectively.

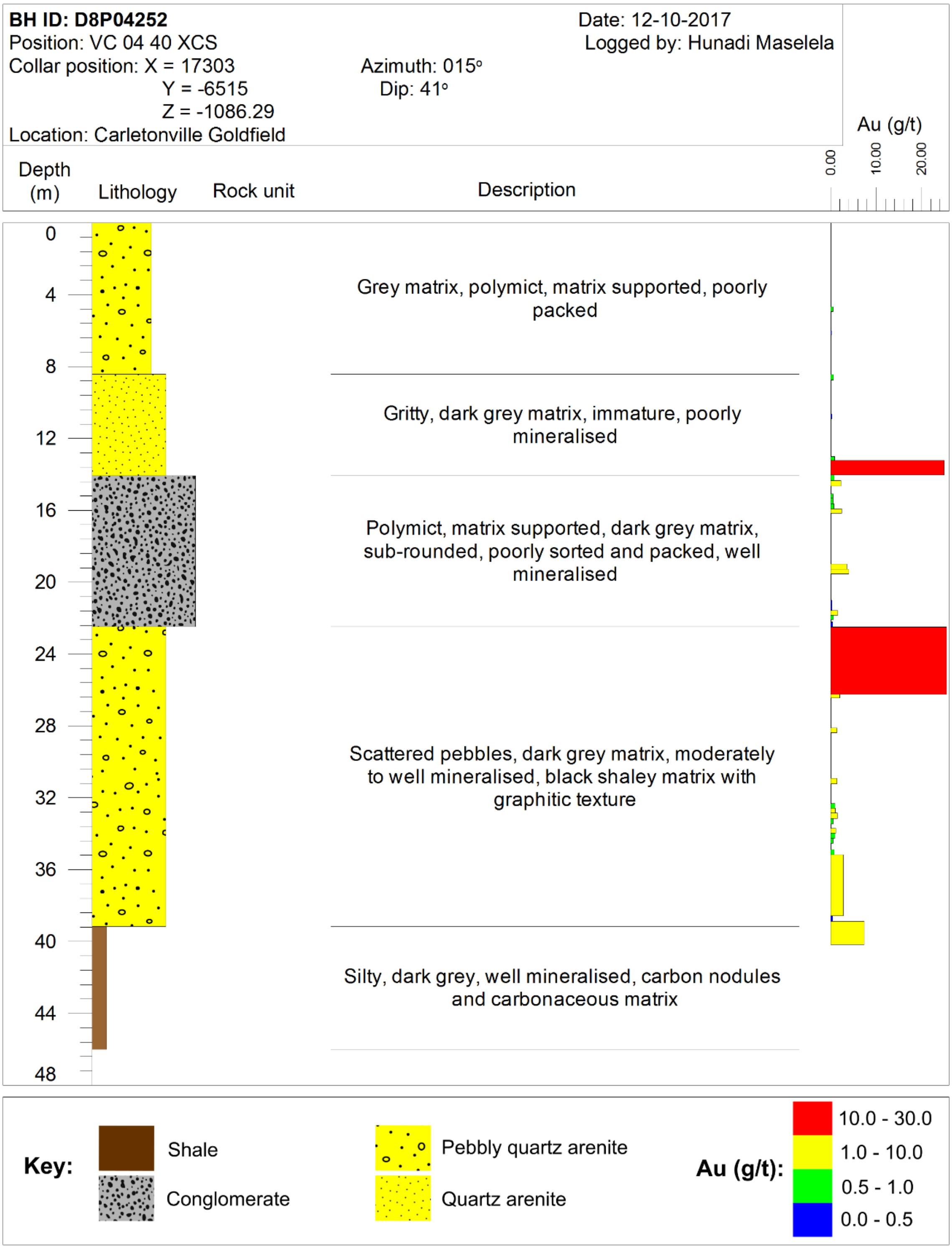

BH ID: D8P04252
Position: VC 04 40 XCS
Collar position: X = 17303
Y = -6515
Z = -1086.29
Location: Carletonville Goldfield
Azimuth: 015°
Dip: 41°
Date: 12-10-2017
Logged by: Hunadi Maselela

Depth (m)	Description
0–8	Grey matrix, polymict, matrix supported, poorly packed
8–13.5	Gritty, dark grey matrix, immature, poorly mineralised
13.5–22	Polymict, matrix supported, dark grey matrix, sub-rounded, poorly sorted and packed, well mineralised
22–39	Scattered pebbles, dark grey matrix, moderately to well mineralised, black shaley matrix with graphitic texture
39–46	Silty, dark grey, well mineralised, carbon nodules and carbonaceous matrix

Figure 4.2: Borehole D8P04252 from the Carletonville Goldfield. This upward-coarsening sequences has the highest Au grades at the upper contact of the conglomerate (Au = 24.9 g/t) and at the upper contact of the lower pebbly quartzite (Au = 25.5 g/t), enveloping the conglomerate bed. Generally, the pebbly quartzite has Au grade of up to 2.7 g/t while quartz arenite has low grades of up to 0.9 g/t.

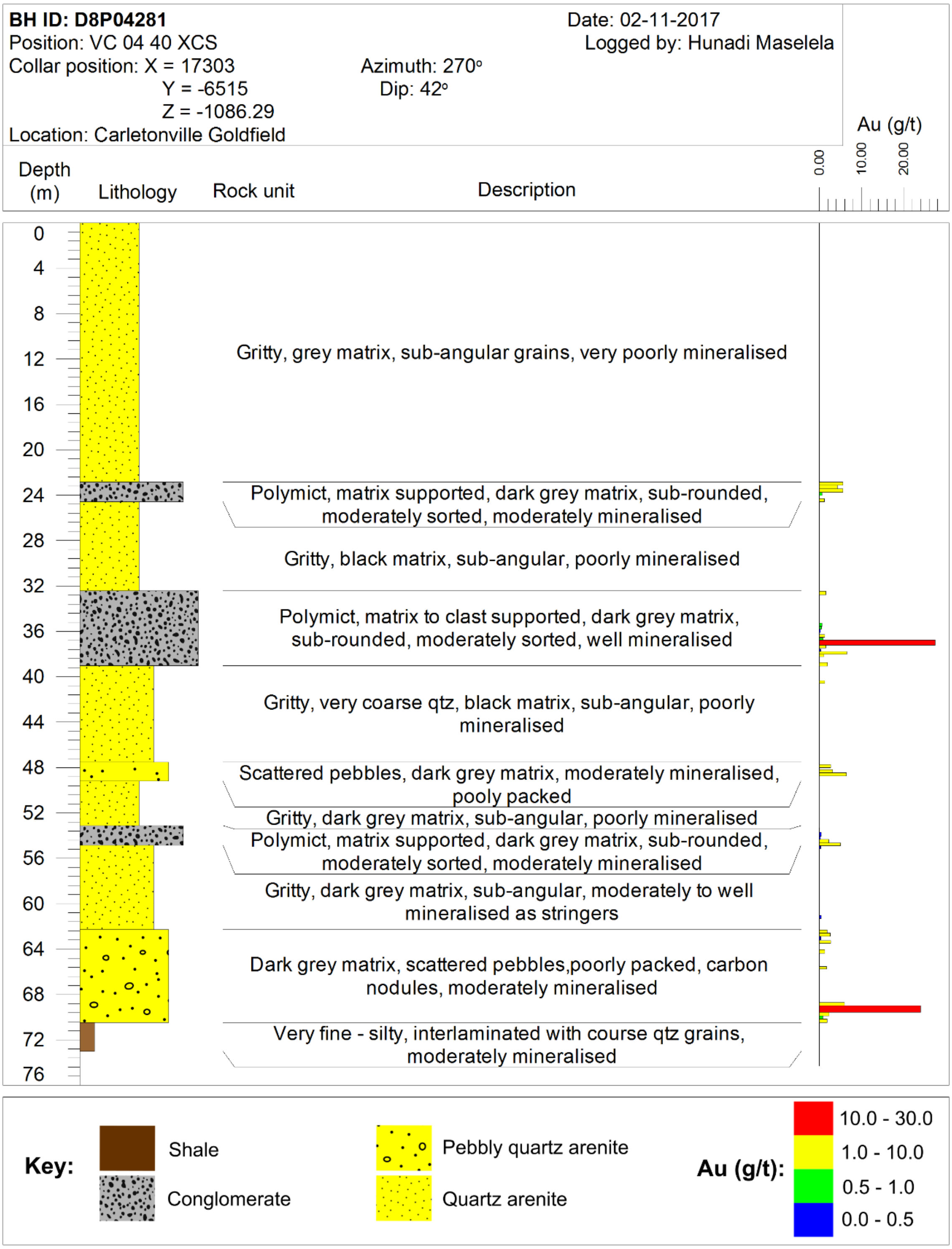

Figure 4.3: Borehole D8P04281 from the Carletonville Goldfield. This borehole shows multiple cycles of high to medium grade conglomerate beds (27.5 – 5.6 g/t), high grades for pebbly quartzites (6.4 – 26.8 g/t). Quartz arenites are barren from any gold mineralisation.

4.2 Sedimentological and petrographic characterisation of the rock units

Sedimentological studies of the samples indicated three main rock types of the Black Reef Formation; (1) carbonaceous shale, (2) quartz arenite and (3) conglomerate. Each of these rock types have similar mineralogy but at different sizes, abundances and textures. Petrographic analyses of the samples from the Black Reef indicate a quartz-muscovite-pyrite-gold-carbon phases-sphalerite-chlorite mineral assemblage. Minor phases of galena, rutile, chalcopyrite and zircon have also been documented in the samples from the Black Reef using SEM (Appendix B). Drennan et al. (1999) and Phillips and Law (2000) have also documented similar assemblages in the Witwatersrand reefs.

4.2.1 Carbonaceous shale

The strata underlying the basal conglomerate unit of the Black Reef Formation (footwall) is made up of carbonaceous shale. The carbonaceous shale normally has very-fine-grained sand to silty grains that are 0.004 – 0.063 mm in size. The carbonaceous shale is mostly grey in colour, and in places directly below the reef, it is shiny black in colour due to the presence of carbonaceous material, and very rarely contains graphite (Fig. 4.4a). The graphite has a shiny lustre and leaves a black streak on hands and on a streak plate. This carbonaceous shale is intercalated with pebbly quartz arenite and conglomerate (Fig. 4.4b, c). This lithology rarely contains pyrite mineralisation along bedding, with up to 5 % modal abundance in some places. The upper lithologies contain carbonaceous shale beds that are intercalated with mudstone and are well-mineralised with rounded pyrite nodules that are up to 1.5 mm in diameter. Non-mineralised shales are grey-green in colour and contain calcite and quartz veins that show micro-faults.

Carbonaceous shale samples are characterised by having sub-angular, fine-grained quartz embedded in a silty matrix. They commonly show bedding and layering which are slightly faulted or showing minor soft sediment deformation (Fig. 4.4d). The matrix of the carbonaceous shale is commonly black in colour in plane-polarised light indicating a high amount of carbonaceous material (Fig. 4.4e, f) and is seldom accompanied by irregular-shaped pyrite (Fig. 4.4g). This carbonaceous material surrounds quartz grains at their boundaries (Fig. 4.4i) and exhibits a fluid-like texture that extends throughout thin section scale. The coarser quartz grains in this carbonaceous shale also have quartz overgrowth and show late-stage microfaulting (Fig. 4.4j).

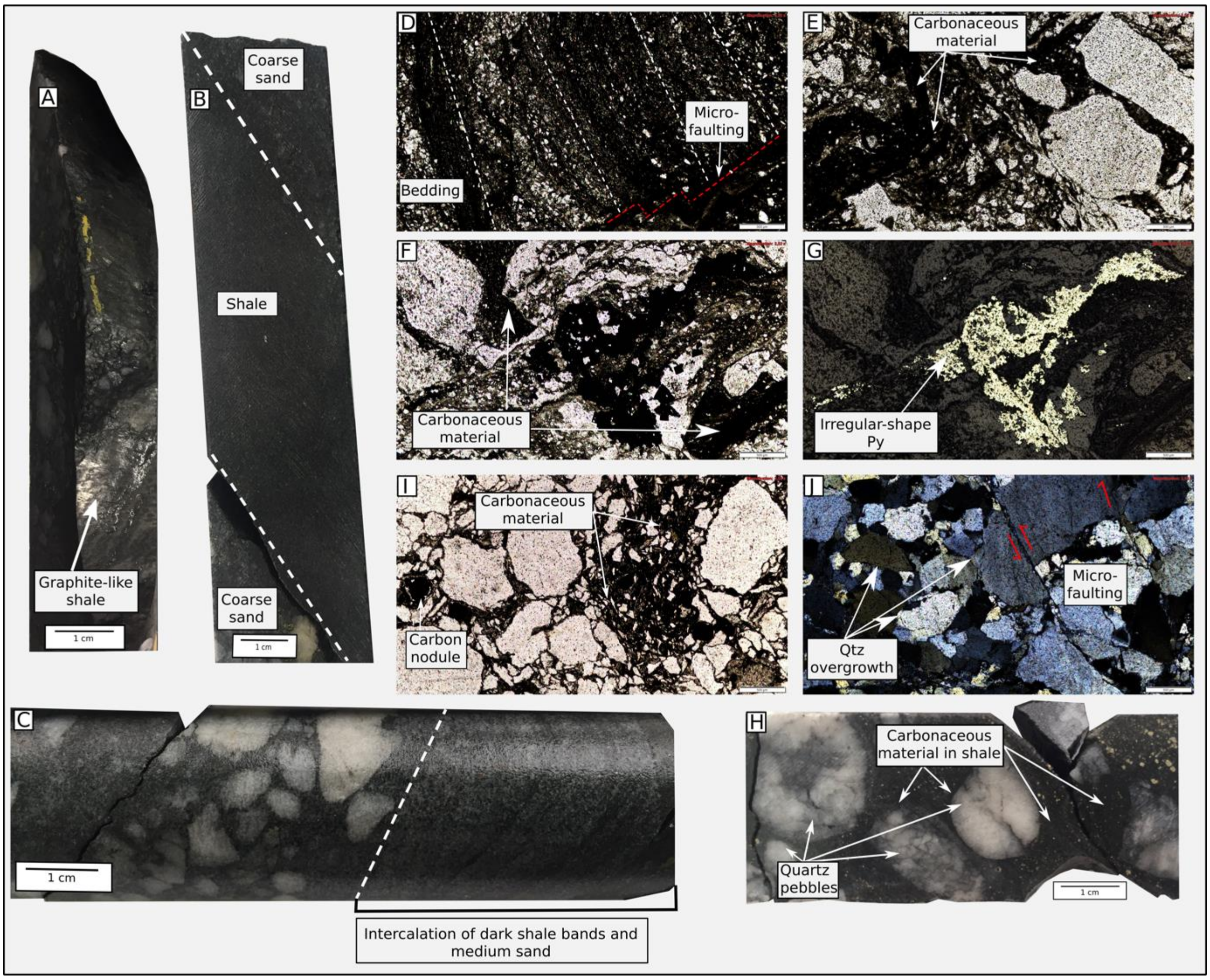

Figure 4.4: Hand samples (scale = 1 cm) and photomicrographs (scale = 500 µm) of the Black Reef carbonaceous shale units. (A) Graphite found in the carbonaceous shale – the shiny lustre shows the presence of graphite in the shale. (B and C) Dark coloured shale bands intercalated with medium- to coarse-grained sand. (D - I) Carbonaceous material (in black) going through very –fine grained quartz. Carbonaceous material carries irregular-shaped pyrite. (J) Quartz overgrowth and late stage microfaulting of quartz grains. (H) Carbonaceous shale intercalated with gold-rich conglomerate.

Figure 4.5 shows a characteristic carbonaceous shale hand sample and microphotographic images of a portion of the hand specimen in transmitted light and reflected light. The transmitted light shows quartz grain size variation from the bottom-up: grain size decreases from fine- to silty grains towards the carbonaceous material. This carbonaceous material encloses a polycrystalline quartz grain. There are scattered polycrystalline quartz-pebbles, and pyrite grains that are generally cubic-shaped indicative of formation under hydrothermal conditions.

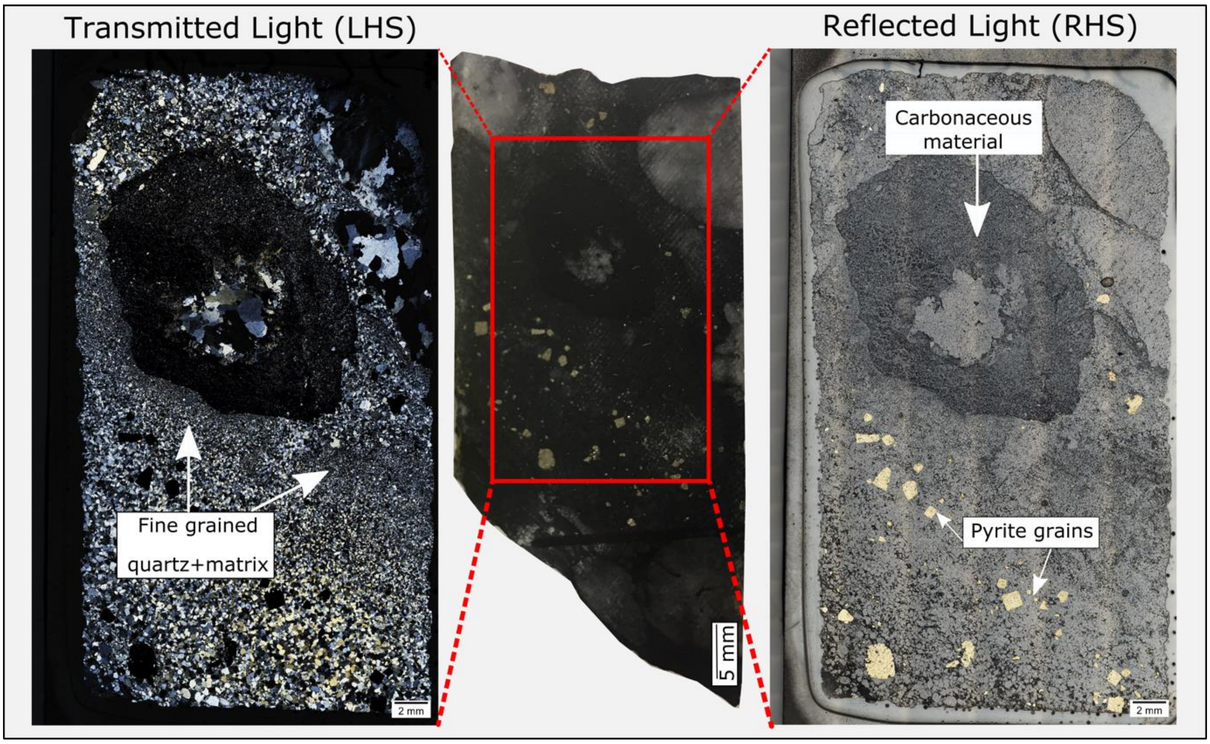

Figure 4.5: Typical hand specimen sample TK-52-36 of carbonaceous shale with scattered quartz-pebbles from the Black Reef (middle). The main features show silty quartz grains surrounding carbonaceous material that encloses a polycrystalline quartz grain. Most of the pyrite grains in this rock unit are cubic. Scale is 5 mm on the core sample and 2 mm on the full thin section images.

4.2.2 Quartz arenite

The strata overlying the basal conglomerate unit of the Black Reef Formation (hanging-wall) is characterised by a quartz arenite with gritty grains and fine- to very-coarse-grained sand that ranges from 0.125 – 1.000 mm in size (Fig. 4.6a). The quartz grains are sub-angular to angular. Quartz arenites that are further from the highly mineralised conglomerate units have a light to dark grey matrix, immature sediments and are poorly mineralised. However, quartz arenites that are proximal to the conglomerate units are mature sediments, have a black carbonaceous matrix and are generally moderately mineralised with pyrite grains (up to 15 % modal abundance) parallel to bedding planes. The pyrite mineralisation also runs along bedding foresets and cross-beds and occurs as pyrite stringers, indicative of synsedimentary mineralisation (Fig. 4.6b, c).

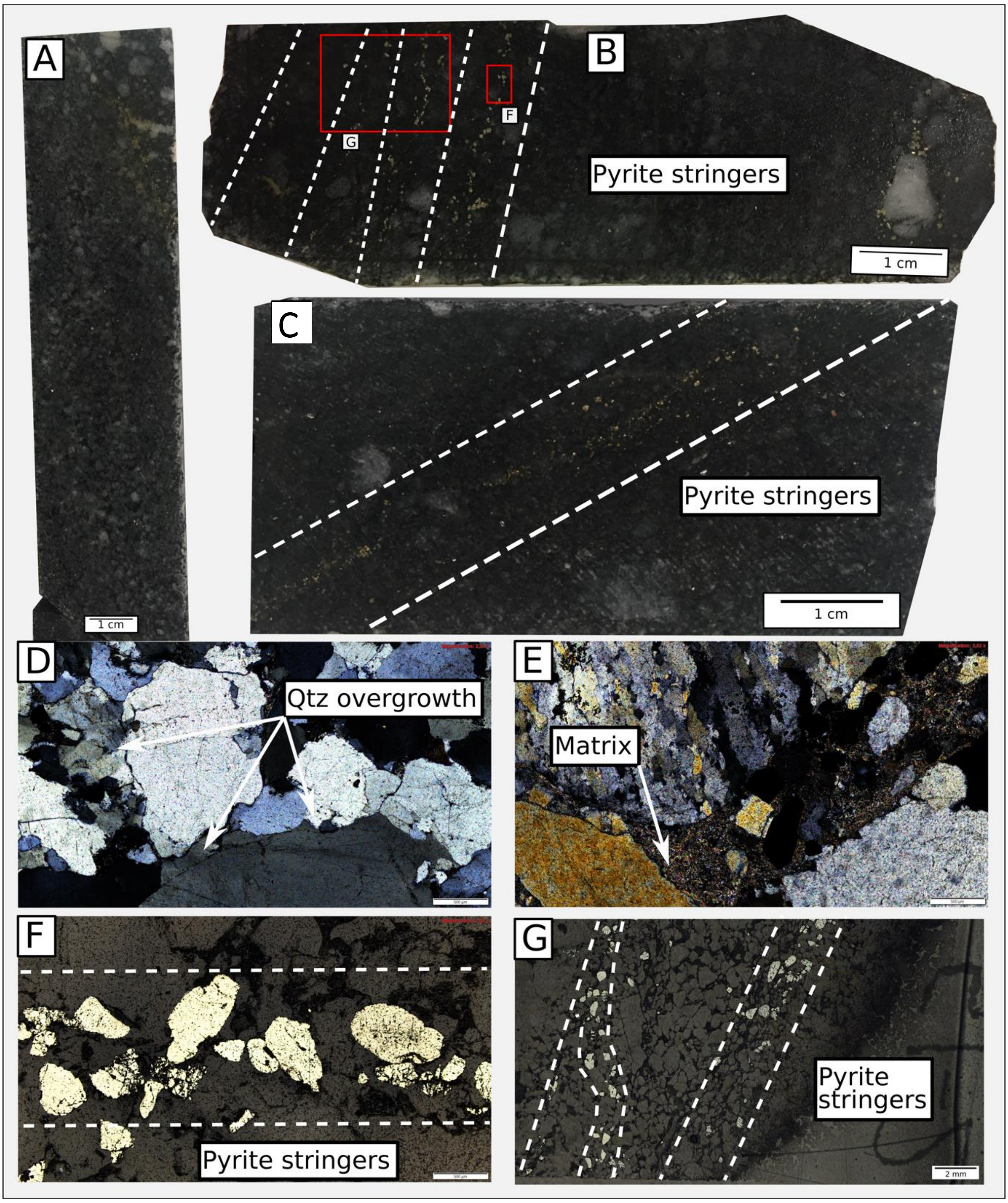

Figure 4.6: Hand samples (scale = 1 cm) and photomicrographs (scale = 500 µm) of the Black Reef quartz arenite units. (A) Gritty quartz arenite. (B) Scattered quartz-pebbles in a quartz arenite and pyrite mineralisation parallel as stringers. (c) Pyrite stringers along bedding foresets. (D) Quartz grains boundaries with quartz overgrowth causing annealing texture (scale = 500 µm). (E) Minor clay minerals in the matrix (scale = 500 µm). (F, G – red inserts in B) Different pyrite grains aligned as stringers at thin section scale (scale = 500 µm in F, 2mm in G).

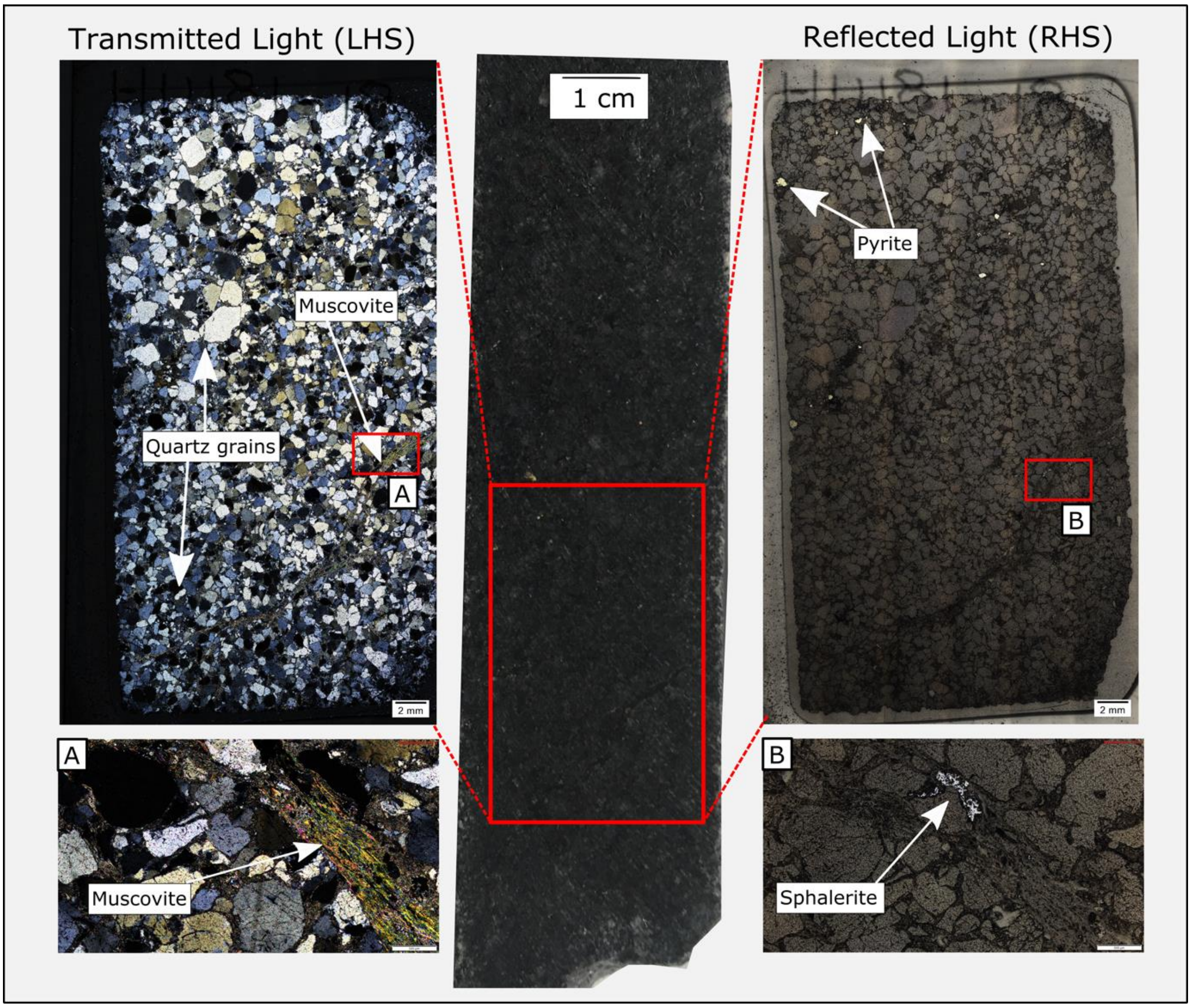

Figure 4.7: Typical hand specimen sample HM-81-18 of quartz arenite from the Black Reef (middle). The main features show that the quartz arenite contain sub-angular to angular and gritty quartz grains (middle), with closely packed quartz grains with minimum clay minerals in the matrix (left-hand side – transmitted light) and very few pyrite mineralisation (right-hand side – reflected light). (A) Muscovite grain extends the entire width of the thin section and exhibits a schistose texture. (B) Sphalerite grain found along the muscovite. Scale is 1 cm on the core sample, 2 mm on the full thin section images and 500 µm on the detailed photomicrographs.

Fine-grained quartz grains that are often aligned in a parallel orientation dominate the quartz arenite units. This indicative of the bedding orientation and sediment sorting. The quartz grains are typically sub-rounded to angular, mostly monocrystalline and surrounded by a brown, fine-grained matrix. There is the presence of annealing; where quartz grains are in contact with one another (Fig. 4.6d), and minor strained quartz grains enclosed by a clay-rich matrix (Fig. 4.6e). On the microscopic scale, pyrite grains are also observed aligned as stringers parallel to bedding (Fig.4.6f, g).

Figure 4.7 shows a typical characteristic core hand sample of a quartz arenite unit and microphotographic images on a portion of the hand specimen in transmitted light and reflected light. The transmitted light shows medium- to fine-grained, sub-rounded quartz grains that are compacted with an elongated muscovite grain exhibiting schistosity (Fig. 4.7a). The reflected light emphasises the often-poor pyrite mineralisation in these units, where pyrite grains are often scattered or may be aligned parallel to bedding, with minor sphalerite (Fig. 4.7b).

4.2.3 Conglomerate

Black Reef conglomerate is characterised by granular- to pebble-sized quartz grains and chert grains that are 23 – 45 mm in diameter (Fig. 4.8a – c). The conglomerate is generally moderately- to well-packed and is generally matrix supported. In places where it is clast supported, the sediments are well-sorted, polymictic, have a black carbonaceous matrix and are highly mineralised with pyrite (Fig. 4.8a, b). The quartz-pebbles are embedded in a black matrix comprising an abundance of carbonaceous material. Quartz-pebbles are rounded- to sub-rounded and many have fractures commonly filled with rounded and elongated pyrobitumen (Fig. 4.8c, d). Conglomerates are moderately- to well-mineralised with pyrite grains (up to 30% modal abundance) that are up to 1.8 mm in diameter. Pyrite tends to be concentrated around quartz-pebbles (Fig. 4.8a). Where conglomerate is stratigraphically followed by quartz arenite, the quartz arenite is pebbly. This is described as a gritty quartz arenite with scattered and fractured quartz-pebbles. The quartz grains are coarse- to very-coarse grained, ranging from 0.5 – 1.5 mm, while the fractured pebbles are up to ~2.5 mm in diameter. This “pebbly quartz arenite” is poorly to moderately mineralised with pyrite (up to 10 % modal abundance), has a dark grey to black carbonaceous matrix and is an immature sediment. Some of the rounded quartz-pebbles are highly fractured and these fractures have black carbonaceous material running through them (Fig. 4.8e, f).

Conglomerates and pebbly quartz arenites of the Black Reef have large (>5 mm) mono- and polycrystalline quartz grains. The quartz-pebbles are generally rounded to sub-rounded) and contain microfractures (Fig. 4.8g – j). Polycrystalline quartz-pebbles have many quartz grains that go into extinction at different times upon stage rotation (undulose extinction). Some of these polycrystalline pebbles show some deformation by compression or elongation where all the micro-quartz grains are aligned in one direction (Fig. 4.8k). The quartz cracks are at times filled with smaller crystalline quartz grains that may indicate micro-quartz veins that run through the length of the thin section (Fig. 4.8g, i). Irregular-shaped gold and irregular-shaped pyrite grains are located inside these micro quartz veins (Fig. 4.8g – j). The quartz-pebbles also have minor quartz overgrowths, which occasionally have pyrite developing on the overgrowth region (Fig. 4.8l). Edges of some quartz-pebbles show strained quartz while on other pebbles the edges show strained muscovite, indicating schistosity (Fig. 4.8m). Microcrystalline quartz (chert) is present (Fig. 4.8n) and occurs mostly as rounded and elongate grains up to ~2.5 mm in length.

The matrix of the conglomerates and the pebbly quartz arenite are at times light brown and often dark brown in colour and very fine-grained (Fig. 4.8l, n). It comprises secondary quartz, pyrite, muscovite and very seldom chlorite. Sericite is the dominant clay mineral in the matrix formed by the alteration of feldspars, which are no longer preserved. The muscovite occasionally occurs as strained, elongated grains exhibiting schistosity, which is seldom accompanied by irregular-shaped pyrite similar to the quartz arenite. There are places where this matrix material occurs as rounded, ~1.8 mm ‘pebbles’ surrounded by mono- and polycrystalline quartz grains (Fig. 4.8o).

Figure 4.9 shows a typical characteristic core hand sample of a conglomerate unit and full thin section images of a portion of the hand specimen in transmitted light and reflected light. The transmitted light shows rounded polycrystalline quartz grains. They are highly fractured, and they show substantial straining based on the fine-grained brittle extensional fractures in quartz grains near adjacent quartz-pebbles (Fig. 4.9a – c). Along the brittle extensional fractures in quartz grains tiny specks of gold that are randomly orientated (Fig. 4.9d – f).

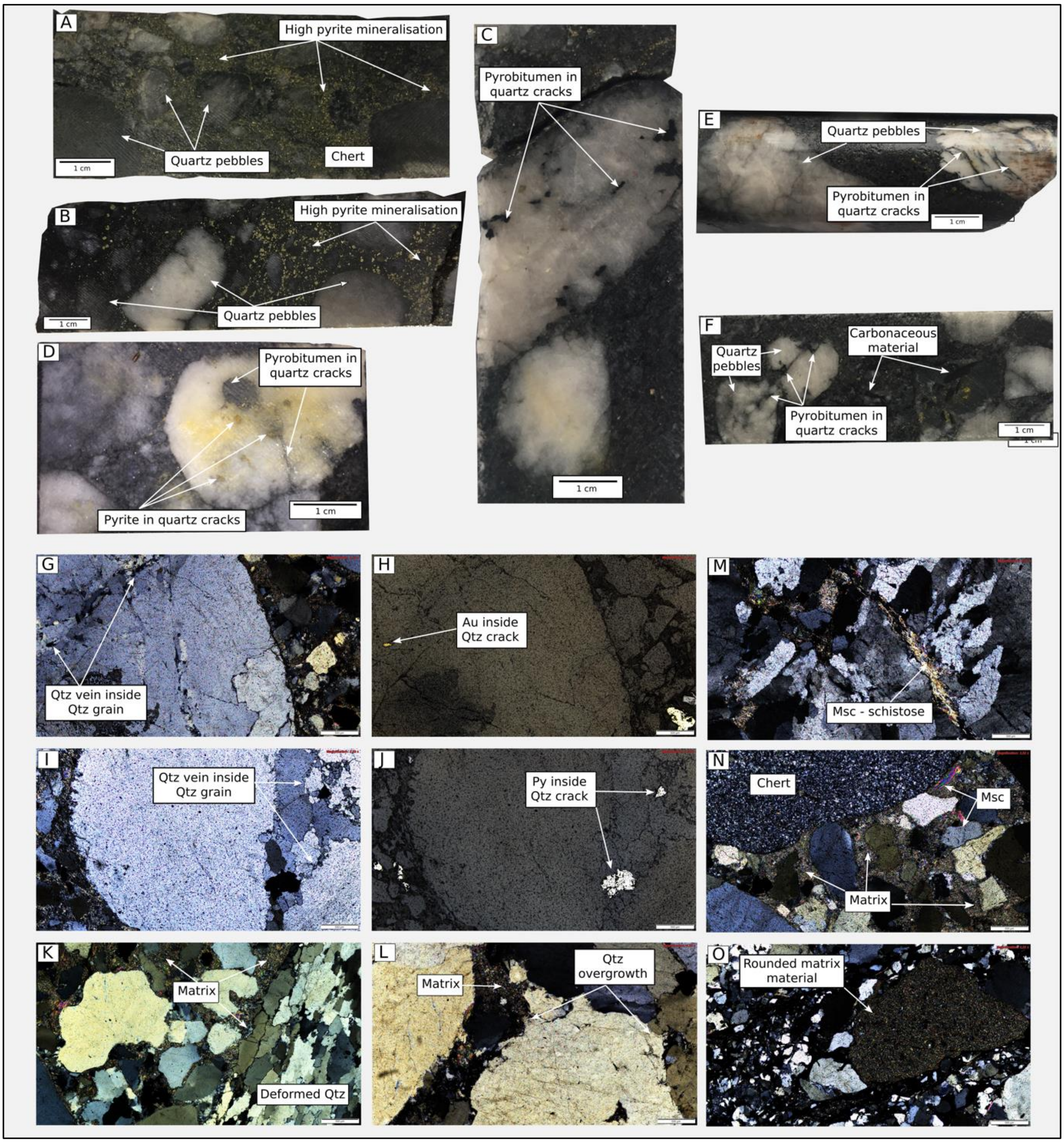

Figure 4.8: Hand samples (scale = 1 cm) and photomicrographs (scale = 500 µm) of the Black Reef conglomerate units. (A and B) High pyrite mineralisation in conglomerate. (C and D) Large quartz-pebbles with cracks filled with pyrobitumen. (E and F) Quartz-pebble fractures filled with carbonaceous material. (G – K) Deformed quartz in conglomerate. Quartz-pebbles have quartz veins carrying irregular pyrite and gold. G is in cross-polarised light and the corresponding image H in reflected light. I is in cross-polarised light and the corresponding image J in reflected light. (L) Quartz overgrowth on rounded quartz to angular shaped. Matrix dominated by mica and clays. (M and N) Presence of muscovite with a schistose-like texture and chert. (O) Rounded matrix material seems to be transported from elsewhere. Qtz = quartz, Msc = muscovite, Py = pyrite, CN = carbon nodule, Au = gold.

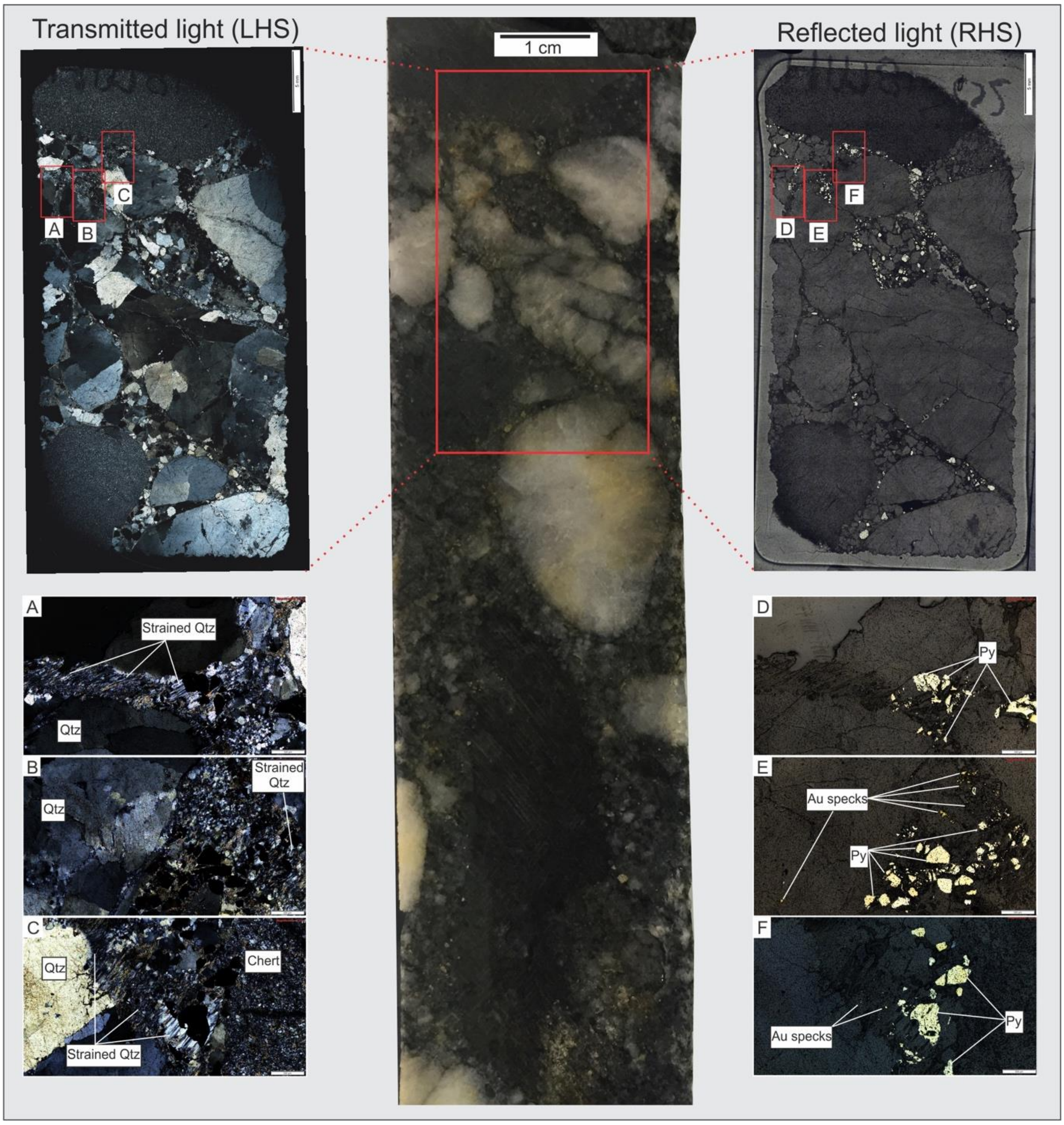

Figure 4.9: Typical conglomerate hand specimen sample HM-81-02 from the Black Reef (middle). The main features show that along strained quartz there are specks of small gold. The area in red on the hand specimen is viewed in transmitted light (left) and reflected light (right). The areas of the smaller red rectangles on the full photomicrographs are placed below to show the textures in detail. (A) Quartz straining along boundaries of quartz grains. (D) the strained areas contain micron-sized, fractured pyrite grains. (B) Strained quartz grains and fractured quartz grains (bottom left). (E) Gold specks located along strained areas of quartz grains and inside quartz fractures. (C) Chert with recrystallised quartz grains and straining of quartz aligned in a single, parallel orientation. (F) Pyrite grains located between quartz grains and chert grains, and gold specks located in the strained areas. Qtz = quartz, Py = pyrite, Au = gold. Scale is 1 cm on the core sample, 5 mm on the full thin section images and 500 µm on the detailed photomicrographs.

4.3 Petrography of the ore minerals

4.3.1 Carbonaceous material

The Black Reef contains carbonaceous material in the form of pyrobitumen. It occurs in four main sub-types:

1. Fracture-filling (~30 % in modal abundance): massive type. Occurs mostly in shale and is graphitic. It often surrounds quartz grains and fills fractures (Fig. 4.4d – 4.4i, Fig. 4.10a)
2. Globular (~15 % in modal abundance): large (up to ~1.5 mm), rounded and generally complex-shaped. They often contain the most irregular-shaped, micron-sized gold and uranium inclusions. They occur in the matrix of conglomerates, quartz-pebble boundaries and inside quartz-pebble cracks (Fig. 4.10b, 4.10d, 4.11a, see earlier Fig. 4.8d)
3. Nodular (~10 % in modal abundance): relatively smaller (up to ~500 µm) and rounded. They do not contain any elemental and mineral inclusions. They occur mostly between quartz grains and in quartz cracks (Fig. 4.10a, 4.10c)
4. Irregular (~15 % in modal abundance): rounded and complex shaped nodules that are ~500 µm in diameter. These often contain inclusions but differ from the nodular ones by having pyrite close to its boundaries or surrounded by pyrite grains (Fig. 4.10e, 4.10f, 4.11b)

SEM imaging was used to identify trace element inclusions within the pyrobitumen and to identify the presence and chemistry of gold and uranium-bearing minerals. The SEM imaging shows that the globular, nodular and irregular pyrobitumen are highly concentrated in C and various heavy elements that are immobile such as Zr, K, Ti, U and minor Au and Ag (Fig. 4.11a). Secondary uranium minerals occur as minor inclusions in these carbon nodules. Most commonly, the carbon nodules contain specks of gold. The carbon nodules are also closely associated with detrital and hydrothermal pyrite grains, shown by the bright AsFe-sulphide phase in the SEM image in Figure 4.11b). Appendix B presents more SEM images of other ore constituents.

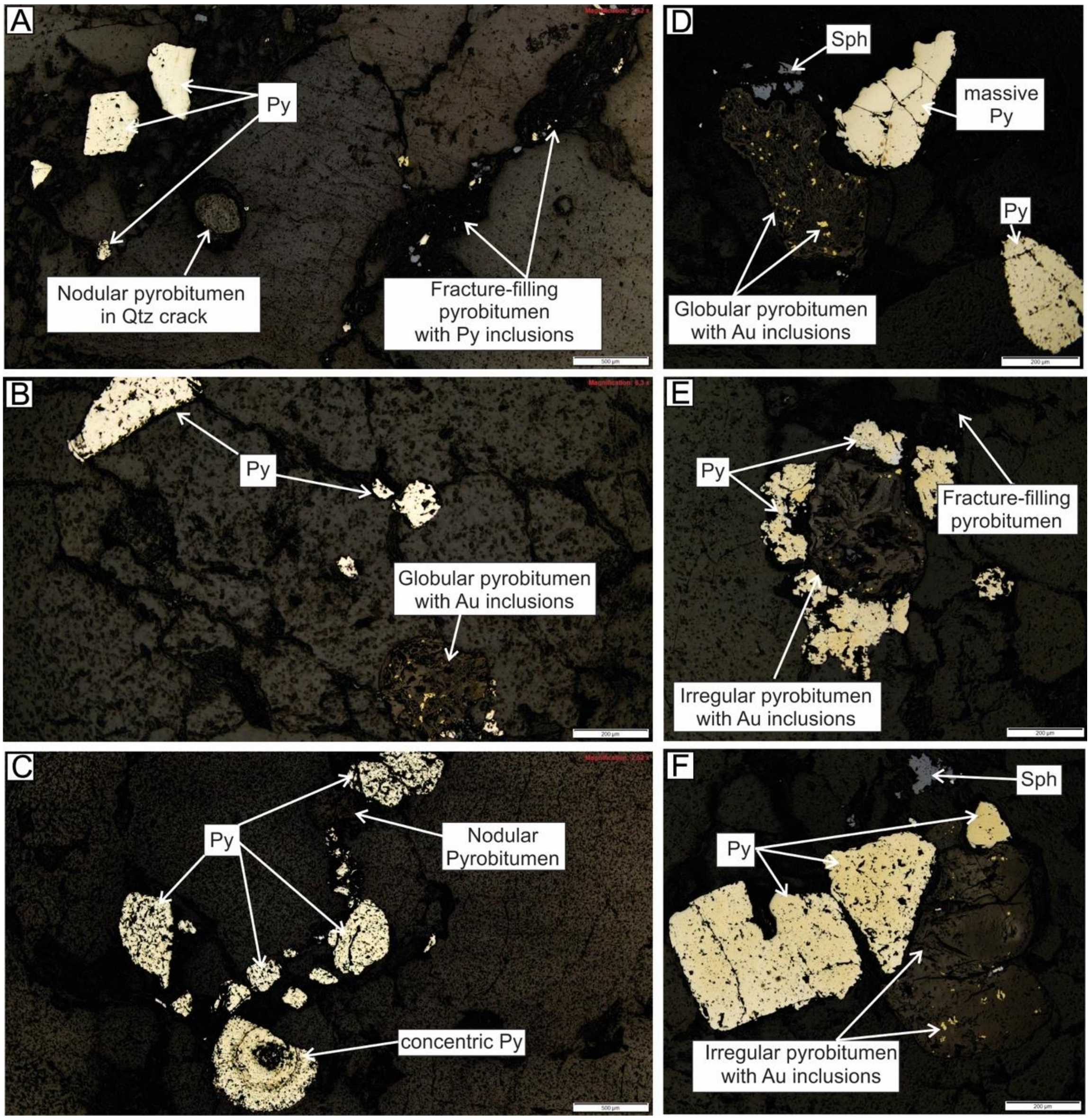

Figure 4.10: Pyrobitumen morphology. (A) Fracture-filling and nodular pyrobitumen. (B and D) Globular with gold inclusion. (C) Nodular. (E and F) Pyrite surrounding irregular pyrobitumen with inclusions. Py = pyrite, Sph = sphalerite, Au = gold. Scale is 500 µm for Figures A and C, and 200 µm for Figures B, D – F.

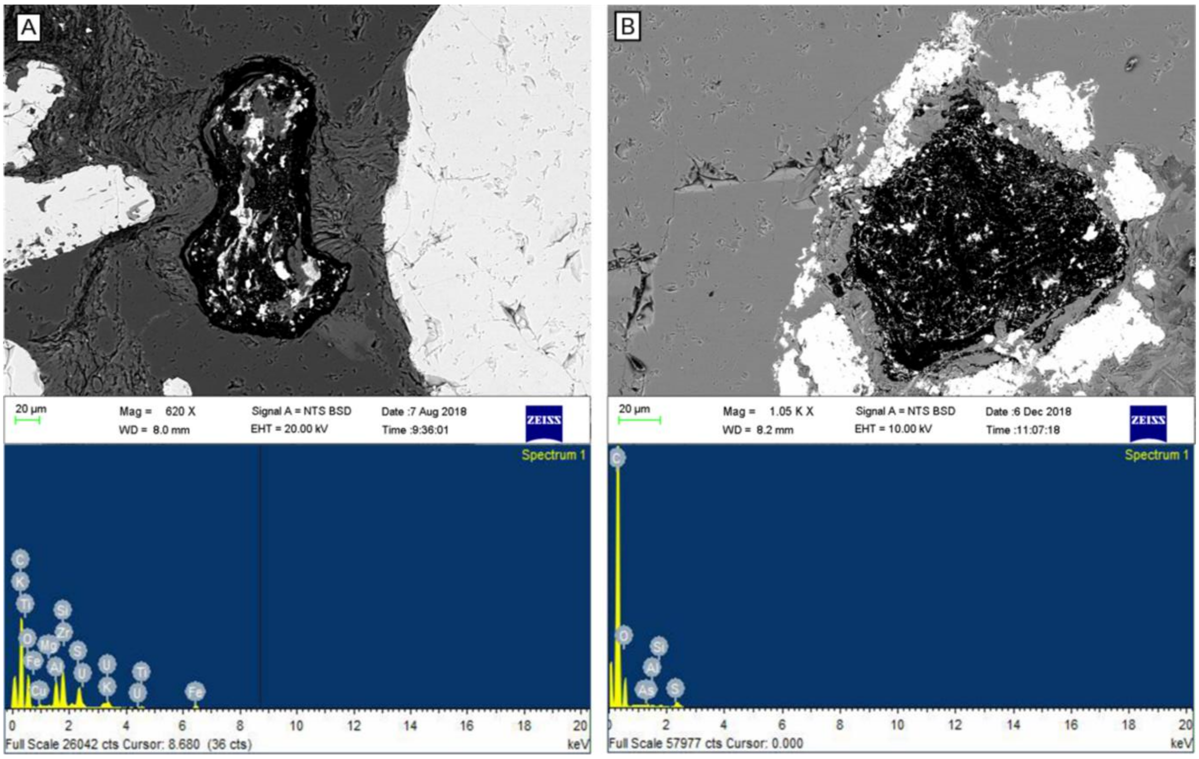

Figure 4.11: SEM images of (A) Globular pyrobitumen in a thin section from sample TK-51-27 from the Black Reef Formation where the pyrobitumen is rounded and the dark/black colour inside delineates light element carbon. The inclusions in the pyrobitumen are brighter phases of heavier immobile elements such K, Ti, Zr and U.(B) Irregular pyrobitumen in a thin section from sample TK-52-20 from the Black Reef there the pyrobitumen is surrounded by a bright phase of AsFe-sulphide. Scale = 20 µm.

4.3.2 Pyrite grains

The most prominent and abundant ore mineral in the Black Reef is pyrite. Pyrite grains make up to 30 % modal abundance and are generally large (up to 2 mm in diameter) and occur in different morphologies. Figure 4.12 depicts different pyrite morphologies occurring together at thin section scale. Pyrite grains occurring in Archaean quartz-pebble conglomerates are divided into two main classes: 1) detrital (or allogenic) pyrite that is derived from recycled intrabasinal sedimentary material, and 2) authigenic pyrite that formed *in situ* after consolidation of the sediments (Costa et al., 2020). Early diagenesis of quartz-pebble conglomerates forms diagenetic pyrite *in situ*, regarded as an authigenic type. This study utilises the classification scheme for detrital and authigenic pyrite in Archaean quartz-pebble conglomerates revised by Costa et al. (2020).

The Black Reef samples show five different pyrite types:

1. Massive detrital pyrite (DM): they are inclusion-poor and are generally irregular-shaped, rounded and cubic with abraded edges (Fig. 4.12a – c, e);
2. Random inclusion-bearing detrital pyrite (DIR): “porous”, with ~>10 % randomly distributed inclusions in the grains. They are generally irregular-shaped and rounded (Fig. 4.12a, b, d – g);
3. Concentrically laminated detrital pyrite (DIC): “oolitic”, spherical or fragmented. They are rounded and consist of concentric sets of laminae with inclusions between the interstices of the laminae and in the grain (Fig. 4.10c, Fig. 4.12f, g,);
4. Euhedral / subhedral authigenic pyrite (AE): cubic crystals, generally massive in texture but may have ~<10 vol% of inclusions (Fig. 4.5, Fig. 4.12b, e, g); and
5. Authigenic pyrite overgrowth (AO): overgrowths on rounded and abraded massive detrital pyrite grain, core-rim structure present and is generally massive (Fig. 4.12c)

The DM and DIR pyrite types are the most abundant and occur in all Black reef lithologies. These pyrite grains range from micron size to ~1.8 mm. A few pyrite grains show overgrowth from an abraded detrital cubic pyrite grains to a more irregular-shaped pyrite (Fig. 4.12c). The detrital pyrite grains DM and DIR are commonly aligned as stringers parallel to bedding (Fig. 4.12e, Fig. 4.6f, g). Sphalerite is the second common sulphide mineral but does not occur frequently. It is mostly associated with the matrix and carbonaceous material and is normally irregular-shaped.

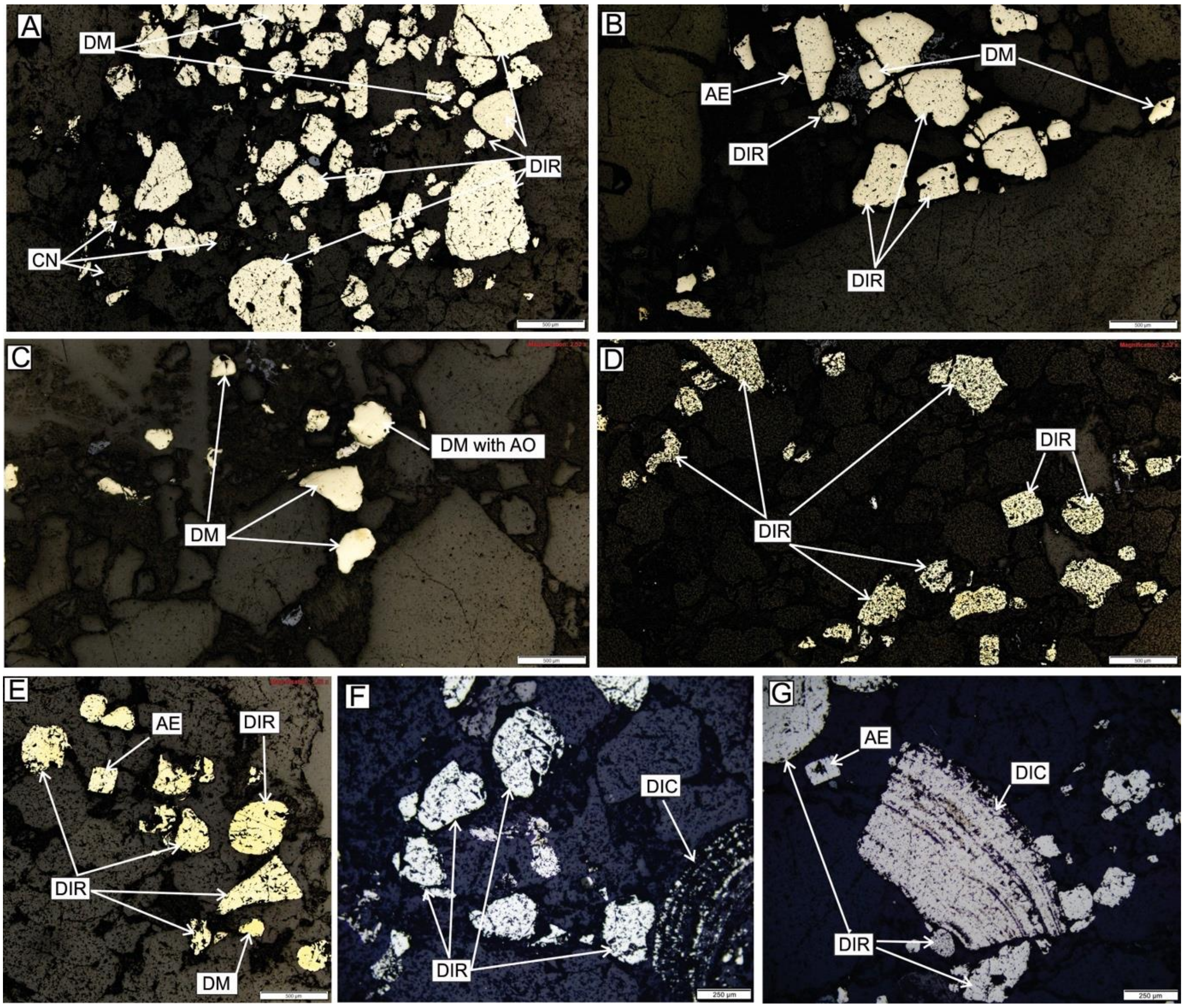

Figure 4.12: Different pyrite morphologies in the Black Reef samples. CN = carbon nodule; DM = massive detrital pyrite, DIR = random inclusion-bearing detrital pyrite, DIC = concentrically laminated detrital pyrite, AE = euhedral / subhedral authigenic pyrite, AO = authigenic pyrite overgrowth. Scale is 500 µm for figures A – E and 250 µm for figures F and G.

4.3.3 Gold

Gold is commonly associated with the conglomeratic samples. It is irregular-shaped and generally occurs as elongated grains occurring in quartz microfractures (Fig. 4.13a, 4.13b) and as inclusions in detrital pyrite grains. Gold also occurs at the boundaries of euhedral authigenic pyrite grains and rounded detrital pyrite grains as hydrothermal gold (Fig. 4.13c, 4.13e) and as tiny specks at the sites of the fine-grained brittle extensional fractures in quartz grains (Fig. 4.13d). Figure 4.14 indicates irregular-shaped gold inside pyrite grains and at pyrite grain boundaries, also comprising minor Ag and Pb.

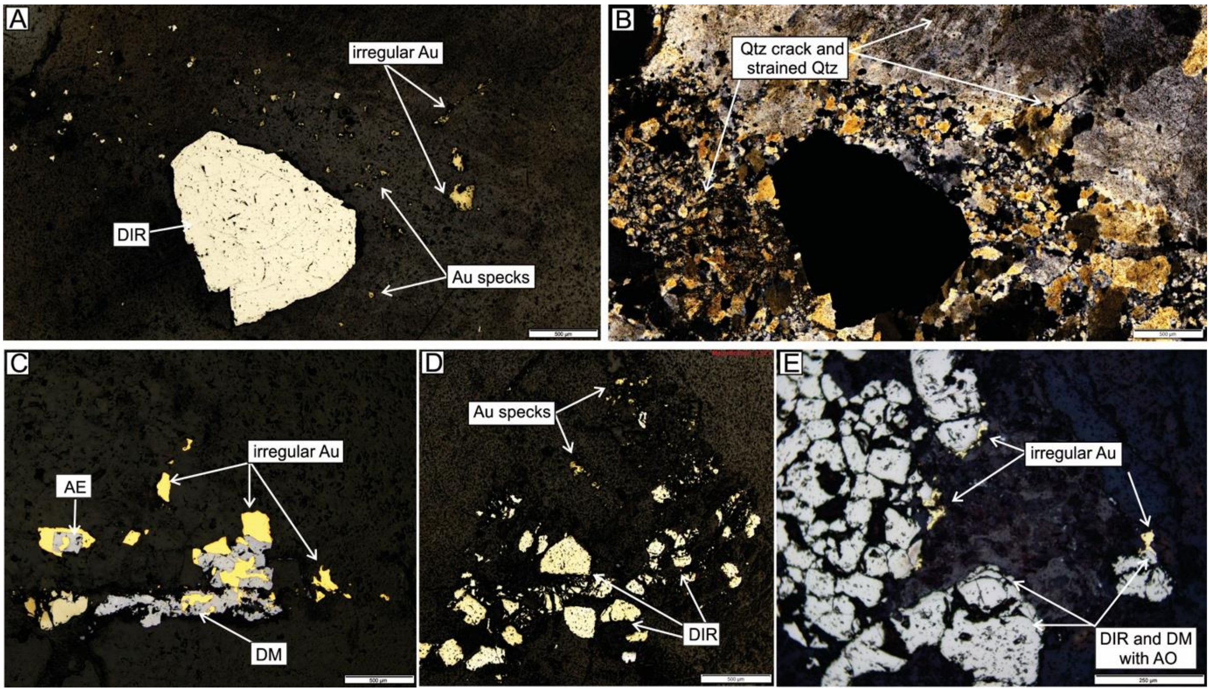

Figure 4.13: Gold morphology and occurrence in the Black Reef conglomerates. (A, B, D) Gold occurring in quartz microfractures as elongated hydrothermal grains and where quartz is strained the gold occurs as micro specks. (C and E) Gold occurring along boundaries of detrital and authigenic pyrite grains. DIR = random inclusion-bearing detrital pyrite, DM = massive detrital pyrite, AE = euhedral/subhedral authigenic pyrite. Scale is 500 µm from Figures A – D and 250 µm for Figure E.

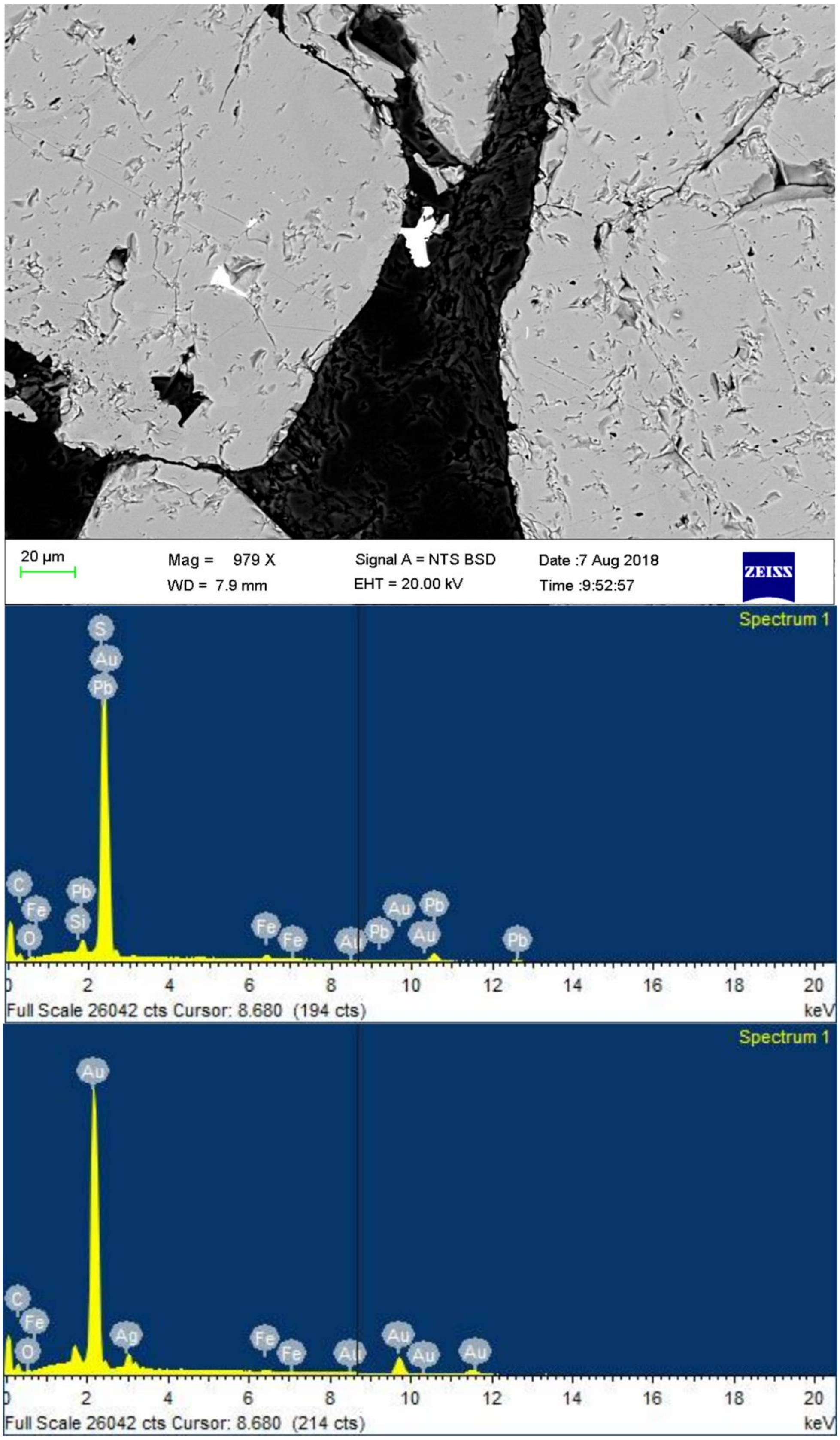

Figure 4.14: SEM images of gold in thin section from sample TK-51-27 from the Black Reef Formation where the bright phase in the dark, carbonaceous matrix and inside pyrite grain fractures is gold. Typically, gold fills fractures, is found as inclusions in pyrite grains and occurs as irregular shaped grains. Scale = 20 µm.

4.4 Fluid inclusions and microthermometry characterisation

4.4.1 Fluid inclusion characterisation

Information such as temperature, pressure, salinity, density and depth of trapping is provided by fluid inclusion analysis, which in turn provides direct information about the conditions at which minerals and rocks are formed (Randive et al., 2014). Fluid inclusion microthermometry was performed on (1) the interior of quartz grains, (2) along microfractured quartz grains, and (3) quartz grains associated with carbon nodules and pyrite grains. The diverse selection of targets was made to note any similarities and/or differences in the fluid inclusions from varying locations of quartz grains. These targets aided in recognising areas with specific fluid inclusion generations and their composition. Microthermometric data from this study is presented in Appendix C.

Analysis shows that most of the fluid inclusions at room temperature (25 ^{o}C) are two-phase inclusions consisting mostly of ~3:1 and 3:2 liquid:vapour ratio, here classified as Type I (Fig. 4.15). Type II inclusions (Fig. 4.9e, 4.10b) are also two-phase inclusions at room temperature and where the liquid:vapour ratio is ~2:3, while Type III inclusions (Fig. 4.15d) were identified as mono-phase inclusions containing only a liquid phase at room temperature. Three-phase inclusions were not visible at room temperature, however Raman spectra (see section 4.4.3) indicate the presence of CO_2 peaks in this Type IV inclusions. Upon cooling, all inclusion types freeze and form microcrystals, but on heating, the vapour-phase in Type I and II inclusions reforms and disappears at their respective homogenisation temperatures. However, the Type III inclusions are metastable inclusions, requiring sophisticated methods (repeated heating and cooling) to produce the vapour phase in the lab (Chi et al., 2021). As such, the final ice melting temperature for the metastable state is higher than the stable ice melting temperature, and therefore cannot be used to calculate salinity from an equilibrium phase diagram (Chi et al., 2021). The methods required to produce the vapour could cause overheating and possible decrepitating the inclusion and produce inconclusive data.

Type I inclusions make up 96% (possible inclusion on Type IV inclusions) of the studied inclusions and occur in various shapes and sizes. Most of them are rounded and elongated (Fig. 4.15a, 4.15b, 4.15d, 4.15f) while others are irregular (Fig. 4.15c, 4.15e). The rounded inclusions are either randomly orientated or occur as inclusion trails (Fig. 4.15d, 4.16a-4.16c). Quartz microfractures are also populated by fluid inclusions, but more commonly the inclusions are aligned as trails sub-parallel to (Fig. 4.15e), and at obtuse angles to (Fig. 4.15c, 4.15f, 4.16f), the fracture orientation. The inclusions occur as a trail or a cluster of irregular-shaped inclusions away from quartz microfractures (Fig. 4.16a, 4.16c, 4.16d). Fluid inclusions that are in proximity (<10 µm) to pyrite grains are smaller than 4 µm (Fig. 4.16e), however, the average width of the inclusions is 9.1 µm (σ = 4.5 µm).

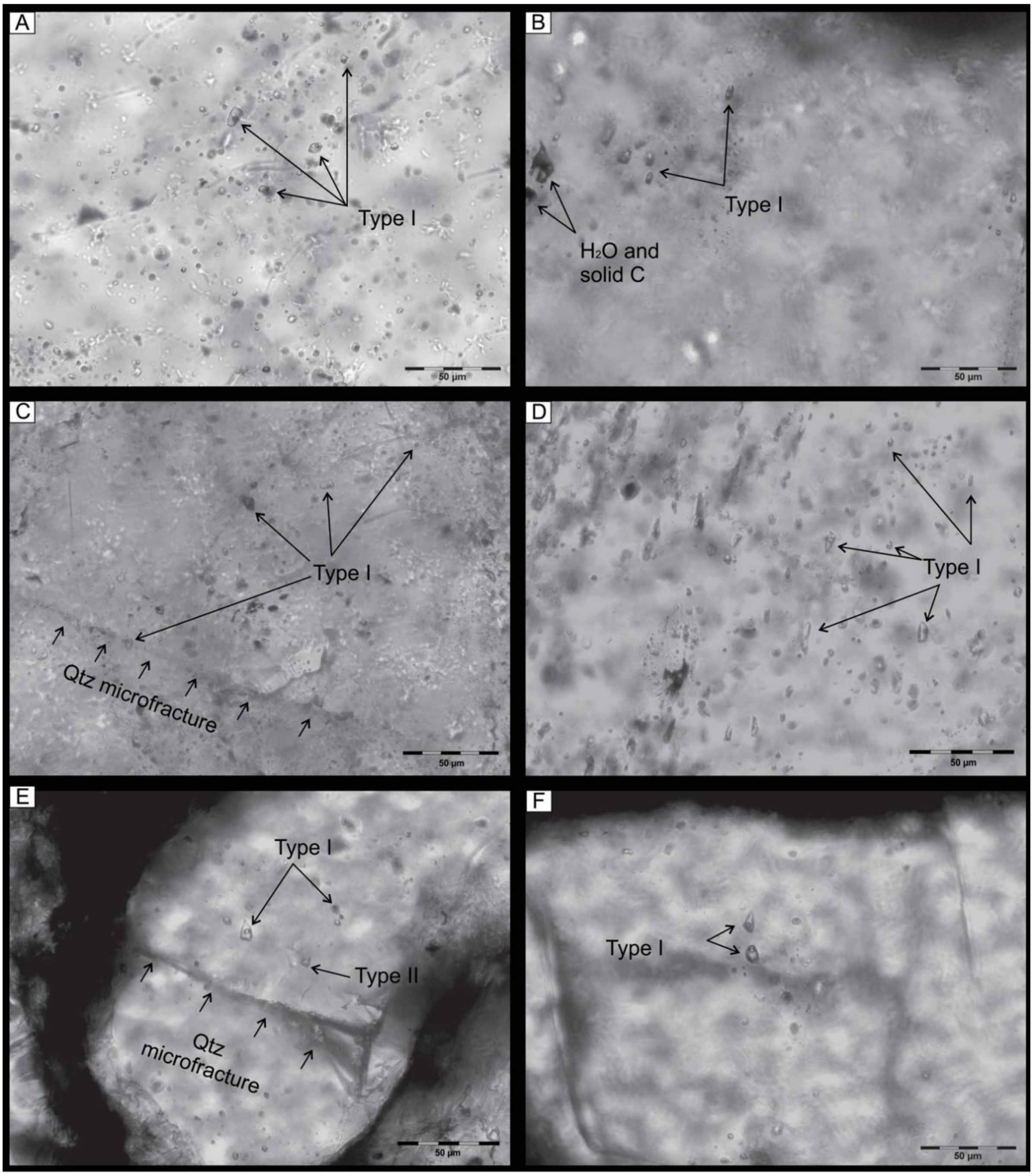

Figure 4.15: Fluid inclusion petrography (at 25 °C). Majority of these fluids are two-phase (type I – vapour phase surrounded by a liquid phase). Fluid inclusions are randomly orientated and aligned sub-parallel and oblique to quartz microfractures. (A, B, D, F) Rounded and elongated inclusions, randomly orientated. (C and E) Inclusions oblique to microfractures. C = carbon, Qtz = quartz. Scale in the inclusions is 50 µm.

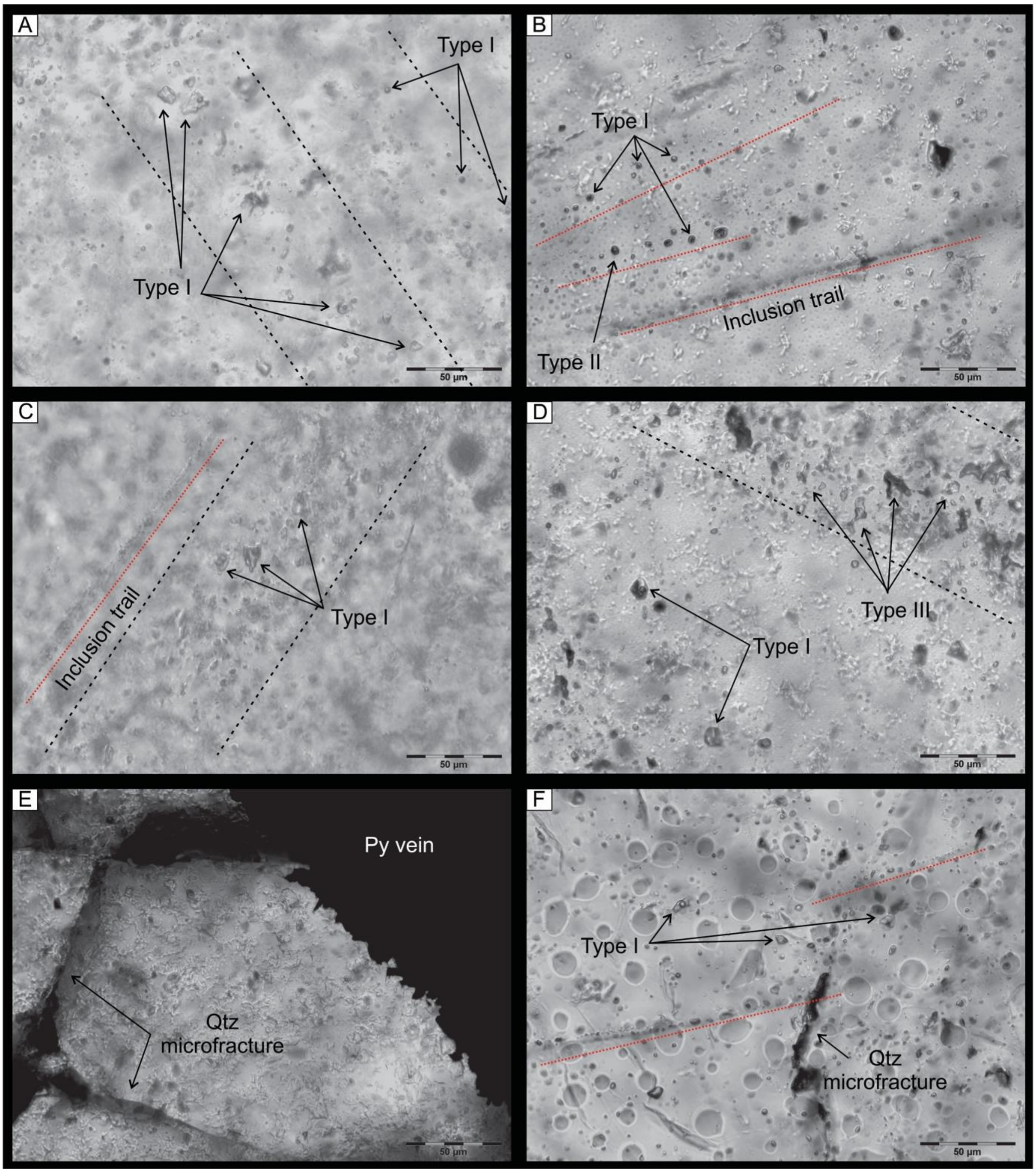

Figure 4.16: Structures in fluid inclusions (at 25 °C). The inclusions are mostly orientated in a cluster that is a in a trail (a, c, d) and in single file trails (b, f). Fluid inclusions close to pyrite veins are much smaller in size (e). The globules seen in (f) is steam / droplets from the liquid Nitrogen during analysis. Qtz = quartz, Py = pyrite. Scale in the inclusions is 50 µm.

4.4.2 Fluid inclusion microthermometry

Microthermometric results are represented in Figure 4.17 as histograms of homogenisation temperature and salinity. The results reveal a large range of homogenisation temperatures from 114 °C to 270 °C ($\bar{x}$ = 172 °C, σ = 30) (Fig. 4.11a) and a constrained range in the freezing point temperature from -16 to -0 °C ($\bar{x}$ = -5 °C, σ = 4). Salinity and density of the fluid inclusions was calculated by inputting the homogenisation and corresponding freezing point temperature into the *HOKIEFLINCS_H2O-NACL* excel programme derived by Steele-MacInnis et al. (2012). As indicated, Type III inclusions produced inconclusive data for salinity and density due to the metastability of the inclusions. As such, this data will not be presented in subsequent microthermometry graphs. Type II inclusions are less abundant than Type I inclusions. Salinity of the fluid inclusions range from 0.53 wt% eNaCl to 19.05 wt% eNaCl ($\bar{x}$ = 7.04 wt% eNaCl, σ = 4.70), forming two clusters for low salinity and medium salinity (Fig. 4.17b) while the density of the inclusions ranges from 0.792 $g.cm^{-3}$ to 1.060 g/cm^3 ($\bar{x}$ = 0.948 g/cm^3, σ = 0.048).

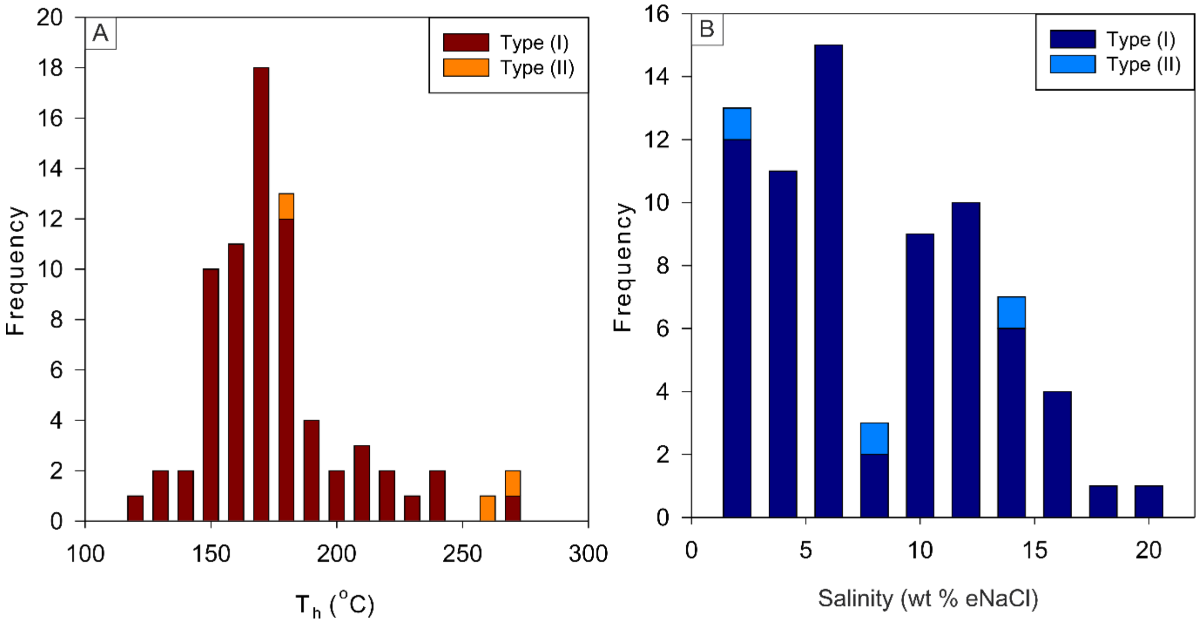

Figure 4.17: Histograms of the frequency of (A) homogenisation temperatures (T_h in °C) and (B) salinity (in wt% eNaCl). There is a large range in homogenisation temperatures averaging at 172 °C and there is a large range in salinity of the inclusions averaging at 7.04 wt% eNaCl. Results show no compositional differences in homogenisation temperature between type I and type II inclusions and there are two clusters of salinity, low and medium salinity.

4.4.3 Chemical characterisation of the fluids using Raman spectroscopy

Raman spectroscopy data were obtained at a room temperature of 25 °C. Interpretation of Raman spectroscopy analysis was obtained from data provided by Frezzotti et al. (2012). The monophase fluids have a composition dominated by liquid CO_2 and are irregular shaped with sharp points (Fig. 4.16d). The low final melting temperature of these fluids (-56.2 to -22.6 °C) indicates the presence of other volatile species such as CH_4 and H_2S (Frimmel at al., 1993). Type I and Type II fluid inclusions that have a liquid-phase made up of H_2O and a vapour-phase made up of H_2O make up 90% of the inclusion's composition (Fig. 4.18). These fluid inclusions are generally irregularly shaped (Fig. 4.18a and 4.18b insert). Raman spectra show

H_2O bands at 3424 cm^{-1} to 3428 cm^{-1} for the vapour-phase and at 3412 cm^{-1} to 3419 cm^{-1} for the liquid-phase.

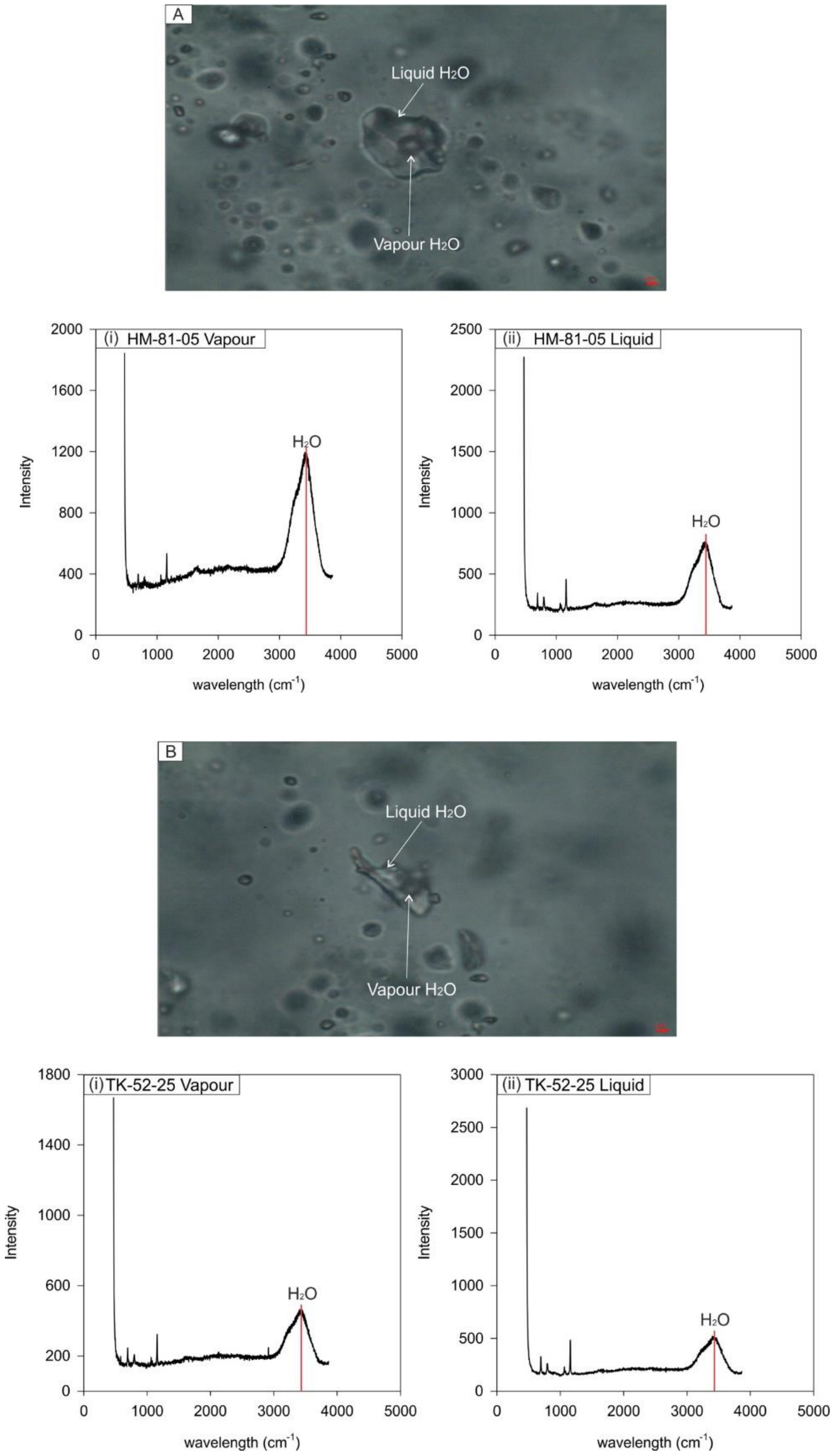

Figure 4.18: Raman spectra for common fluid inclusions dominated by a H_2O-rich vapour-phase and H_2O-rich liquid-phase. (A) Sub-rounded liquid-phase fluid inclusion enclosing a well-rounded vapour-phase. (B) Irregular-shaped liquid-phase fluid inclusion enclosing a rounded vapour-phase. Images (i) indicate peaks for the vapour phase and images (ii) indicate peaks for the liquid phase. The red scale bar represents 2 µm.

Type I inclusions with a solid carbon inclusion in a H_2O liquid, and very rarely, in a carbon-rich liquid make up 8 % of the inclusions (Fig. 4.19a and 4.19b inserts, respectively). These inclusions have a generally rounded solid carbon-rich inclusion surrounded by a generally sub-rounded H_2O-rich or carbon-rich liquid-phase. The solid carbons are opaque while the hydrocarbon liquid is transparent but darker than the liquid H_2O. In these inclusions, Raman peaks (Fig. 4.19) were observed at 3267 cm^{-1} for liquid H_2O and at 1351 – 1581 cm^{-1}, representing the graphitic solid carbon double bands (Frezzotti et al., 2012), 2707 cm^{-1} for a very strong carbon band and two peaks for CH_4 from 2914 – 3248 cm^{-1}. Liquid hydrocarbon showed carbon peaks at 1353 – 1584 cm^{-1}, a very strong carbon peak at 2705 cm^{-1} and a weak CH_4 peak at 2947 cm^{-1}.

One sample revealed an interesting composition in its vapour phase. This is a Type IV inclusion with a circular vapour phase (Fig. 4.20) consisting of a mixture of CO_2 (Raman peak at 1353 cm^{-1}), H_2O (Raman peak at 1670 cm^{-1}), H_2S (Raman peak at 1364 cm^{-1}) and CH_4 (doublet Raman peaks at 2944 – 3246 cm^{-1}). The presence of CO_2 vapour indicates that it is a Type IV 3 phase inclusion, however, the liquid CO_2 may not be visible because it may be small in volume and thus hidden by the large vapour. The Raman peak for CO_2 liquid may also be difficult to observe because it may overlap with other hydrocarbons (such as CH_4) as they are sensitive to pressure and temperature. The liquid phase has a H_2O Raman peak at 3270 cm^{-1}. The liquid phase is also generally rounded and 3 μm in diameter.

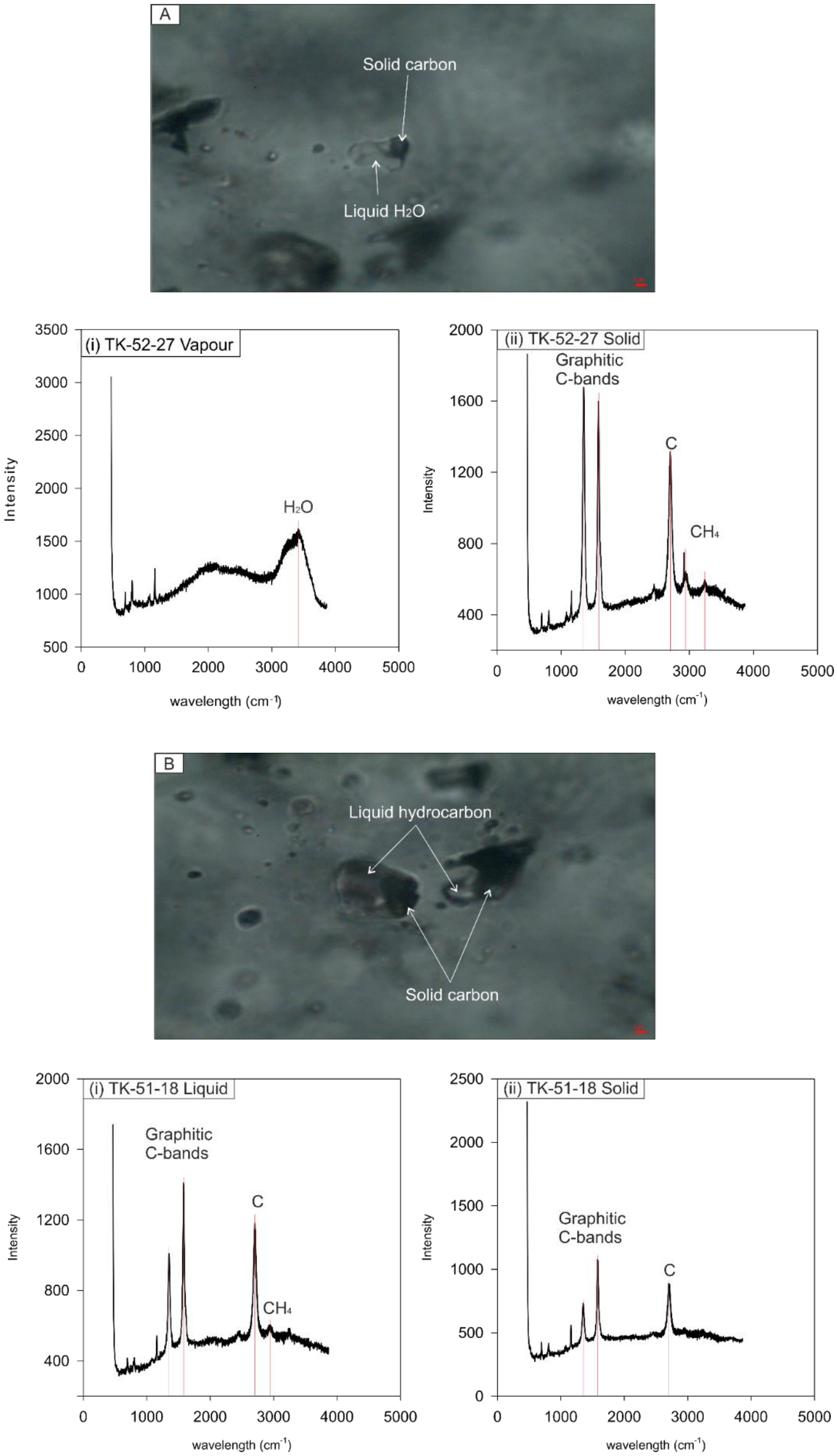

Figure 4.19: Raman spectra for fluid inclusions dominated by an inner solid carbon and (A) a (i) H_2O-rich liquid-phase and (B) a (i) carbon-rich liquid-phase phase. The liquid phase of these fluid inclusions of this composition have a generally sub-rounded shape and Raman peaks are observed at ~3270 cm^{-1} for H_2O, 1350 – 1590 cm^{-1} for solid graphitic carbon and 2910 – 3250 cm^{-1} for CH_4. The red scale bar represents 2 µm.

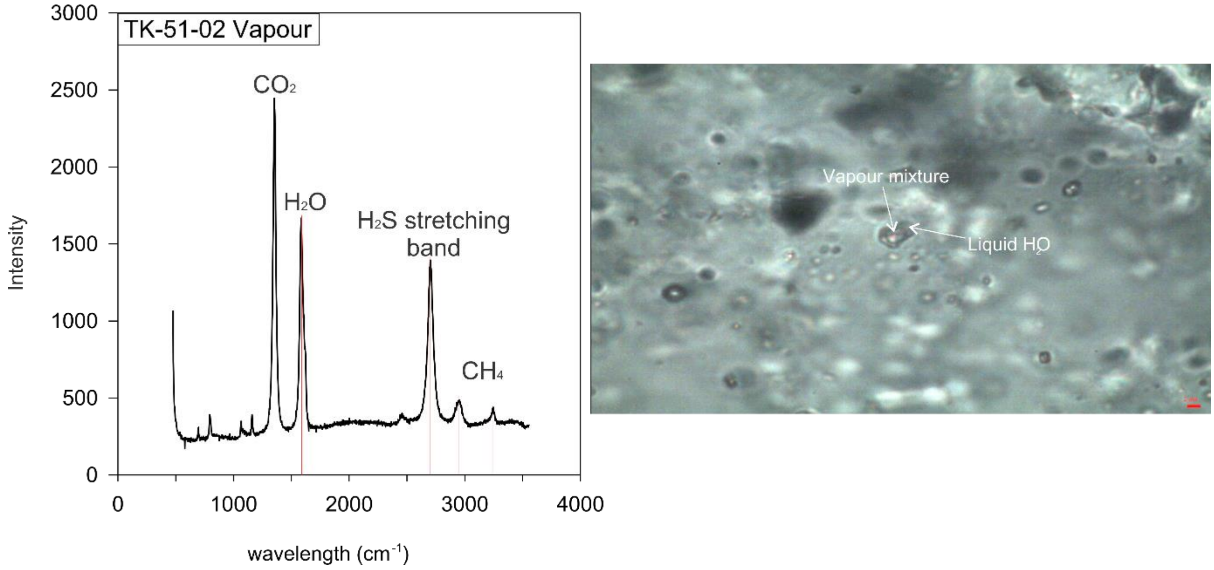

Figure 4.20: Raman spectrum of a type II fluid inclusion with a H_2O liquid phase and a vapour phase dominated by a mixture of CO_2, H_2O, H_2S and CH_4. Scale bar is 2 µm in the inclusion image.

4.5 Geochemistry

4.5.1 XRD mineral quantification

X-ray diffraction was carried out on samples to quantify the mineral assemblages for each lithology and to specifically quantify matrix minerals that are too fine-grained for traditional microscopic identification. The corresponding X-Ray Diffraction (XRD) spectra are attached in Appendix D. The results (Fig. 4.21) show that carbonaceous shale samples ($n = 3$) have the least quartz content ($\bar{x} = 56.1$ %), but the highest muscovite and chlorite abundances ($\bar{x} = 37.4$ % and $\bar{x} = 6.0$ % respectively) with no pyrophyllite. Quartz arenite samples ($n = 7$) have the highest quartz content ($\bar{x} = 95.1$ %), lowest muscovite abundances ($\bar{x} = 2.4$ %), low pyrophyllite contents ($\bar{x} = 1.9$ %) and no chlorite. Conglomerate samples ($n = 19$) have 87.3 % quartz and the clay minerals make up 10.4 % (muscovite: $\bar{x} = 5.7$ %; pyrophyllite: $\bar{x} = 4.6$ %; chlorite: $\bar{x} = 0.1$ %). Pyrite mineralisation is concentrated in the conglomerate samples ($\bar{x} = 2.3$ %) and is lower in the carbonaceous shale and quartz arenite samples ($\bar{x} = 0.5$ % for both rock types).

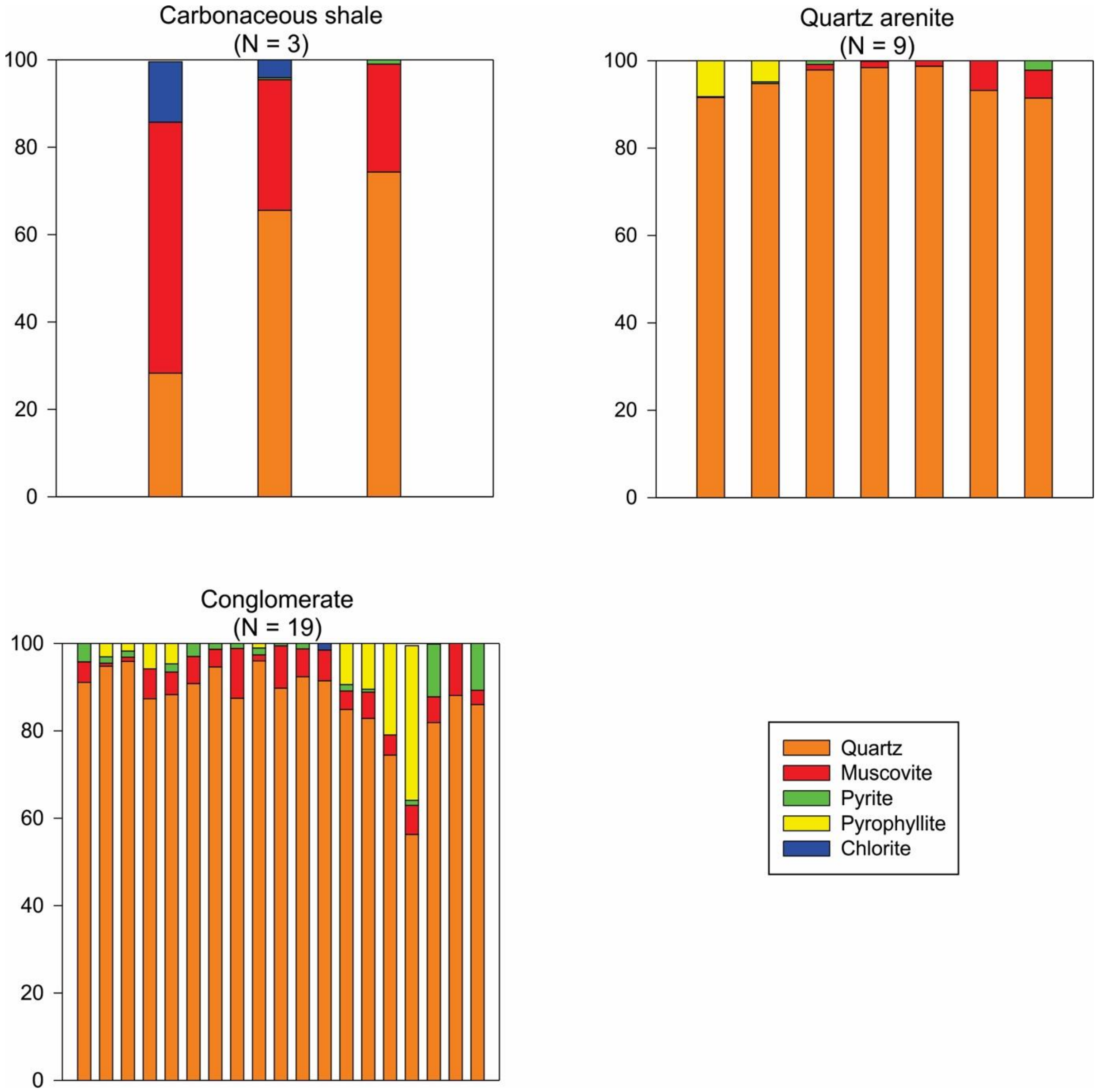

Figure 4.21: Cumulative bar graph indicating different minerals analysed by XRD in the Black Reef Formation samples. The main minerals analysed were quartz, muscovite, pyrite, pyrophyllite and chlorite. Shale samples gave the highest content of muscovite and chlorite while quartz arenite has the highest quartz content with fewer clay minerals present. Conglomerate samples have erratic amounts of quartz, but higher clay mineral proportions in the matrix than quartz arenites and the highest pyrite mineralisation.

4.5.2 Major element chemistry

Understanding processes that influence the weathering, transport and sorting of sediments, may provide insight into the provenance of the Black Reef succession (Taylor and McLennan, 1985). Major elements record these aspects and the major element oxide data for Black Reef are tabulated in Appendix E1. The TiO_2 and Al_2O_3 contents of Black Reef carbonaceous shale have a comparable composition to that of the post-Archaean Australian shale (PAAS) reference

(Fig. 4.22; Taylor and McLennan, 1985). Carbonaceous shales have the lowest SiO_2 content (61.19 – 82.21 wt%; x̄ = 73.13 ± 6.56 wt%) and the highest Al_2O_3 (8.99 – 18.79 wt%; x̄ = 15.58 ± 3.61 wt%). Quartz arenites contain 90.22 to 94.83 wt% SiO_2 (x̄ = 92.63 ± 1.44 wt%) and Al_2O_3 ranging from 2.35 to 5.93 (x̄ = 3.76 ± 1.12 wt%). Conglomerate units of the Black Reef exhibit a relatively broad compositional range, with SiO_2 between 79.34 to 92.61 wt% (x̄ = 87.49 ± 3.11 wt%) and Al_2O_3 between 1.96 to 10.25 (x̄ = 5.62 ± 2.01 wt%). All Black Reef lithology are slightly depleted in Al_2O_3 and TiO_2 relative to PAAS and more depleted in CaO and MgO relative to PAAS (Fig. 4.22). The Black Reef carbonaceous shales have Fe_2O_3 contents that range from 0.56 to 6.97 wt% (x̄ = 2.38 ± 2.28 wt%). Black Reef quartzite have Fe_2O_3 content from 0.66 to 3.01 wt% (x̄ = 1.43 ± 0.76 wt%), whereas the conglomerate ranges from 0.63 to 8.78 wt%, with x̄ = 2.69 ± 1.80 wt%.

Black Reef carbonaceous shale contains 0.99 wt% total organic carbon (TOC), quartz arenite has 0.15 wt% TOC and the conglomerate has 0.21 wt% TOC. The total sulphur (TS) content of the Black Reef varies from 0.32 to 0.39 wt% (x̄ = 0.35 ± 0.03 wt%) in carbonaceous shale, from 0.14 to 1.73 wt% (x̄ = 0.43 ± 0.46 wt%) in quartz arenites, and from 0.10 to 4.38 wt% (x̄ = 1.55 ± 1.03 wt%) in conglomerate. Correlation factors are used to describe the linear relationship between elements in Figure 4.23. For TOC and TS (Fig. 4.23a), a weak positive correlation exists in carbonaceous shale and quartz arenites (r = +0.35 and +0.24, respectively), whereas a negative correlation (r = -0.40) is observed for conglomerate. For TS and Fe_2O_3 (Fig. 4.23b), the correlation in carbonaceous shale is negative (r = -0.34), a good positive correlation is observed in quartz arenite (r = +0.54) and a strong positive correlation is observed in conglomerate (r = +0.95). This indicates that the TS and Fe_2O_3 are mainly located in the pyrite. For TOC and Al_2O_3 (Fig. 4.23c), the correlation in carbonaceous shale is good (r = +0.71), with no correlation evident for quartz arenite (r = -0.18) and positive correlation in conglomerate (r = +0.35). Except for quartz arenite which has a positive correlation between TOC and SiO_2 (r = +0.32), there are negative correlations between TOC and SiO_2 and between TS and SiO_2 in all Black Reef lithologies (Fig. 4.23d – filled symbols refer to TS vs SiO_2).

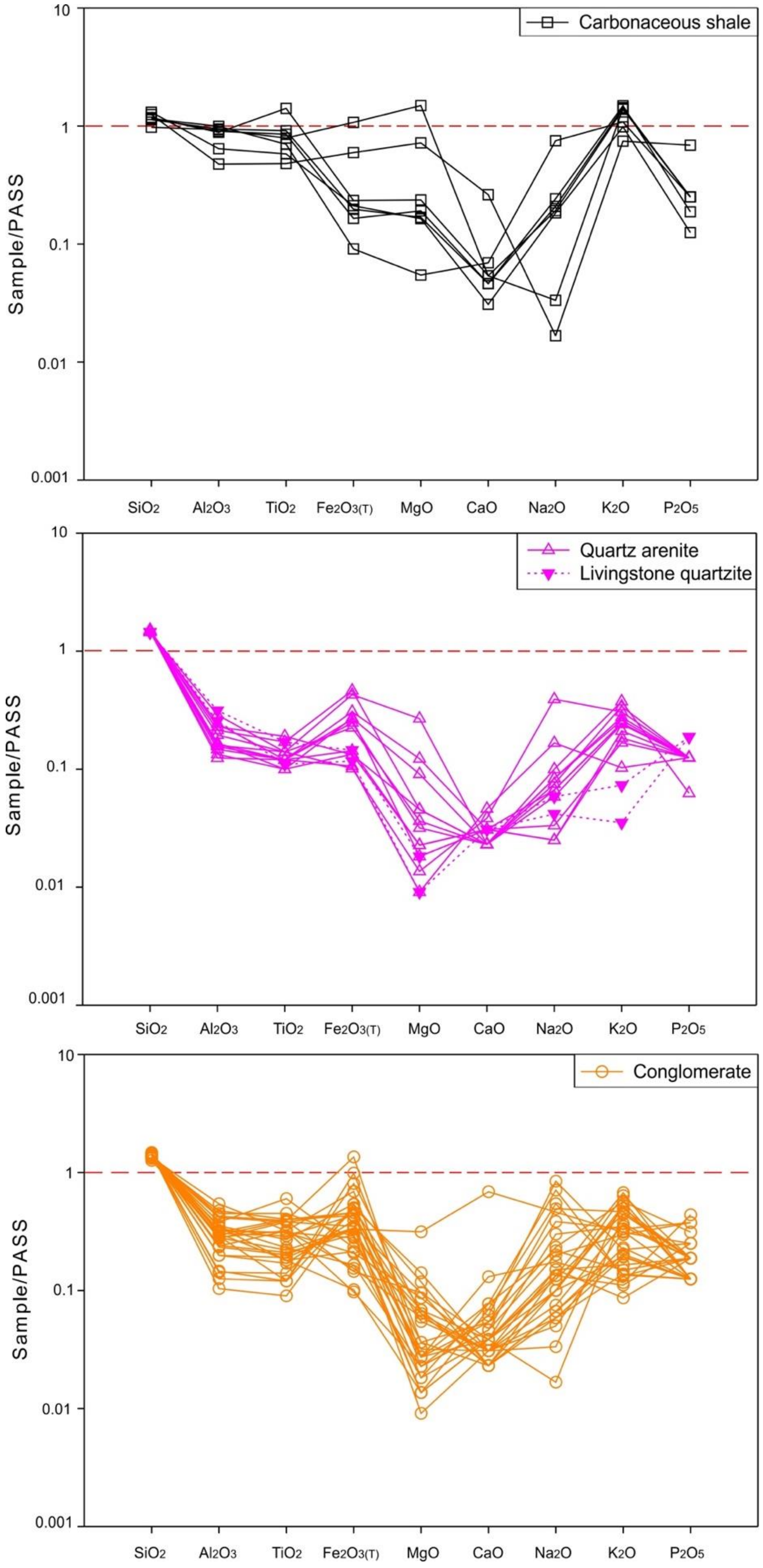

Figure 4.22: Major element composition of shale, quartz arenite and conglomerate of the Black Reef samples normalised relative to PAAS. All samples are depleted in MgO and CaO relative to PAAS, while quartz arenites are slightly depleted in Al_2O_3 and TiO_2 relative to PAAS. The dashed line indicates values where the sample concentration values are equal to PAAS reference values.

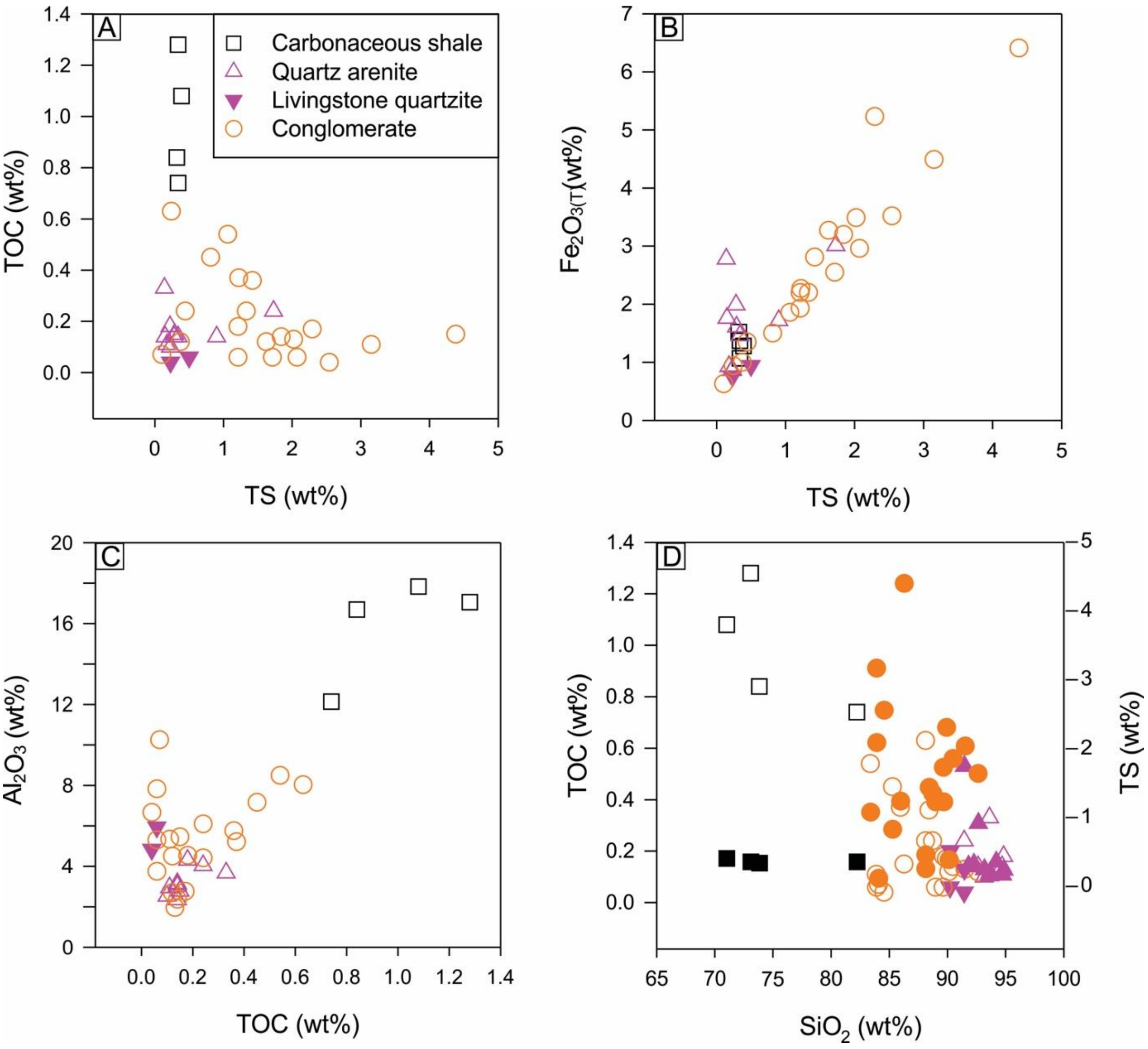

Figure 4.23: Correlation diagrams between (A) TOC vs TS, (B) $Fe_2O_{3(T)}$ vs TS, (C) Al_2O_3 vs TOC, and (D) TOC and TS vs SiO_2 for all Black Reef lithology. Carbonaceous shale shows positive correlations between TOC and TS and between Al_2O_3 and TOC. Quartz arenite shows positive correlations between TOC and TS, between $Fe_2O_{3(T)}$ and TS, and between TOC and SiO_2. Conglomerate shows positive correlations between TS and $Fe_2O_{3(T)}$, between Al_2O_3 and TOC. Filled symbols in (D) correspond to TS vs SiO_2 while unfilled symbol represents TOC vs SiO_2.

4.5.3 Trace element chemistry

Relatively immobile trace elements are considered as indicators of source-rock composition (Taylor and McLennan, 1985). The trace element data are represented in Appendix E2. The post-Archaean Australian shale was used to normalise the elemental contents because it contains a complete set of trace elements when compared to Archean shale. The average trace element values of the Black Reef lithology compared to the PAAS reference shows that the carbonaceous shale, quartz arenite and conglomerate are relatively depleted in large ion lithophile elements (LILEs) (Fig. 4.24), such as Rb, Ba, Sr and Cs. The high-field-strength elements (HFSEs), such as Nb, Hf, Th and U, show an increase in enrichment relative to PAAS from Nb to U. The transition metals (TMs), such as Co, Cr and Ni, are slightly depleted for carbonaceous shale, but are enriched for quartz arenite and conglomerate. Carbonaceous shale associated with the Black Reef show a positive correlation between TOC and trace elements except for Ni, Co and Cu. Total sulphur has a strong positive correlation with Mo (r = +0.87) and Pb (r = +0.93) for all Black Reef lithology. In conglomerate units, TOC correlates negatively with Pb, Co, Cu and Ni but these elements correlate positively with TS.

The PAAS-normalised rare earth element (REE) patterns for all Black Reef lithologies are shown in Figure 4.25. The Black Reef patterns are relatively similar to those in PAAS (Condie, 1993). The Black Reef carbonaceous shales have an average higher total REE content than the quartz arenite and conglomerate. Generally, the REE patterns are characterised by (Table 4.1):

1) small light-REE (LREE) / heavy-REE (HREE) fraction (La_N/Yb_N),
2) flattish HREE (Gd_N/Yb_N) pattern, and
3) small amplitude of Eu anomalies (Eu/Eu*).

The one anomalous carbonaceous shale sample relates to the shale the with the highest CaO content (0.34 wt%) and second highest MgO content (1.58 wt%), attributed to a dolomitic shale.

Table 4.1: Summary of PAAS-normalised rare earth elements (REE) patterns for all Black Reef lithologies.

REE Pattern	Carbonaceous Shale	Quartzite	Conglomerate
$\bar{x}\Sigma_{REE}$	125.35	56.44	112.50
La_N/Yb_N	0.90 - 1.99	1.19 - 2.53	0.43 - 4.31
Gd_N/Yb_N	1.01 - 1.97	1.01 - 2.22	0.77 - 2.60
Eu/Eu*	1.00 - 1.17	0.83 - 1.43	0.70 - 1.64

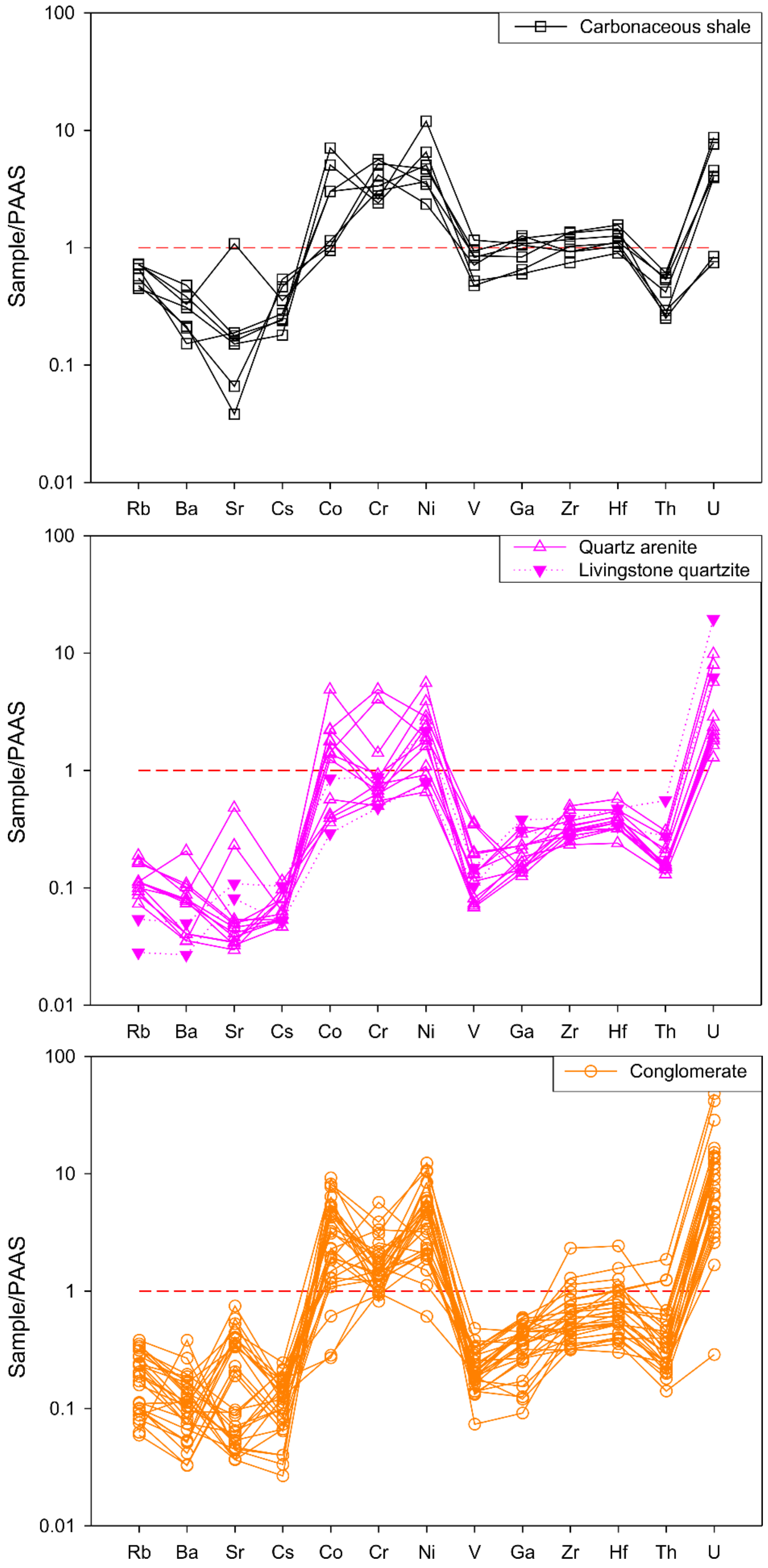

Figure 4.24: Spider diagrams of trace element patterns for shale, quartz arenite and conglomerate of Black Reef samples, normalized relative to PAAS. There is a general depletion in LILEs, and enrichment in TMs and an increasing enrichment in HFSEs. The dashed line indicates values where the sample concentration values are equal to PAAS reference values.

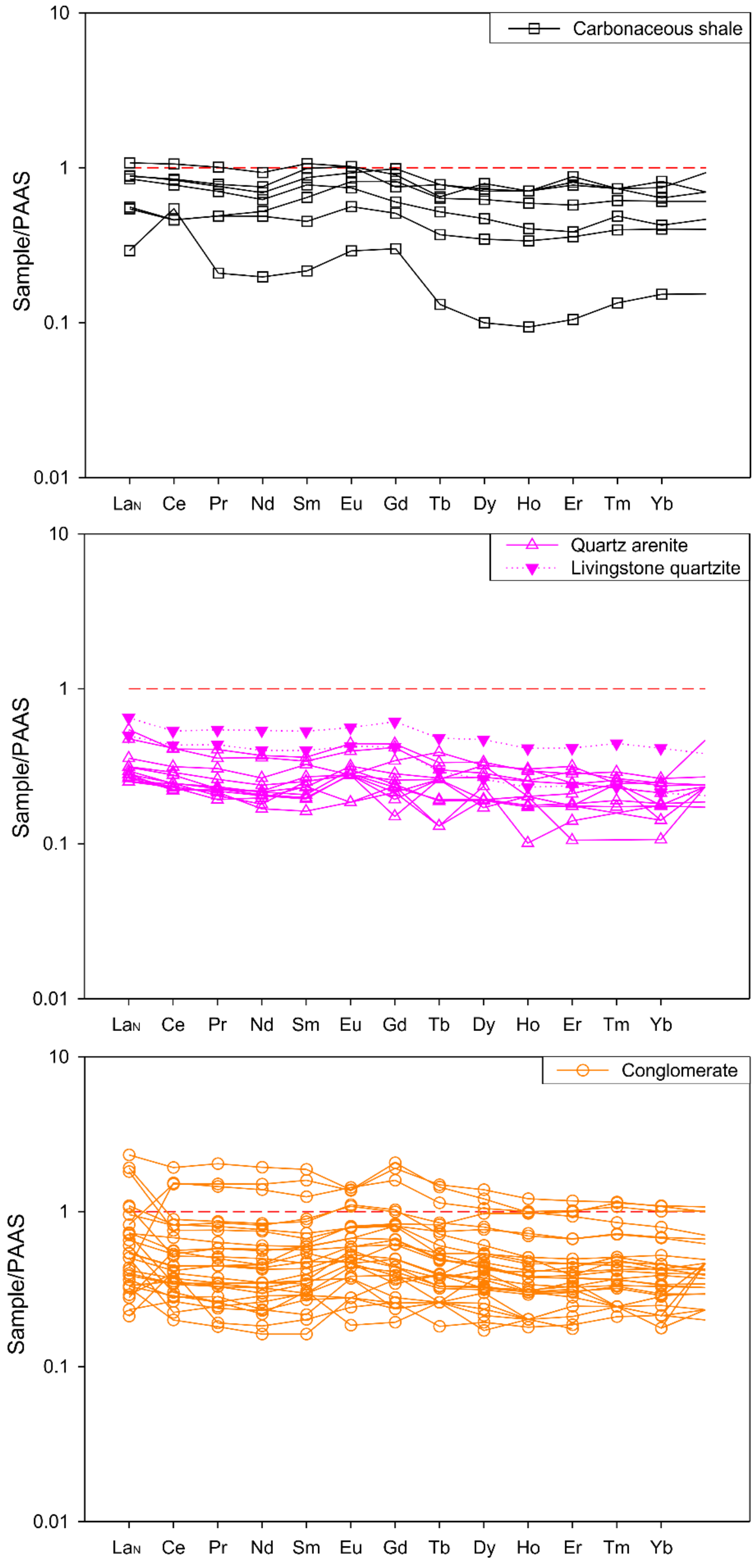

Figure 4.25: REE patterns of Black Reef shales, quartz arenites and conglomerates that are PAAS normalized. Shales have a relatively horizontal pattern. Quartz arenite and conglomerate have a slight HREE depletion pattern. All the samples are depleted in REEs relative to PAAS. The dashed line indicates values where the sample concentration values are equal to PAAS reference values.

4.5.4 Correlation of gold with major and trace elements

Figure 4.26 shows the correlation of Au with SiO_2, total organic carbon (TOC), total sulphu (TS), U, Zr and Zr/Ni in Black Reef carbonaceous shale, quartz arenite and conglomerate. Gold and SiO_2 (Fig. 4.26a) have no correlation for carbonaceous shale (r = -0.19), correlation is negative for quartz arenite (r = -0.53) and is positive for conglomerate (r = +0.50). TOC and TS are negatively correlated with Au in carbonaceous shale (r = -0.40 and -0.56, respectively). Gold has a weak positive correlation with TOC (r = +0.24) and a strong positive correlation with TS (r = +0.82) in quartz arenite samples. Gold has a negative correlation with TOC (r = -0.32) and a positive correlation with TS (r = +0.46) in quartz arenite samples. (Fig. 4.26b, 4.26c). There is a negative correlation between Au and U for carbonaceous shale (r = -0.63) and a positive correlation for both quartz arenite and conglomerate (r = +0.53 and +0.35, respectively) (Fig. 4.26d). Carbonaceous shale and quartz arenite show positive correlations for Zr and Au (r = +0.36 and +0.53, respectively) while conglomerate show a negative correlation (r = -0.17; Fig.4.26e). A negative correlation between Au and Zr/Ni is observed in all Black Reef samples (carbonaceous shale: r = -0.43; quartz arenite: r = -0.43; conglomerate: r = -0.34; Fig. 4.26f).

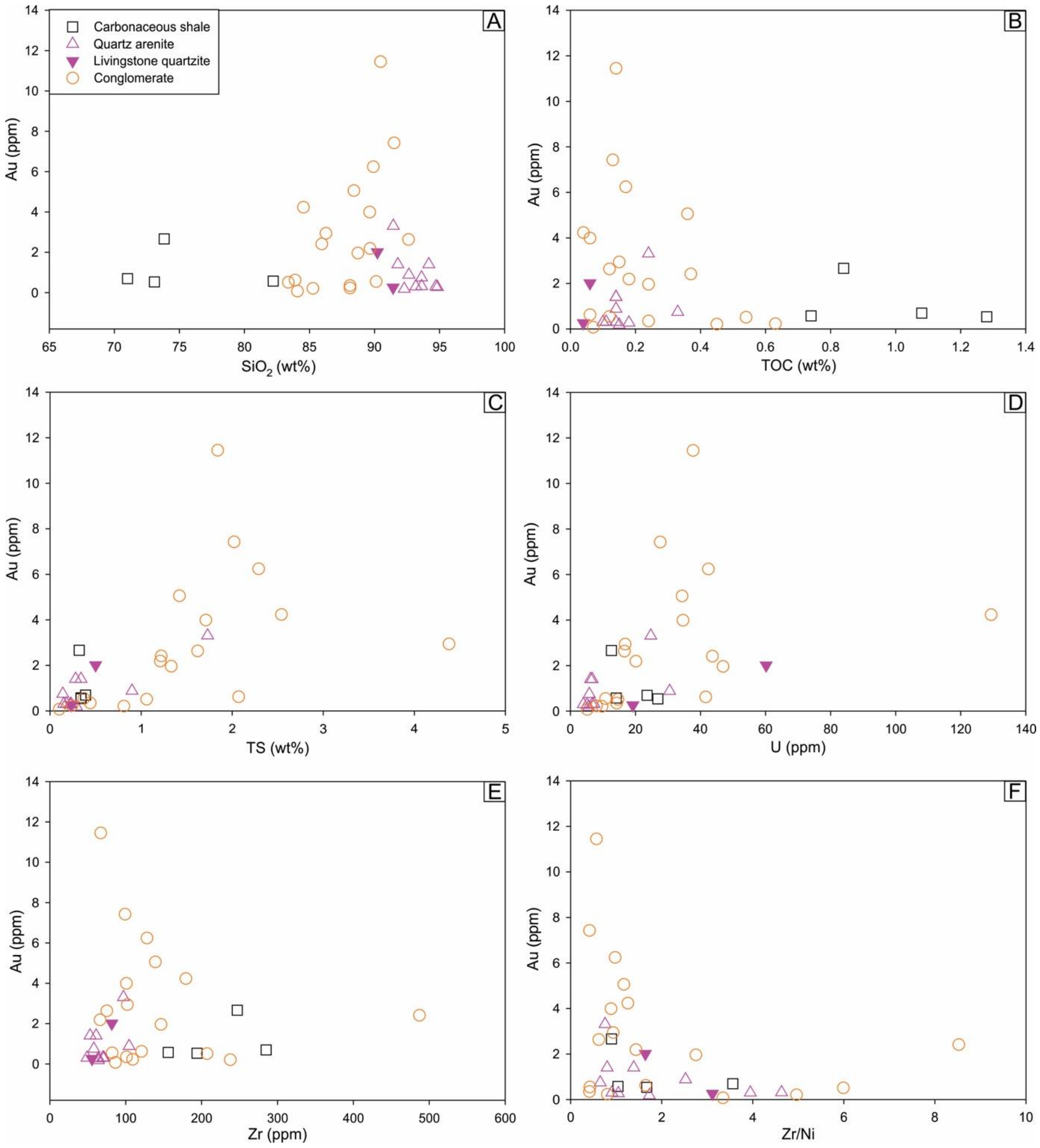

Figure 4.26: Binary diagrams of Au vs SiO$_2$, TOC, TS, U, Zr and Zr/Ni. Gold in conglomerate correlates positively with SiO$_2$, TS and U and negatively with TOC, Zr and Zr/Ni. Gold in quartz arenite correlates positively with TOC, TS, U and Zr and negatively with SiO$_2$ and Zr/Ni. Gold in shale correlates positively with Zr, negatively with TOC, TS, U and Zr/Ni while there is no correlation with SiO$_2$.

4.5.5 Sulphur isotope composition of pyrite

Sulphur isotope results are presented in Appendix F. Pyrite separates from whole-rock samples of the Black Reef all show positive δ^{34}S values with respect to the CDT standard. Both the shale and conglomerate samples show low variation in δ^{34}S with values between 2.70 and 3.70

‰ in shales (x̄ = 3.20 ± 0.71 ‰) and 2.80 and 3.50 ‰ in conglomerates (x̄ = 3.13 ± 0.22 ‰) and this shows that they are similar in S-isotope space. Figure 4.27 indicates that Black Reef sulphides in this study plot at δ^{34}S values overlapping with previous studies by Hofmann et al. (2009) and Guy et al. (2014). The mean δ^{34}S value for this study coincides within the mean and 75th percentile in the study by Guy et al. (2014), specifically for samples obtained from the Carletonville and Klerksdorp goldfields. The mean δ^{34}S value for this study also coincides with values above the 75th percentile in the study by Hoffmann et al. (2009), specifically in samples obtained from the VCR TauTona Mine and Randfontein Kimberley Reef in the Carletonville goldfield and the Dominion Reefs Uranium Mine in the Klerksdorp goldfield.

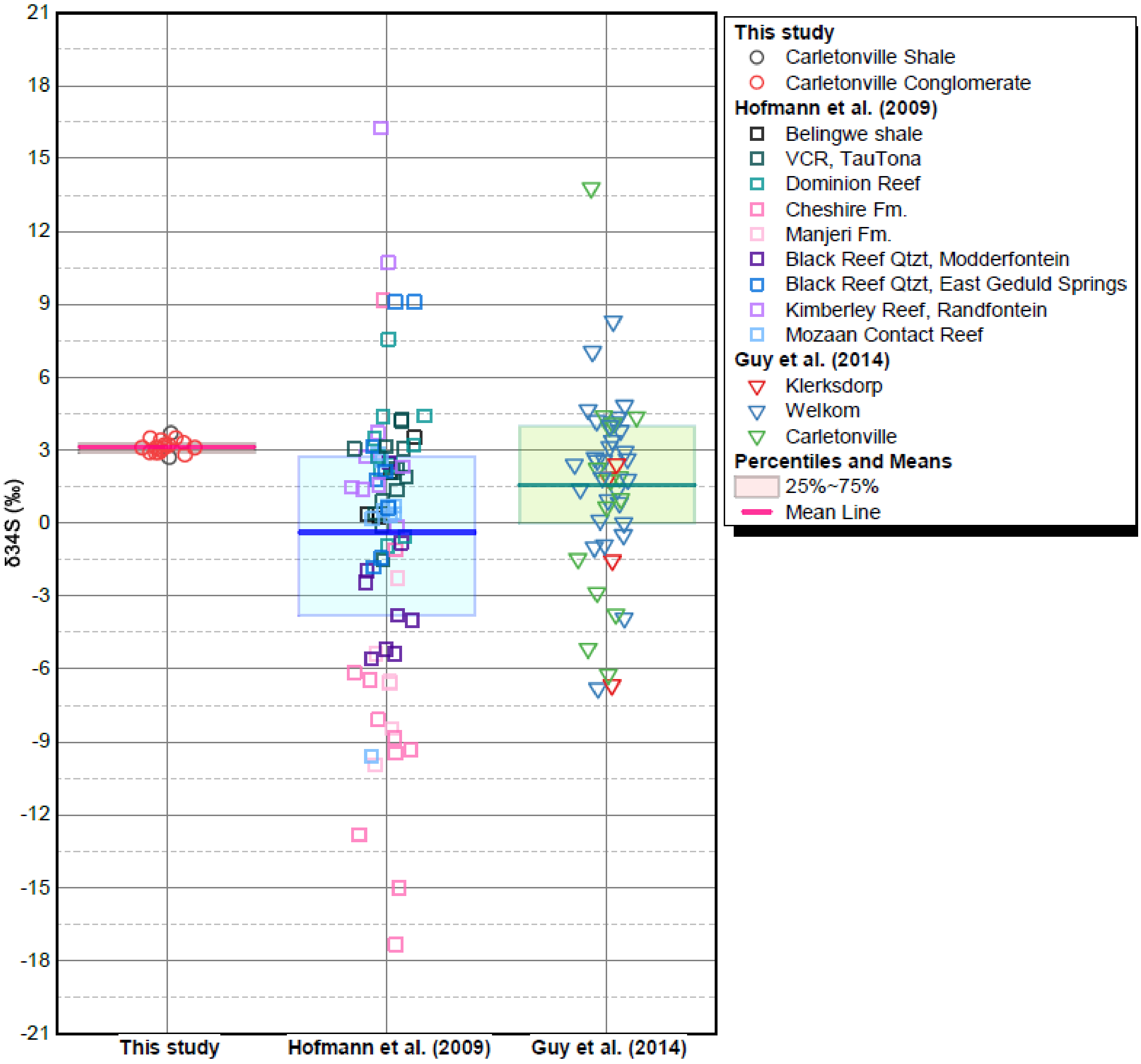

Figure 4.27: Stable δ^{34}S isotope data for whole-rock samples from the Black Reef (this study) compared to those from Hofmann et al. (2009) and Guy et al. (2014). This study shows a low range in δ^{34}S values, with the mean δ^{34}S (3.20 ‰ and 3.13 ‰) values coinciding with samples collected from the Carletonville Goldfields (VCR and Randfontein Kimberley Reef) and in the Klerksdorp goldfield (Dominion Reef).

4.6 Summarised major findings

The main outcomes of the results are listed below in table 4.1.

Table 4.2: Summary of the ore mineral and fluid inclusion parameters (Qtz = quartz, Py = pyrite, Sph = sphalerite, Flinc = fluid inclusion).

Mineral	Morphology	Grain size	Origin	Texture / Mode of occurrence	Mineral Association
Gold	Irregular	10 - 250 µm	Hydrothermal	Massive	Py, Qtz pebble fractures
DM Py	Irregular, abraded cubic	50 - 350 µm	Detrital / Allogenic	Massive	Py, pyrobitumen, Qtz pebbles
DIR Py	Rounded, irregular	50 - 2000 µm	Detrital Allogenic	Porous	Py, pyrobitumen, Qtz pebbles
DIC Py	Concentrically laminated	500 - 1000 µm	Detrital Allogenic	Porous, concretionary	Py, pyrobitumen
AE Py	Euhedral / subhedral cubic	100 - 1000 µm	Authigenic	Massive, occasionally porous	Py, pyrobitumen, Qtz pebbles
AO Py	Irregular	10 - 200 µm / surrounds pyrite grains	Authigenic / Diagenetic	Massive	Py, pyrobitumen
Globular pyrobitumen	Sub-rounded, complex shaped	500 - 1500 µm	Hydrothermal	Inclusion-rich	Qtz cracks and boundaries
Fracture-filling pyrobitumen	Irregular	Can cover entire thin section or be interstitial	Hydrothermal	Massive / Cryptocrystalline	Py, Sph, Qtz boundaries, Qtz fractures
Nodular pyrobitumen	Rounded	200 - 500 µm	Hydrothermal	Massive, inclusion-poor	Qtz cracks and boundaries
Irregular pyrobitumen	Sub-rounded, complex shaped	200 - 500 µm	Hydrothermal	Inclusion-rich	Surrounded by Py
Type I Flinc	Irregular to sub-rounded	3 - 10 µm	Hydrothermal	Two-phase	Qtz fractures, Py; aqueous, H_2O-CH4-Graphite-rich
Type II Flinc	Sub-rounded, elongated	2 - 6 µm	Hydrothermal	Two-phase	Qtz fractures, Py; H_2O-CO_2 rich
Type III Flinc	Irregular	3 - 7 µm	Hydrothermal	Monophase	Qtz fractures, Py; CO_2-rich
Type IV FLINC	Irregular	2 – 5 µm	Hydrothermal	Three-phase Difficult to observe 3rd phase	Qtz fractures, H_2O-CH_4-CO_2-H_2S-rich

Table 4.3: Summary of whole-rock $\delta^{34}S$ isotopes for carbonaceous shale and conglomerate in this study.

Rock type	Isotope type	Material type	Range (‰)
Carbonaceous shale	$\delta^{34}S$	Whole-rock	2.7 – 3.7
Conglomerate	$\delta^{34}S$	Whole-rock	2.8 – 3.8

Chapter 5: Discussions

The formation of the Black Reef is similar to that of the Witwatersrand reefs, as do other quartz-pebble conglomerate deposits. The investigation of the Black Reef with respect to integrated petrographic, geochemical and S-isotope provides insights that have not been explored before and offers alternative processes to best describe mechanisms for its gold mineralisation. The main aim of this study was to find evidence for the conglomerate-hosted gold mineralisation processes in the Black Reef. This section will discuss fundamental questions such as

- where are the sediments and ore minerals (gold, pyrite and carbon nodules) in the Black Reef sourced from;
- how are the ore minerals associated with the clastic sediments;
- what is the composition of the gold-mineralising fluids and their complexing ligands and what were the main fluid pathways;
- what is the deposition process and responsible preservation mechanism; and
- what were the palaeoenvironmental conditions in the Black Reef at the time of gold deposition.

5.1 Sediment and gold provenance

The Al/Ti/Zr ratios of sediments resemble those of their source rocks because these elements are immobile due to their low solubility as oxides and hydroxides in low-temperature aqueous solutions (Stumm and Morgan, 1981; Ziemniak et al., 1993). The Al_2O_3/TiO_2 ratio for Archean shale is 28; Archean granite is 59, Archean tonalite-trondhjemite-granodiorite is 51, Archean basalt is 15, and Archean komatiite is 23 (Condie, 1993). The conglomerate and quartz arenite units in this study have Al_2O_3/ TiO_2 ratios of 11.93 – 45.42 and 29.58 – 43.91 respectively, indicating a felsic proto-source from weathering and sorting of coarse sediments, while the shale units in this study have an Al_2O_3/ TiO_2 ratio of 11.84 – 26.84 indicating a mafic to intermediate proto- source from weathering and sorting of fine sediments (Fig. 5.1a). The whole-rock composition of the quartz arenite and conglomerate in this study does not fully display typical characteristics of shale, sandstone, arkose and arenite due to the presence of interlayers such as organic matter, clays and carbonates from calcite veins (Fig. 5.1b), but may rather reflect a reworked sediment source. Carbonaceous shales of the Black Reef have relatively high Cr (264 – 618 ppm) and moderate Zr (156 – 285 ppm) contents compared to the quartz arenite and conglomerate. The elevated Cr contents suggests a sediment source from mafic rocks such as the volcanic rock of the Ventersdorp Supergroup and the numerous greenstone belts of the Kaapvaal (Fig. 5.1c). The quartz arenite and conglomerate have Cr contents of 52.9 – 538 ppm and 90.0 – 627.9 ppm, respectively, and Zr contents of 49.0 – 104 ppm and 66.2 – 487 ppm, respectively. Figure 5.1c shows that the quartz arenite and conglomerate samples from the Black Reef plot near Archaean granites, Archaean TTGs, Archaean andesite and the PAAS reference values. This indicates that various Archaean felsic rocks of the Kaapvaal in the hinterland are the proto-source rocks for the quartz arenite and conglomerate sediments of the Black Reef.

Figures 5.1d and 5.1e shows a plot of Ni/Co versus magnesium number (X_{Mg}) and Gd_N/Yb_N ratio versus La_N/Yb_N ratio, which indicates different source-rock compositional content of Black Reef rocks. These plots are supported by a plot of Cr content versus Ni content (Fig. 5.1f) in the Black Reef samples. High Cr and Ni contents are related to ultramafic and mafic source-rocks, and these high concentrations are reflected in the carbonaceous shales. Low Cr and Ni content are related to intermediate to felsic source-rocks, supported by high Zr content, which is in the quartz arenites and conglomerates.

The samples obtained from the study by Simmons and McGloin (2020) from the Northern Territory Geological Survey (NTGS), Australia, were used as an indicator for a likely sulphur source and a graph comparing $\delta^{34}S$ from this study versus their study is shown in Figure 5.2. The sulphide samples from the Simmons and McGloin (2020) study are from orthomagmatic and epigenetic deposits, syngenetic volcanic, synsedimentary or carbonate replacement deposits, and volcanic- and sediment-hosted deposits. It is deduced that the $\delta^{34}S$ values of this study coincide mainly with those obtained in the Mount Doreen mapsheet, related to the ~1830 Ma Clark Cu deposit that is intrusion related breccia and vein epigenetic mineralisation. There are small correlations with the ~1770 Ma Oonagalabi Cu-Zn-Pb deposit (Strangways Range) of vein related carbonate replacement epigenetic mineralisation and the ~1780 Ma Jervoius mineral field (Illogwa Creek) with Broken Hill-type syngenetic with epigenetic overprint deposits. These are unlikely sulphur sources because they are young deposits which the sulphur fractionated under different atmospheric conditions than in the Archaean. The whole-rock $\delta^{34}S$ from this study shown in Figure 4.27 overlaps with values from pyrite grains of the VCR and Witwatersrand reefs. This indicate that the Black Reef pyrite sulphur signatures reflect a sulphur source similar to the underlying stratigraphy or that the Black Reef pyrite grains are recycled from the underlying stratigraphy. The latter is supported by preliminary Re-Os isotope ages by Nwaila et al. (2019), suggesting that Black Reef pyrite grains overlap with Re-Os isotope ages of pyrite grains from the VCR and Witwatersrand reefs. By inference, Black Reef gold would also have been mechanically sourced from the VCR and Witwatersrand reefs.

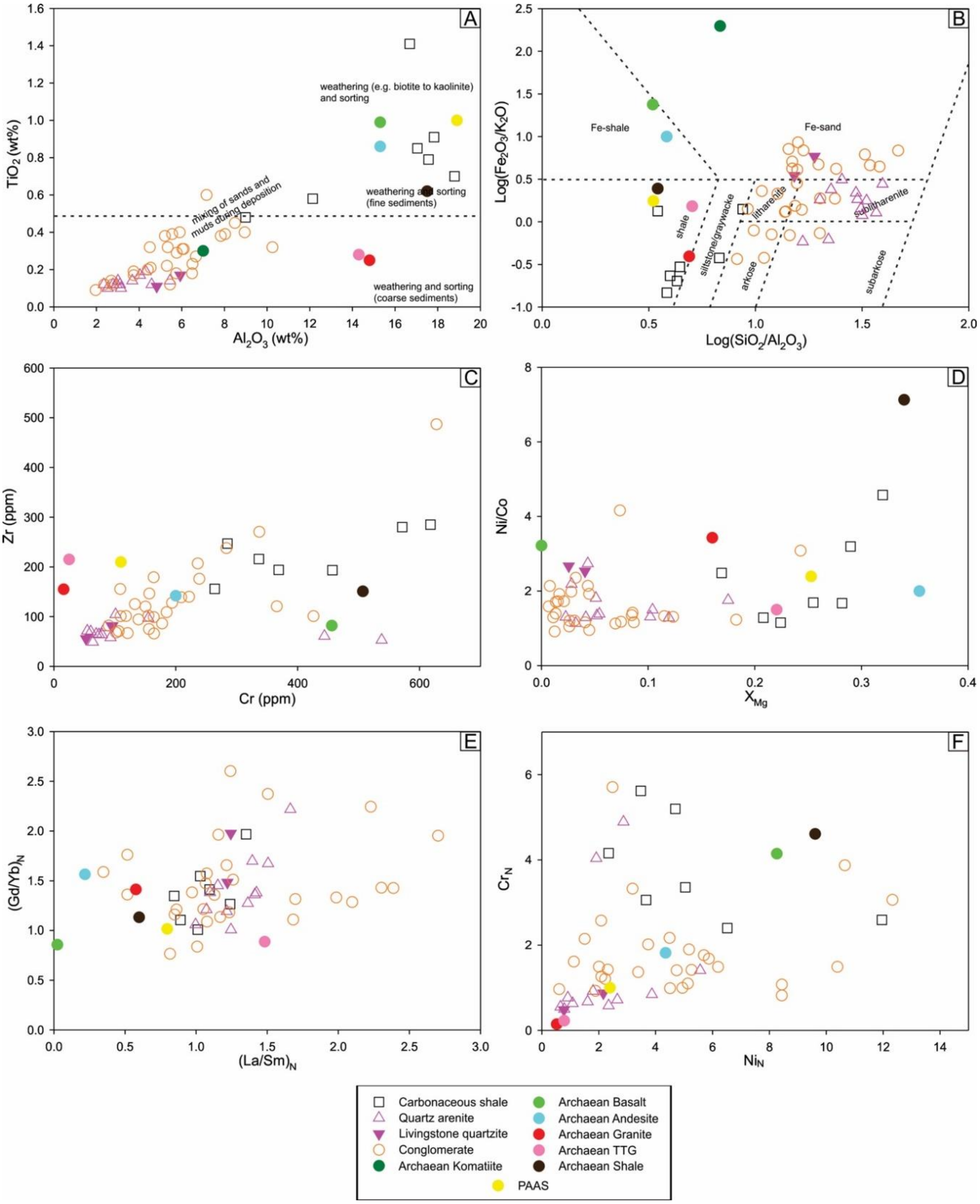

Figure 5.1: Sediment provenance characterisation. (A) Bivariate plot of TiO_2 (wt%) vs Al_2O_3 (wt%). (B) Logarithmic plot of Fe_2O_3/K_2O vs SiO_2/Al_2O_3. (C) Zr content vs Cr content. (D) Ni/Co vs X_{Mg}. (E) $(Gd/Yb)_N$ vs $(La/Sm)_N$. F) Cr content vs Ni content. Archaean rocks reference samples data is obtained from Condie (1993). PAAS = post-Archaean Australian shale; TTG = tonalite-trondhjemite-granodiorite.

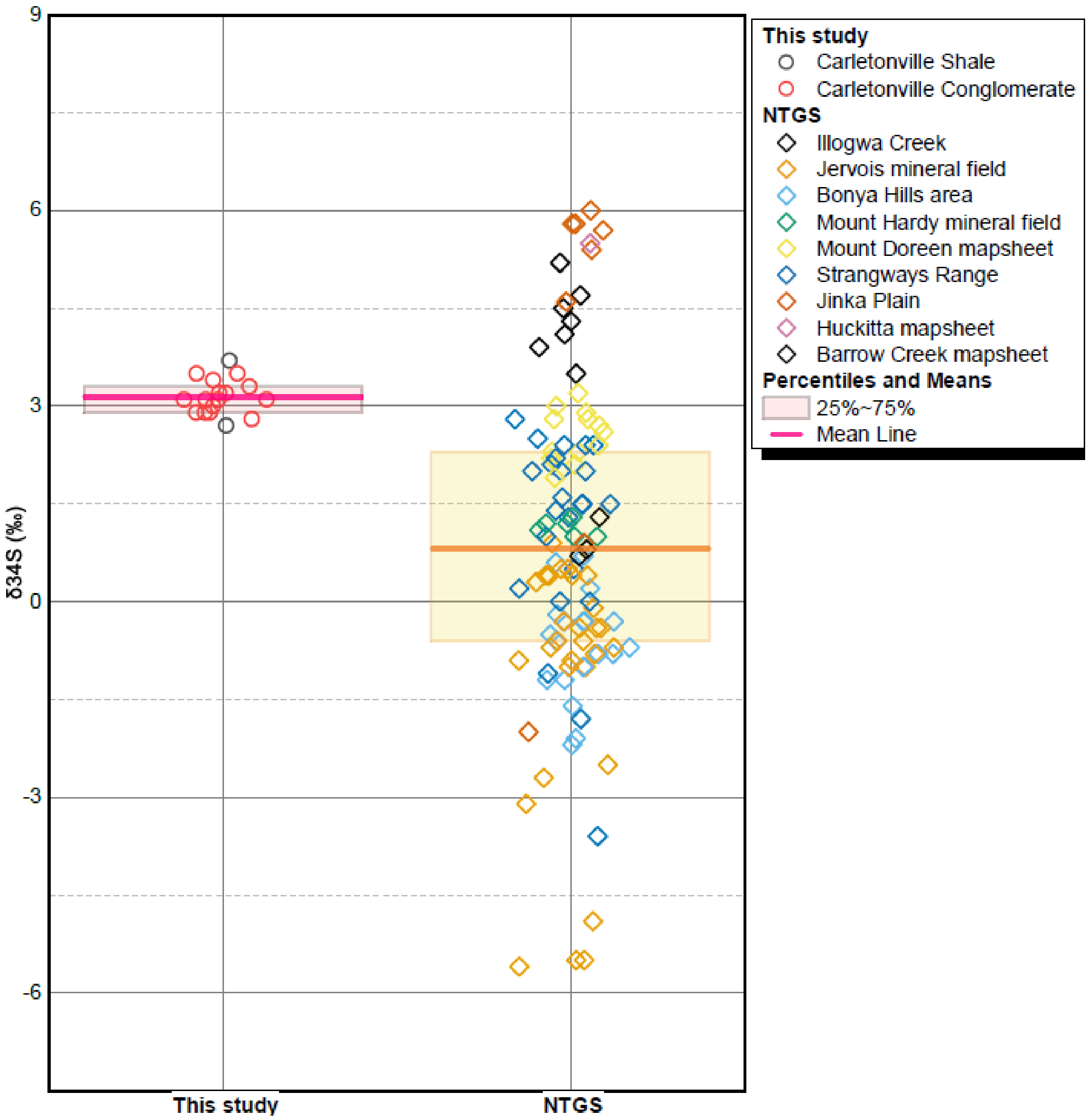

Figure 5.2: Stable δ^{34}S isotope data for whole-rock samples from the Black Reef (this study) compared to those from Northern Territory Geological Survey (NTGS) by Simmons and McGloin (2020).

5.1.1 Weathering and geochemical alteration

Weathering under an acidic Archean atmosphere was responsible for deep chemical weathering of the exposed Archaean surface in the Witwatersrand basin, marked by a high chemical index of alteration (CIA) (Sutton and Maynard, 1993; Frimmel, 2005; Frimmel and Hennigh, 2015). A CIA plot in Figure 5.3 was constructed to monitor how clay minerals progressed from alteration of plagioclase and potassium feldspar using molar proportions of Al_2O_3-(CaO + Na_2O)-K_2O (A-CN-K). The carbonaceous shale units have a low range in CIA with an average value of 76.0 ± 1.5 % similar to PAAS. In comparison, quartz arenite units show a relatively broader range with an average CIA of 79.1 ± 7.6 % and the conglomerate samples have an average CIA of at 78.9 ± 5.6 %. The carbonaceous shale units have the lowest CIA because they generally have lower permeability.

The two quartz arenite samples with CIA values above 90% represent those from the Livingstone Reef from the upper Central Rand Group. Intense acidic leaching by postdepositional fluids causes the loss of K in coarser grained siliciclastic rocks like quartzite and conglomerate (Barnicoat et al., 1997; Phillips and Powel, 2011). The hanging wall lithology are the most altered because large-scale alteration, marked by very high CIA values, is most intense in arenitic rocks immediately underlying the conglomerate-covered palaeoerosion surfaces, which gradually decreases with depth (Frimmel and Minter, 2002). The samples show a trend towards the kaolinite field where they are currently clustered at the muscovite field. This indicates that the dominant silicate in these samples is muscovite with a moderate to high rate of palaeoweathering in the source area. The high CIA values in this study suggest Al^{3+} remained during weathering while the more mobile cations (Ca^{2+}, Na^{+} and K^{+}) were removed. For carbonaceous shale samples, the amount of K-metasomatism is represented by the alteration of aluminous clay minerals such as kaolinite to illite through the addition of potassium.

Concentrations of CaO and Na_2O are very low in all of the studied Black Reef samples (average of 0.08 ± 0.13 wt% and 0.21 ± 0.23 wt%, respectively) also shown by the PAAS normalised major element plots (Fig. 4.22), indicating that plagioclase was weathered from its source region. No feldspar was recorded in the studied rocks for conglomerate and quartz arenite so CIA cannot be affected by K-metasomatism. Mole-for-mole replacement of K for Ca or Na is therefore suggested (Glazner, 1988) for quartz arenite and conglomerate with a (A-CNK-MF) diagram showing differences in clay mineral proportions. Carbonaceous shale samples still plot near the muscovite field while conglomerate and quartz arenite samples show grading from chlorite to kaolinite field (Fig. 5.3). The trend towards the kaolinite apex in the Black Reef samples is indicative of progressive alteration by removal of K, with the Livingstone quartzite samples being the most altered and having the least K_2O (see Fig. 4.22). This can be attributed to leaching of acid rain on old erosion surfaces followed by isochemical metamorphism of kaolinite-rich sediments (Wallmach and Meyer, 1990; Frimmel, 1994). The main fluid pathways are possibly following the arenite beds, and interstitial sand grain fraction controlling permeability in conglomerates.

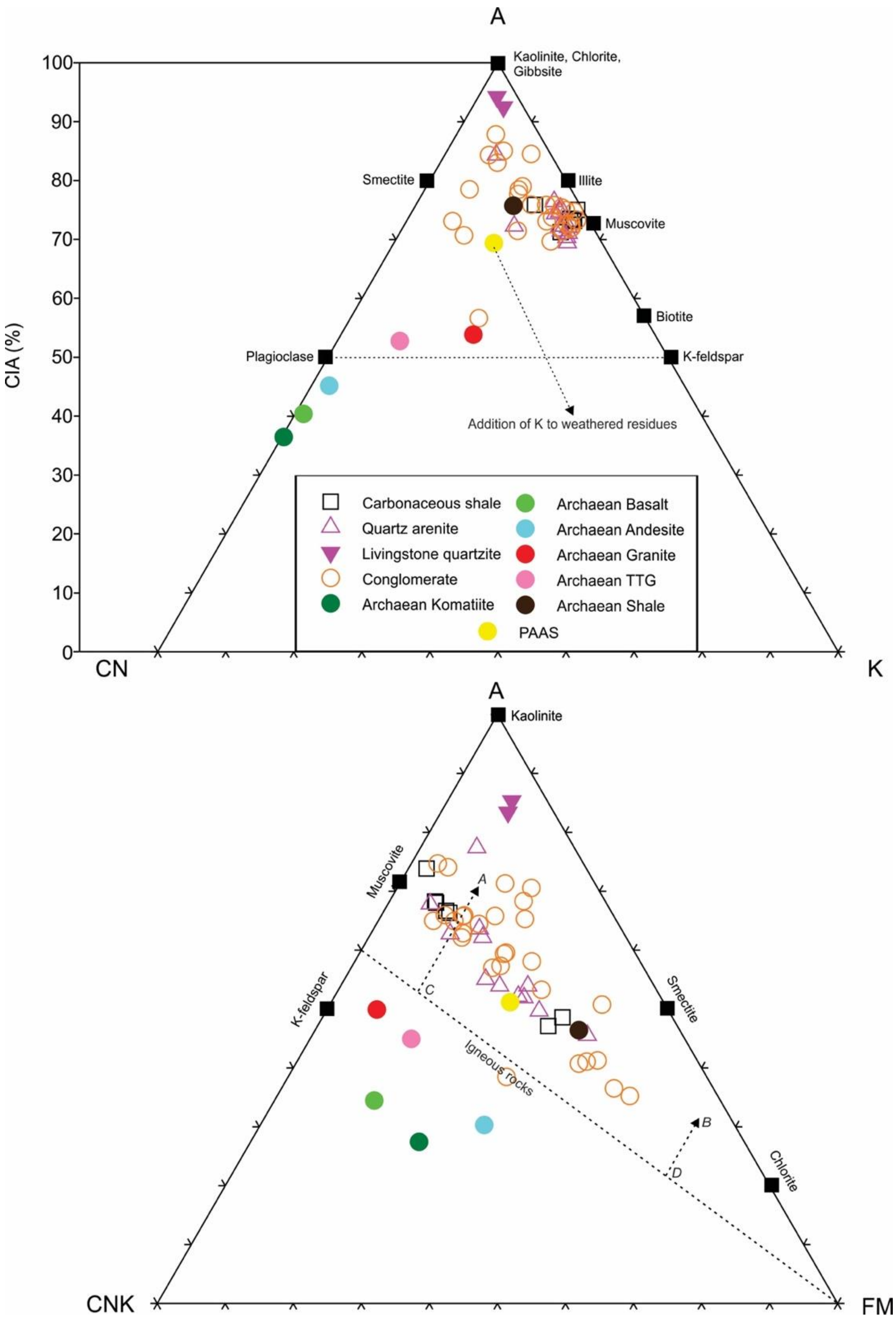

Figure 5.3: The degree of palaeoweathering and post depositional alteration the Black Reef Formation shown by (a) Chemical index of alteration (CIA) and ternary A-CN-K diagram; and (b) Ternary A-CNK-FM diagram showing the trends of weathering of a granitic source (A) and a basaltic source (B). Metasomatic and/or diagenetic transformation of kaolinite into illite with high K$^+$/H$^+$ ratios is indicated by C. Metasomatic and/or diagenetic transformation of kaolinite into chlorite with high Mg^{2+} = H$^+$ ratios is indicated by D. Adapted from Camiré et al., (1993). PAAS = post-Archaean Australian shale; TTG = tonalite-trondhjemite-granodiorite.

5.2 Lithological and mineralogical characteristics and their association with gold

Quartz-pebble conglomerate units of the Black Reef show the highest mineralisation, with the highest pyrite content and gold grade, and there are some contributing factors for this feature. Parts of the Black Reef that lie at unconformity surfaces of the VCR, Witwatersrand reefs and auriferous greenstone rocks are relatively more highly mineralised than sections that are distal from these unconformity surfaces (Frimmel, 2014; Tucker et al., 2016; Pearton and Viljoen, 2017). This spatial relationship is the most important factor for economic gold grades in the Black Reef since those proximal areas exhibit grades between 5 – 30 g/t (Fig. 4.1 – 4.3). The rounded quartz-pebbles and clast- to matrix-supported nature of the conglomerate units indicates reworked sediments from the hinterland and underlying Witwatersrand Basin and that they have travelled long distances to their depositional area. Gold is located in quartz fractures as native gold, between quartz-pebbles in carbonaceous matrix due to repeated reworking often at the bottom contact before it is subsequently chemically dissolved (Hallbauer, 1986), at pyrite grain boundaries and inside quartz microfractures as hydrothermal gold.

Pyrite grains in these conglomerate units surround the quartz-pebbles and are scattered in the matrix. Most of these pyrite grains are larger (≤2 mm) than those found in quartz arenite due to recrystallization by hydrothermal fluids containing more sulphide to react with unreacted iron-bearing phases at the surface of pre-existing pyrite grains (fluid-rock interactions), or by reworking of the underlying strata and minimal abrasion. Most authors (e.g. Hallbauer, 1986; England et al., 2002) regard DIR pyrite in this study (detrital, irregular-shaped and rounded and porous) as pyrite fragments derived from the erosion of sedimentary sources, such as the Central Rand reefs and VCR while DM pyrite in this study (detrital, massive) is regarded as derived from the erosion of granitic-greenstone from the hinterland. In contrast, the pyrite grains in the quartz arenite units are smaller (<0.5 mm) and are aligned parallel to bedding and cross-beds. This indicates that these pyrite grains are detrital, underwent greater abrasion and were deposited syngenetically. However, detrital pyrite grains are known to have a high resistance to mechanical abrasion owing to its preservation in sedimentary successions (Costa et al., 2017). This means that detrital pyrites are mostly found in areas where there was interrupted sedimentation with little oxidative weathering while rapid erosion and transportation took place, with eventual deposition in conglomeratic and arenitic beds (Utter, 1978).

On a microscopic scale, there is compositional heterogeneity of pyrite grains in the Black Reef and this observation is similar to the Witwatersrand Supergroup (Koglin et al., 2010; Agangi et al., 2015). Black Reef conglomerate contains angular fragments of broken, concentrically laminated pyrite grains, although Figures 4.12f and 4.12g show that the internal texture is still preserved. This pyrite type has been interpreted as grains that formed by replacement of carbonate or ironstone ooids (England et al., 2002). However, these grains are fragmented; thus, a replacement model for this pyrite type is unlikely to have formed at the Black Reef. A more likely source is a sedimentary precursor, with their preserved internal structure indicating short-distance transport from their source while carrying trace elements and gold between the laminae (Agangi et al., 2015). Agangi et al. (2015) analysed this pyrite type from the VCR in the Carletonville goldfield and found that they are enriched trace elements such as Sb, Mn, Au, Ag, Tl, Cu, and Mo. Black Reef could have sourced these concentrically laminated pyrite grains from the underlying VCR and Witwatersrand reefs, thus transporting detrital and mechanically recycled gold into the Black Reef and increasing the gold content in these conglomerate units.

Of particular interest is the presence of gold-rich basal conglomerate units intercalated with carbonaceous or graphitic shale – now termed 'conglomeratic shale' (Fig. 4.4a, 4.4h). The pebbles in these conglomerates are sparsely distributed, and carbonaceous material encloses most of the quartz-pebbles. These basal conglomerates intercalated with carbonaceous shale have the highest abundance of coarse-grained (~5 mm) authigenic pyrite grains in their matrix (Fig. 4.4h, 4.5) and this carbonaceous material is also embedded with fine-grained detrital and authigenic pyrite grains. The graphite is interpreted to be a product of thermal maturation of kerogen or bitumen (Mossmann et al., 2008). Microscopically, the flow of hydrocarbon fluids is evident in these 'conglomeratic shale' units because the hydrocarbons are not nodular but are embedded in the matrix surrounding quartz grains and are also oriented parallel to bedding. Interestingly, the quartz-pebbles in these units comprise fractures a few of which contain carbonaceous material (Fig. 4.4h). However, these conglomeratic shale units exhibit low gold grades. Gold assay data in the drill cores reveal gold grades of 0.1 – 1.0 g/t in the 'conglomeratic shale' - significantly lower than those recorded in the quartz-pebble conglomerate.

Sedimentary facies and stratigraphy are regarded as first-order controls on gold grade in placer deposits (Frimmel, 2018). Hallbauer (1986) evoked that there is a robust sedimentary control for gold deposits where the bulk of gold occurs (1) on foresets within the gravel deposits or in pyritic quartzite, (2) in the matrix between pebbles and (3) in various sediment traps such as small potholes and surfaces of fossilised algal mats. Phillips and Powell (1993) also highlighted that the lithological control on gold comes from the influence of strata on fluid flow and the distribution of original Fe-rich particles to form epigenetic deposits. In this study, sedimentology and grain size morphology have a controlling factor on the deposition of gold in the Black Reef. In this regard, the lack of connectivity of the quartz-pebbles may be the main feature that explains why the organic carbon-rich conglomeratic shales are typically uneconomic in terms of gold.

5.3 Gold mineralising fluids in the Black Reef

Fluid inclusions provide insight into the conditions at which minerals were formed. They provide necessary information about geological processes occurring from high temperatures at depth, moving towards low temperatures near the Earth's surface (Randive et al., 2014). They are an essential aspect for the Black Reef study since it experienced a series of deformation and metamorphic events that, in turn carried fluids responsible for gold mineralisation. This study shows that two-phase fluid inclusions with variable liquid/vapour ratios dominate the quartz-pebbles from the Black Reef. This confirms a nearly heterogeneous state of the fluid during fluid capture (Lai et al., 2015). It can also be deduced that the main composition of the fluids is aqueous, H_2O-CO_2, H_2O-CO_2-CH_4 and H_2O-H_2S-CH_4 which is similar to those found in the Witwatersrand quartz-pebble conglomerates (Drennan et al., 1999; Frimmel et al., 1999; Safonov and Prokof'ev, 2006).

Dutkiewicz et al. (1998) studied hydrocarbon fluid inclusions in the Witwatersrand Basin to identify oil in these fluid inclusions. The solid carbon inclusion in this study may represent preserved liquid hydrocarbons under high-pressure closed systems (Dutkiewicz et al., 1998). This implies that hydrocarbon generation by thermal maturation of organic matter was a process occurring in the Archean and later trapped by fluid inclusions for billions of years. Because of the absence of an ultra-violet (UV) illuminator attached to the transmitted light microscope during fluid inclusion studies, liquid carbon-rich inclusions are not classified as oil inclusion because of the lack of observed fluorescing under UV excitement. However, England et al. (2002) identified oil inclusions from Black Reef samples in the Carletonville goldfield.

The studied fluids represent a medium temperature with an average entrapment temperature of 172 ^{o}C. Only three of the studied inclusions show temperatures greater than 250 ^{o}C, where two of them are type II inclusions, and one is a type I inclusion. This type I inclusion is treated as an outlier because it shows similar parameters as the other type I inclusions besides its higher homogenisation temperature. Although three types of fluids were noted based on physical appearance (excluding mono-phase inclusions providing inconclusive data), they do not show significant differences and classes in homogenisation temperatures and composition. These fluid inclusions were trapped during successive stages of microfracturing from the observed broad range in homogenisation temperatures (Thébaud et al., 2006). In addition, these fluids occur as inclusion trails along healed microfractures that cut across several quartz grains and can therefore be classified as secondary inclusions (England et al., 2002; Thébaud et al., 2006).

Frimmel et al. (1993) studied fluid inclusions from a sample obtained from the Basal Reef in the Central Rand Group in the Welkom goldfield. They found that fluid inclusions trapped in authigenic and detrital quartz are significant because they are related to the postdepositional alteration of the placer sediments and the partial mobilisation of gold. Results of their study are presented in Table 5.1. Safonov and Prokof'ev (2006) also studied fluid inclusions in quartz cement and pebble-shaped quartz from the Black Reef, VCR and Kimberley Reef. They found three types of fluids, listed in Table 5.2. The microthermometric data and composition data obtained in these two studies are similar to those obtained in this study. It can be deduced the fluid inclusions in this study are related to ore-forming fluids that are compositionally identical to those that were responsible for mineralisation in the Witwatersrand reefs, and that they had a similar source.

Table 5.1: Summary of the microthermometric results of the ore-forming fluids of authigenic and detrital quartz in ore-bearing Basal Reef in the Welkom goldfield (Frimmel et al., 1993).

Type of quartz	Inclusion generation	T_h (ºC)	Salinity (wt% eNaCl)	Notes
Detrital and authigenic	Primary in authigenic quartz	130 - 140	7 - 17	Two-phase, mainly $CaCl_2$
	Secondary in authigenic and detrital quartz	130 - 140	<4	Small roundish, presence of KCl and NaCl
	Secondary in authigenic and detrital quartz	23.1	8 (in the aqueous part)	-58.8 ºC final melting temperature, CO_2-rich

Table 5.2: Summary of the composition of ore-forming fluids and physiochemical conditions of quartz formation in ore-bearing Black Reef and VCR (Safonov and Prokof'ev, 2006).

Type of quartz	*n*	T_h (ºC)	Salinity (wt% eNaCl)	Pressure (bar)	Notes
Cement	78	145 – 294	2.6 – 18.1	1450 – 1550	Two types of heterogeneous fluid; CO_2 prevails in the gas phase of one fluid and CH_4 and other hydrocarbons, in the gas phase of the other fluid
Pebble-shaped	98	149 – 314	2.4 – 13.5	1470 – 1780	Heterogeneous fluid with a prevalence of CO_2 in the gas phase

5.3.1 Origin of the fluids

Many fluids recorded in many Archaean gold deposits are alkaline, sulphur-bearing (sulphur predominantly in the reduced state), low salinity and are H_2O-CO_2 mixtures (Phillips and

Groves, 1983; Phillips and Powell, 1993; Phillips and Evans, 2004). The low salinity arises from metamorphic devolatilisation of mafic and/or graywacke successions such as the Klipriviersberg Group and the underlying Witwatersrand Supergroup, while the H_2O-CO_2 composition arises from devolatilisation of metamorphosed Archaean greenstone belts (Phillips and Groves, 1983; Phillips and Powell, 1993).

The classification of fluid salinities is based on various experimental freezing point depression temperature studies of aqueous-chloride solutions. Low salinity fluids are those with salinities from 0 – 10 wt% eNaCl (Bodnar, 1993). Moderately saline fluids are those with salinities from 10 – 23.20 wt% eNaCl, where 23.20 wt% eNaCl is the eutectic composition in the NaCl-H_2O system (Potter et al., 1978). Data from this study shows that there are two clusters of salinities – low salinity fluids (0.53 wt% eNaCl equivalent – 9.60 wt% eNaCl) and moderate salinity fluids (10.11 wt% NaCl equivalent – 19.05 wt% NaCl equivalent). However, an overlap of these ranges occurs, reflecting isothermal mixing processes between the two different fluid sources (Thébaud et al., 2006). Lai et al. (2015) envisaged the large range in salinity to indicate a wide variety of source fluids that may have mixed with a low salinity fluid. The source of these fluids is, however, debatable.

Suggested sources are (1) metamorphic source (e.g. Groves and Phillips, 1987); (2) magmatic source and (3) meteoric and/or seawater source (Thébaud et al., 2006). The salinity of metamorphic fluids from greenschist metamorphic facies, as experienced by the Black Reef and underlying strata, is generally low to moderate (Phillips and Powell, 1993). Based on oxygen and hydrogen isotope studies in the Carbon Leader Reef of the Carletonville goldfield, Groves and Harris (2010) concluded that the origin of the gold mineralising fluid was a mixture of metamorphic and meteoric water trapped during sedimentation and later liberated during prograde metamorphism. The studied fluid inclusions cluster at a combination of metamorphic and meteoric water mixing (Fig. 5.4). This is the primary sources of the gold transporting fluid. Metamorphic fluids from devolatilisation and dehydration of hydrous phases are characteristic of the low salinity while the meteoric fluids are characteristic of the moderate salinity (Phillips and Powell, 1993).

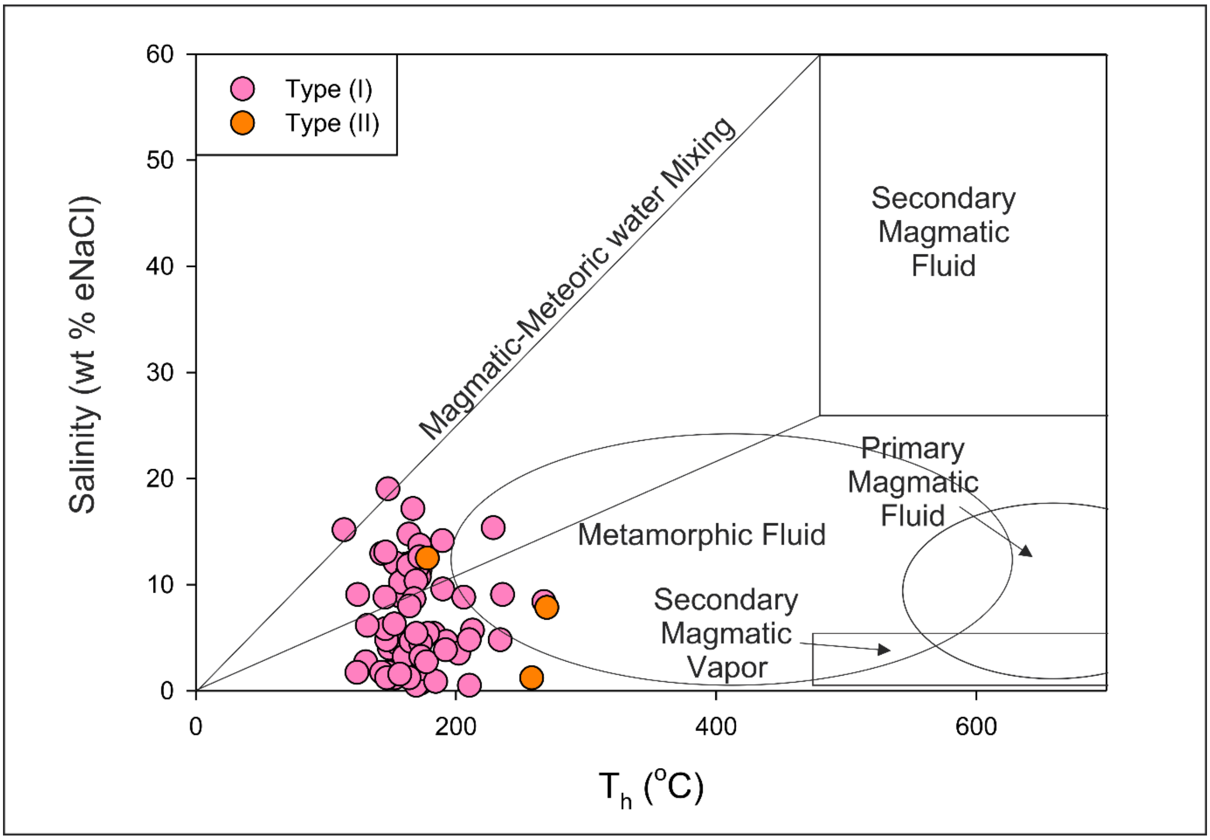

Figure 5.4: Correlation between homogenisation temperature and salinities of the fluid inclusions in the quartz-pebbles of the Black Reef Formations. Pink circles represent type I inclusions and orange circles represent type II inclusions from this study. The inclusions suggest a mixture between metamorphic and meteoric fluid sources. Fields used are obtained from Yang et al. (2013).

Origin of hydrocarbons

Petrographically, the fracture-filling pyrobitumen is interpreted as residues of migrating hydrocarbons generated by thermal maturation of organic matter through the oil window (at 100 − 150 °C – Phillips and Law, 2000; William-Jones et al., 2009) in sedimentary basins. Depending on how quickly the source rock is heated, hydrocarbons are released (Robb et al., 1992). The depth of burial and geothermal gradient of the host basin influences source rock maturation (Parnell, 1999; Dutkiewicz et al., 1999; England et al., 2002). Previously, an estimated geothermal gradient of 15 °C/km requires ~7 – 10 km of burial (Jones, 1988) while a geothermal gradient of 27 °C/km requires ~4 – 4.5 km of burial (isochore calculation for the youngest secondary fluid inclusion generation; Frimmel et al., 1993). Witwatersrand underground gold mines have already reached 4 km depth and recent work in these goldfields indicates that at a 3.8 km depth, measured rock temperatures are as high as 60 °C, with an average geothermal gradient of 9.3 ± 1.0 °C /km (Jones, 2003). Across the goldfields, at 2.5

km depths the rock temperatures are ~ 40 ^{o}C with and an average geothermal heat flux of 51 ± 6 mW/m^2 (Jones, 2018). Gibson and Jones (2002) modelled the geothermal gradients for the late Achaean and Palaeoproterozoic and found that the average geothermal gradients in the stratified rocks is between 15 – 20 ^{o}C/km. Temperatures corresponding to the oil window should have been reached post-Black Reef deposition considering the average thickness of the Transvaal succession and the lower end of the geotherm range. The presence of oil-bearing fluid inclusions in the study by England et al. (2002) provides direct evidence that oil migration took place in the Transvaal Basin through the oil window.

Researchers such as Barnicoat et al. (1997), Gray et al. (1998), Spangenberg and Frimmel (2001) and Drennan and Robb (2006) envisaged that the source rocks of the carbon seams and bitumen in the Witwatersrand reefs are within the Witwatersrand Basin, such as the Booysens Shale and shales of the Jeppestown subgroup with up to 0.42 % and 0.34 % reduced carbon, respectively. Mossman et al. (2008) observed oil-bearing fluid inclusions derived like the bitumen from thermal maturation of kerogen. They concluded that carbon originated *in situ* from living organisms in microbial mat cover due to truncations of carbon seams at palaeoerosion channels observed in the Carbon Leader Reef of the Carletonville goldfield. The source of hydrocarbons in the Black Reef is, however, unknown.

There possible sources of carbonaceous material which have been suggested for the Witwatersrand Basin include: (1) Late Archaean algal-bacterial kerogens derived from widespread microbial mats (Schidlowski, 1981), (2) shale units within the Witwatersrand Supergroup with disseminated kerogens (Robb et al., 1997; Gray at al., 1998) and (3) external sources such as the shale units in the Wolkberg Group or the carbonaceous shallow marine carbonates in the Chuniespoort Group in the Transvaal Basin (Robb et al., 1997). The two former sources are relevant for carbon seams found in the Witwatersrand Basin as the sources have been supported by δ^{13}C isotope data (Spangenberg and Frimmel, 2001) and been favoured for an indigenous origin in the form of microbial mats (Mossman et al., 2008). δ^{13}C isotope data does not support external derivation of hydrocarbons for the Witwatersrand Basin due to bulk and molecular isotope characteristics, but this is a more likely local source of carbonaceous material for the conglomerate units of the Black Reef (England et al., 2002).

5.3.2 Complexation of gold

Naturally occurring gold is Au(I) which is a soft cation likely to form covalent bonds with soft bases such as HS^-, $S_2O_3^{2-}$, CN^- and SCN^- (Phillips and Powell, 1993; Phillips and Evans, 2004; William-Jones et al., 2009). The strongest gold complex is with CN^- [e.g. $Au(CN)_2^-$], followed by $S_2O_3^{2-}$ [e.g. $Au(S_2O_3)_2^{3-}$] in oxidising conditions and HS^- [e.g. $Au(HS)_2^-$] in reducing and neutral pH conditions, and lastly SCN^- [e.g. $Au(SCN)_2^-$] if thiocyanate is concentrated (William-Jones et al., 2009). Reducing fluids will favour the ionic state of Au^+ for gold in solution (Phillips and Evans, 2004). Under very oxidising, highly saline and acidic groundwater conditions, gold occurs as Au(III) and forms stable complexes with Cl^- (e.g. $AuCl_4^-$) (Phillips and Evans, 2004). Seward (1973) noted that the most important ligand at temperatures up to 350 ^oC is reduced sulphur (i.e. HS^-), where lower pH yields AuHS and moderate pH yields $Au(HS)_2^-$. However, the stability constant for these HS^- complexes with gold reaches a maximum at 350 and 250 ^oC, respectively, meaning that above these temperatures, gold is less effectively transported as a hydrogen sulphide species (William-Jones et. al, 2009).

Gold solubility in conglomerate-hosted gold deposits relies on factors such as pressure, temperature, pH, salinity and sulphur activity (Phillips and Law, 2000). Temperatures of 300 ^oC with low salinity and stability in the muscovite field are reasonable enough conditions where gold solubility would be well above 0.1 ppm as a bisulphide complex (Phillips and Law, 2000). The maximum measured homogenisation temperature from fluid inclusion analysis is ~280 ^oC, and this is the characteristic temperature of the remobilising fluids in the Black Reef. The reaction in equation 1 controls the dissolution, hydrothermal transportation and deposition of gold at temperatures up to 350 ^oC.

$$\mathrm{Au_s} + 2\mathrm{HS^-} + \mathrm{H^+} + {}^{1}\!/_{4}\,\mathrm{O_2} \rightleftharpoons \mathrm{Au(HS)_2}^- + {}^{1}\!/_{2}\,\mathrm{H_2O} \qquad (1)$$

By applying Le Châtelier's principle, the deposition of gold in equation 1 will be favoured by a decrease in HS- and *f*O2 activity and an increase in pH. A decrease in temperature alone does not have a significant effect on the large-scale deposition of gold transported as a bisulphide complex. However, deposition of gold may be reached by a combination of a decrease in temperature and fluid mixing and/or immiscibility (Phillips and Powell, 1993). Therefore, the deposition of gold is controlled by: (1) boiling – vapourising H_2S thus lowering the concentration of HS^-; (2) decreasing reduced sulphur in the fluids by sulphidation of iron-bearing wall rocks to form pyrite or pyrrhotite; (3) interaction of fluids with carbonaceous metasediments to lower oxygen fugacity; and (4) increasing the pH of gold-bearing fluids by interaction of fluids with wall-rocks where H^+ ions are reduced through exchange with Na^+ and K^+ ions (Phillips and Groves, 1983; Phillips and Powell, 1993; Phillips and Law, 2000; Phillips and Evans, 2004).

5.3.3 The role of hydrocarbons

Complex-shaped and rounded carbon nodules are abundant in the conglomerates of the Black Reef. Their shape provides evidence for migration, indicating that they were either derived externally in the Witwatersrand Basin, travelling through reactivated pre-existing structures, or that they were derived internally in the Transvaal Basin from the Wolkberg Group or the Chuniespoort Group in the Transvaal Basin. Therefore, these carbon nodules are epigenetic (Frimmel and Hennigh, 2015). Carbon nodules are regarded as hydrothermal pyrobitumen because they occur preferentially along microfractures and arenaceous and carbonaceous matrix (Gray et al., 1998). These carbon nodules contain inclusions of gold and are commonly surrounded by pyrite grains. According to Drennan (1997), Drennan et al. (1999) and Woods (2017), carbon nodules are effective at remobilising immobile elements such as REEs, Au, Ag and Hg because the carbon nodules are isolated particles in the hydrocarbon fluids. In addition, the carbon nodules are minute, therefore, containing higher concentrations of immobile elements than the entire hydrocarbon fluids. This signifies that immobile elements would be low in concentration in the bitumen since they would be more dispersed compared to the carbon nodules (Woods, 2017). Consequently, this justifies why the carbon-rich shales are poorly mineralised in gold compared with the conglomerates because the carbon nodules are predominantly concentrated in the matrix of the conglomerates, also increasing their gold concentration.

Hydrocarbons are commonly associated with gold mineralisation as shown by the presence of liquid petroleum-bearing fluid inclusions in the ore samples from the Carlin District containing up to 100 ppm Au, and from the Witwatersrand where 40 % of the gold is in reefs with carbon seams containing up to 1000 ppm Au (William-Jones et al., 2009; Frimmel and Hennigh, 2015). The carbon seams from the Witwatersrand are regarded as remnants of cyanobacteria, producing free oxygen on their surface and therefore promoting gold precipitation by oxidation indicated by equation 2 (Frimmel and Hennigh, 2015).

$$4\mathrm{Au_s} + 8\mathrm{SO_4}^{2-} + 12\mathrm{H}^+ \rightleftharpoons 4\mathrm{Au(HS)_2}^- + 15\mathrm{O_2} + 2\mathrm{H_2O} \qquad (2)$$

However, they have also been interpreted as residues from the migration of liquid hydrocarbons (Drennan et al., 1999; Drennan and Robb, 2006) signifying that they can also aid in transportation of gold contributing to the localised remobilisation of originally syngenetic gold (Frimmel and Hennigh, 2015). William-Jones et al. (2009) focused strongly on metal transportation within oils in the Witwatersrand reefs and found that metals such as V, Ni, Cr, Mn, As, Hg, U, Fe and Au are transported in sulphur-bearing crude oil around 100 ^{o}C. The increase in temperature causes the increase the sulphur activity and therefore sulphur aids in increasing the solubility of metals and complexes metals such as Au, Ag and Hg to make them slightly soluble in hydrocarbon fluids (Phillips and Powell, 1993; William-Jones et al., 2009, Woods, 2017). The fluid inclusions in this study demonstrate a few important factors:

1) presence of H_2S indicates that sulphur was present to assist the dissolution of gold (Phillips and Groves, 1983);
2) CO_2, with carbon in the reduced oxidation state, aided in the pH buffering capacity to maintain elevated gold solubility (Phillips and Evans, 2004); and
3) organic carbon solids and methane gas indicates that hydrocarbons were present and aided the transportation of gold in solution to further distances (William-Jones, 2009).

5.3.4 Fluid pathways

Underground mapping and 3D seismic imaging in the Carletonville goldfield revealed the presence of major reverse and duplex faulting which formed after deposition of the Black Reef Formation, Chuniespoort Group and Pretoria Group (Nwaila et al., 2019). The remnants of these faults are present as microfaults seen in the Black Reef Formation units. The Pretoria Group caused burial diagenesis and low-grade metamorphism. This is presently shown by the quartz overgrowths, schistosity and healed microfaults in the quartz grains, interpreted to be compaction-related (England et al., 2002). Brittle extensional fractures in the quartz-pebbles similar to the observed quartz straining in this study are interpreted to have formed from high fluid pressures relating to fluid generation (Parnell, 1999) or from early stages of diagenesis where quartz grains are unable to support increasing overburden causing strain at a granular level and resulting in internal brittle failure and grain rotation (England et al., 2002). The well-sorted nature, high porosity and permeability of conglomerate allowed fluid flow and deposition of gold. Unconformities also direct fluid flow confined to the conglomerate units

(Phillips and Law, 2000). Various microfractures within the quartz-pebbles acted as fluid traps to deposit hydrothermal gold. This is supported by the presence of a high concentration of fluid inclusions and pyrobitumen along healed microfractures and in cavities of quartz cracks. This also suggests that the onset of oil migration occurred simultaneously with early stages of sediment burial (England et al., 2002).

Secondary permeability and reactivation of pre-existing structures in the Witwatersrand, Ventersdorp and Transvaal Supergroups caused by the Vredefort meteorite impact, allowed hydrocarbon migration and remobilisation of fluids, which have been circulating in the basin due to the Bushveld Igneous Complex, carrying gold and other ore components (Gibson et al., 1998; Frimmel et al., 1999; Frimmel and Hennigh, 2015). The outer limb of the Carletonville goldfield and the Potchefstroom synclinorium have remnants of these complex fault systems related to the Vredefort meteorite impact (Killick and Roering, 1995; Trieloff et al., 1994). It is therefore concluded that these impact-related fractures and faults are the main conduits liable for distributing gold from its source area and transported mineralising fluids even into the distal regions of the Black Reef away from underlying Witwatersrand reefs, such as the Black Reef hydrothermal gold observed in the Kaapsehoop area in the Barberton Mountain Land (de Waal and Herzberg, 1969). Fracture-filling pyrobitumen and gold filling the fractures during oil migration and the negative correlation of Au and elements concentrated in detrital minerals, such as Zr ($r = -0.17$; Fig. 4.26e) indicate short travel distance of the fluids both prior and during fracturing (Frimmel, 2005) and therefore, gold is late-stage in the paragenetic sequence of the Black Reef.

Parnell (1999) recorded that various goldfields in the Witwatersrand Basin have bitumen occupying minute fractures in quartz-pebbles. Gartz and Frimmel (1999) also reported carbon nodules in veins which cross-cut pseudochylite in the Witwatersrand Basin, attributed to the Vredefort meteorite impact. U-Pb dating of euhedral pyrite grain overgrowths in the Carbon Leader Reef suggests that the main period of auriferous hydrothermal fluid flow in the Carletonville goldfield occurred between 2.1 and 2.0 Ga (Large et al., 2013). Preliminary Re-Os model ages of various pyrite morphologies showed that the sub-rounded compact pyrite yielded ages of ~3.2 Ga, whereas rounded, massive microcrystalline pyrite yielded ~3.1 Ga, and euhedral, hydrothermal pyrite yielded ~2.0 Ga (Nwaila et al., 2019). This indicates that the main hydrothermal event took place around 2.0 Ga, a period ~32 My after the Bushveld

Igneous Complex caused fluid circulation and increase in geothermal gradient for the basin to reach the oil window.

5.4 Gold source and entrapment mechanism in the Black Reef

The Witwatersrand gold endowment enigma has been studied for over a century and yet no single area for this gold source can explain the >52 000 t of gold in this basin (Frimmel, 2018). It is well known that the hinterland hosts Archaean- granite-greenstone terranes associated with most common developments of Witwatersrand-type gold deposits (Robb et al., 1990; Law and Philips, 2006; Frimmel et al., 2005). They are an essential source of orogenic gold, such as the Barberton greenstone belt and the Pietersburg and Murchison greenstone belts (Poujol et al., 2002; Schmitz et al., 2004). However, for reasons outlined by Frimmel et al. (2005) and Frimmel and Hennigh (2015) based on mass-balance, these greenstone-hosted orogenic gold sources could not produce all the gold content found in the Witwatersrand gold reefs for a purely syn-sedimentary genetic model.

A more likely source is the entire Mesoarchaean land surface of the whole Kaapvaal Craton (Nwaila et al., 2020). In the anoxic Mesoarchaean atmosphere, acid rain leached out background concentrations of gold in the hinterland into meteoric water and transported gold as dissolved gold in river waters to near shallow seas. The dissolved gold came into contact with the photosynthetic cyanobacteria in shallow seas, resulting in the deposition of gold by oxidative precipitation in contact with these microbial mats (Frimmel, 2014) to produce fine-grained gold-rich microbial mats. These gold-rich microbial mats would have been delicate structures, prone to mechanical reworking by any high-energy wind and water. Physical reworking of the gold-rich microbial mats produced fine-grained gold that was subsequently redeposited as palaeoplacers in the Witwatersrand reefs such as the Middlevlei Reef and Kimberley Reef amongst others. The VCR was formed through the further mechanical reworking of the Witwatersrand gold. It is, therefore, highly likely that the background gold found responsible for gold mineralization in the Black Reef was sourced similarly to the Witwatersrand reefs and the VCR by mechanical reworking of underlying reefs prior to any chemical dissolution and deposition. Primary mechanical processes followed by hydrothermal activity led to gold mineralisation in the Black Reef Formation, where gold is soured from the immediate hinterland (Nwaila et al., 2019). The process of primary recycling of gold from the underlying palaeoplacers is not constrained even though mineralising postdepositional hydrothermal fluids interacted with hydrocarbon fluids within the Black Reef (Fuchs et al.,

2016) and promoted additional gold mineralisation (Nwaila et al., 2019). Background gold concentration is important, and this is observed where locally auriferous conglomerate units in the Black Reef lie at erosional and angular unconformities to auriferous Witwatersrand conglomerates, the VCR and auriferous granite-greenstone terranes.

5.4.1 Gold deposition mechanism and preservation of gold

In the Neoarchaean hydrosphere, volcanic eruptions were important to create optimal redox conditions for gold dissolution (Frimmel and Hennigh, 2015; Heinrich, 2015). Volcanic sulphur degassing controlled the Neoarchaean atmosphere where sulphur is a key component in the redox chemistry of early Earth. Mechanical reworking of gold and sediments occurred mainly at the auriferous Black Reef sites, proximal to gold-rich Archaean greenstone basement, Witwatersrand reefs and the VCR where gold was subsequently concentrated. Acid rain formed, causing chemical recycling of weathered gold that was transported as a dissolved species in Neoarchaean river waters because of the presence of reduced sulphur in solution (Frimmel, 2018). The Bushveld Igneous Complex magmatism and Vredefort meteorite impact event are the major episodes for gold concentration in the Black Reef. These events allowed fluid formation and migration, causing the further remobilisation and redissolution of gold. Reaction of this solution with iron-bearing minerals depleted the sulphide by forming pyrite and decreased gold solubility. However, gold precipitation occurred by reduction of gold complexes where it was absorbed into biotic or abiotic reduction by organic matter (Heinrich, 2015).

Fuchs et al. (2016) proposed that hydrothermal fluids assisted in the transportation of gold as bisulphide complexes and then precipitated electrochemically on pyrite and in pyrobitumen by reduction of the complexes or due to sulphidation of iron-bearing minerals as proposed in equation 1. In this study, pyrite overgrowth observed on originally rounded, massive texture pyrite grains (see Figures 4.12c and 4.13e) shows that the original pyrite grains were subject to metamorphism and local heating events to produce the new pyrite (Hallbauer and Gehlen, 1983). Hydrothermal gold is observed at the boundaries of irregular-shaped and cubic pyrite grains. This is a crucial aspect of recognising that gold has a high affinity for sulphides. The positive linear relation between Au and total sulphur in quartz arenite and conglomerate justifies the location of gold at pyrite grain edges.

Erratic concentrations of gold are experienced throughout the lateral extent of the Black Reef because of the undersaturation of gold in the fluid in contact with the host rocks (Phillips and Powell, 1993). If the mineralising sulphur-bearing fluids are undersaturated with gold, the fluids will more likely precipitate pyrite as it passes through iron-bearing (silicate) host-rock. However, as saturation of gold is achieved and the sulphur activity and fO_2 are lowered, gold will be precipitated with pyrite on the iron-bearing rocks or within the pyrite grains. The presence of native carbon in the fluid inclusions as graphite indicates a precipitation of carbon which reflects a decrease in fO_2 buffer conditions in the fluid-rock system, a similar condition like a change in redox reactions (Frezzotti et al., 2012). Host-rock also hold a significant control for gold deposition where most major Archaean gold provinces have a strong correlation with iron-rich and/or carbon-rich host-rocks (Phillips and Powell, 1993). There is not enough evidence for oxidative precipitation of gold complexes in this study because of the high activity of HS^- in the system and little support for the presence of photosynthesising organisms as microbial mats. The hydrocarbon fluids containing carbon nodules observed in the Black Reef mainly aided in dissolution and transportation of gold. The main reductant in the Black Reef would be the high amount of detrital pyrite as the Fe-bearing phase, which consumed the reduced sulphur in the mineralising fluids (Phillips and Law, 2000) while the fractures in the quartz-pebbles acted as a gold trap and the connectivity of these pebbles trapped the gold-containing carbon nodules as the fluids passed through. Therefore, hydrothermal gold was chemically precipitated in these sites and this is evidence for hydrothermal gold in the Black Reef even at distal areas from auriferous Witwatersrand conglomerates, the VCR and auriferous granite-greenstone terranes.

5.5 A reducing palaeoenvironmental atmosphere in the Neoarchaean

Many of the pyrite grains in the Black Reef Formation are locally sourced by recycling of the underlying strata. Detrital pyrite grains have been interpreted to be sourced from weathering of Archaean basement rocks in the hinterland such as the mafic rocks of the Dominion Group or greenstones of the Barberton Mountain Land (Frimmel et al., 2009; Koglin et al., 2010). Other researchers have suggested that they may be of metamorphic, igneous or hydrothermal origin related to orogenic gold systems in the hinterland (England et al., 2002; Koglin et al., 2010). Guy et al. (2014) showed that most reworked diagenetic sedimentary pyrite grains reveal positive $\delta^{34}S$ values, which suggest closed system conditions during formation below the sediment-water interface with respect to sulphate reducers. A wide range in $\delta^{34}S$ values indicates that some Witwatersrand pyrite grains formed through microbial sulphate fixation in such conditions (Hofmann et al., 2009; Large et al., 2013; Guy et al., 2014). However, the results obtained in this study coincides with those obtained by Guy et al. (2014) for reworked diagenetic pyrite grains which display positive δ^{34}S values (between ~0 and +5 ‰). It is interpreted that a continental sulphur flux became active in the Mesoarchaean to produce reworked pyrite grains of sedimentary origin, which were documented in various auriferous sedimentary successions in the Kaapvaal Craton, including the Black Reef (Barton and Hallbauer, 1996; Hofmann et al., 2009; Guy et al., 2014).

The consensus is that detrital pyrite grains are transported without modifying the δ^{34}S signature of the source material. Fluctuating oxidising and reduced conditions in Meso- and Neoarchaean basins during diagenesis stabilised both sulphate and sulphide species causing a wide range of sulphur isotope values for pyrite grains (Phillips and Law, 2000). However, the pyrite grains in this study indicate a low range in positive δ^{34}S values suggesting that reducing environments favoured the sulphide species without overprinting of any sulphate species during pyrite formation. The study by Simmons and McGloin (2020) indicated that near-zero δ^{34}S signatures are typical of Archaean to Palaeoproterozoic volcanic- and sediment-hosted deposits that are associated with having formed in sulphate-poor seawater. The δ^{34}S values on detrital pyrite grains of the Carbon Leader Reef from the Carletonville goldfield have a mean value of +1.5 ‰, suggesting that these pyrite grains represent a metamorphosed hinterland with homogenised porous diagenetic pyrite (Large et al., 2013) or these pyrite grains represent reworked sedimentary pyrite that formed under sulphate-limited conditions (Hofmann et al., 2009).

The Black Reef Formation also contains hydrothermally derived pyrite grains. Sulphur-rich fluids originating in the local basin help to explain the narrow range in δ^{34}S values, because biological and thermochemical driven fractionation was limited because of the reduced nature of oceans pre-GOE. In addition to a favoured overall reducing conditions of sedimentation during Archaean times pre-GOE, the slight positive Eu anomaly is noted for all Black Reef Formation lithology (Nwaila et al., 2017). This implies that in sediment-hosted gold deposits, the ore-forming fluids are derived from the local stratigraphy (Selvaraja et al., 2017). In hydrothermal conditions, gold is transported as a bisulphide complex, which implies that the gold was also sourced locally. Black Reef gold was sourced from the underlying Archaean basement, Witwatersrand and Ventersdorp Supergroup reefs through recycling, and remobilised over localised distances in basin-derived sulphur-rich fluids by later hydrothermal processes that precipitated gold by reduction. Gold was introduced hydrothermally and was therefore well preserved in the Black Reef Formation because of the thick sedimentary package of the Pretoria Group. All the gold in the Black Reef is epigenetic and has been preserved as an erratically developed quartz pebble conglomerate gold deposit.

Chapter 6: Conclusions

Black Reef gold mineralisation is erratically developed but is mined economically in the Carletonville goldfield with the Middlevlei Reef, Carbon Leader Reef and the VCR. This study focused on providing a mechanism for the introduction of gold in the Black Reef by investigating the association of gold with its surrounding sediments and other mineralisation. The study showed that:

1. Black Reef conglomerate and quartz arenite units are sourced from felsic rocks in the hinterland, such as granitic basement, and the underlying Witwatersrand Basin sediments. Carbonaceous shale units are sourced from more mafic rocks, such as the mafic volcanic rocks of the Ventersdorp Supergroup, and the greenstone rocks from the hinterland.
2. The whole-rock $\delta^{34}S$ values for Black Reef conglomerate is ~3.13 ‰ and for carbonaceous shale is ~3.20 ‰, which overlaps with values from the underlying pyrite-rich conglomerates from the Witwatersrand and Ventersdorp Supergroup. This indicates that Black reef pyrite grains have a similar local source of sulphur related to the surrounding stratigraphy or that the pyrite grains are sourced from the surrounding stratigraphy. Fractured concentrically laminated detrital pyrite are evidence for mechanically derived pyrite from the VCR and the Witwatersrand reefs, carrying detrital gold inclusions.
3. Remobilising and mineralising fluids are aqueous, H_2O-CO_2, H_2O-CO_2-CH_4 and H_2O-H_2S-CH_4 in composition, with organic solid C in the fluid inclusions. Microthermometric results showed homogenisation temperature between 114 ^{o}C to 270 ^{o}C, a large range indicative of trapping during successive stages of microfracturing.
4. The fluids formed by devolatilisation and dehydration reactions of hydrous minerals during prograde metamorphism at the time of emplacement of the Bushveld Igneous Complex and during the Vredefort meteorite impact event. The main hydrothermal event took place during both the Bushveld Igneous Complex event and the Vredefort meteorite impact event, where gold mineralising fluids circulated in the basin then travelled through fractures, fault systems and at unconformity boundaries.
5. Chemically recycled gold from the Witwatersrand reefs and the VCR was dissolved as a bisulphide complex, while the CO_2 aided in keeping gold in solution. Carbon nodules which were introduced hydrothermally with the hydrocarbon fluids transported soluble

gold and gold-hydrocarbon complexes into the sites of deposition during hydrothermal reworking.

6. Reduction precipitation of hydrothermal gold occurred due to sulphidation of Fe-phases to form pyrite. Black Reef gold is located at pyrite grain boundaries and is located in quartz-pebble fractures as native gold where it was trapped. The thick package of the Pretoria Group assisted with the preservation of gold, which ceased further mechanical recycling of Black Reef gold.

6.1 Recommendations

There are some limitations of the analyses and the interpretations proposed in this study which require the following recommendations:

- Black Reef Formation samples from the East Rand Goldfields should be analysed using similar techniques so that similarities and differences, if any, can be noted so that sedimentation, geochemical and isotopic characteristics can be extended throughout the lateral extent of the Black Reef.
- Oxygen and hydrogen stable isotope analyses would complement fluid inclusion studies in better defining the origin of the fluids and to quantify the amount of fluid-rock interaction.
- Carbon stable isotope analyses on organic carbon found in the fluid inclusions and on the pyrobitumen would provide the source and depositional history of the carbonaceous material present in the Black Reef and while U-Pb isotope data on bitumen will better constrain the timing of hydrocarbon production and migration in the basin.

References

African Mineral Standards, *AMIS0192,* certificate of analysis downloaded from https://www.amis.co.za/certificates-a-proficiency-reports/certificates-depleted-stock/427-amis0192-pgm-4e-14-51-g-t-merensky-western-limb-south-africa-1/file, accessed: 2020-02-29

Agangi, A., Hofmann, A, and Wohlgemuth-Ueberwasser, C. C. (2013) Pyrite zoning as a record of Mineralisation in the Ventersdorp Contact Reef, Witwatersrand Basin, South Africa. *Economic Geology*, **108**, pp. 1243 – 1272

Agangi, A., Hofmann, A., Rollin-Bard, C., Marin-Carbonne, J., Cavalazzi, B., Large, R. and Meffre, S. (2015) Gold accumulation in the Archaean Witwatersrand Basin, South Africa – Evidence from concentrically laminated pyrite. *Earth-Science Reviews*, **140**, pp. 24 – 53

Anhaeusser, C. R. (1976) Archean metallogeny in southern Africa. *Economic Geology*, **71**, pp. 16 – 43

Anhaeusser, C. R. and Viljoen, M. J. (1986) Archaean metallogeny of Southern Africa. In: Anhaeusser, C. R., Maske, S. (Eds) Mineral Deposits in Southern Africa. *Geological Society of South Africa, Johannesburg*. **(1)**, pp. 33 – 42

Antrobus, E. S. A., Brink, W. C. J., Brink, M. C., Caulkin, J., Hutchinson, R. I., Thomas, D. E., van Graan, J. A. and Viljoen, J. J. (1986) The Klerksdorp Goldfield. In: Anhaeusser, C. R., Maske, S. (Eds) Mineral Deposits in Southern Africa. *Geological Society of South Africa, Johannesburg*. **(1)**, pp. 559 – 598

Armstrong, R. A., Compston, W., Retief, E. A., Williams, I. S. and Welke, H. J. (1991) Zircon ion microprobe studies bearing the age and evolution of the Witwatersrand Triad. *Precambrian Research*. **53**, pp. 243 – 266

Barnicoat, A. C., Henderson, H. C., Knipe, R. J., Yardley, B. W. D., Napier, R. W., Fox, N. P. C., Kenyon, D. J., Muntingh, D. J., Strydom, D., Winkler, K. S., Lawrence, S. R. and Cornford, C. (1997) Hydrothermal gold mineralisation in the Witwatersrand Basin. *Nature*, **386**, pp. 820 – 824

Barton, E. S. and Hallbauer, D. K. (1996) Trace-element and U-Pb isotope compositions of pyrite types in the Proterozoic Black Reef, Transvaal Sequence, South Africa: Implications on genesis and age. *Chemical Geology,* **133**, pp. 173 – 199

Blair, T. C. and McPherson, J. G. (1999) Grain-size and textural classification of coarse sedimentary particles. *Journal of Sedimentary Research*. **69**, pp. 6 – 19

Bodnar, R. J. (1993) Revised equation and table for determining the freezing point depression of H_2O-NaCl solutions. *Geochimica et Cosmochimica Acta*, **57**, pp. 683 - 684

Bose, P. K., Eriksson, P. G., Sarkar, S., Wright, D. T., Samanta, P., Mukhopadhyay, S., Mandal, S., Banerjee, S. and Altermann, W. (2012) Sedimentation patterns during the Precambrian: a unique record? *Mar. Pet. Geol*. **33**, pp. 34 – 68

Brandl, G., Cloete, M. and Anhaeusser, C. R., (2006) Archaean greenstone belts. In: Johnson, M. R., Anhaeusser, C. R. and Thomas, R. J. (Eds) *The Geology of South Africa*. Geological Society of South Africa, Johannesburg, pp. 9 – 56

Button, A., 1973. A regional study of the stratigraphy and development of the Transvaal basin in the eastern and northeastern Transvaal. Ph.D. Thesis, University of the Witwatersrand, Johannesburg, 352 pp. (unpublished).

Button, A. (1986) The Transvaal sub-basin of the Transvaal Sequence. In: Anhaeusser, C. R., Maske, S. (Eds), Mineral Deposits in Southern Africa. *Geological Society of South Africa, Johannesburg*. **(1)**, pp. 811 – 817

Camiré, G. E., Laflèche, M. R. and Ludden, J. N. (1993) Archaean metasedimentary rocks from the northwestern Pontaic Subprovince of the Canadian Shield: chemical characterization, weathering and modelling of the source area. *Precambrian Research*. **62**, pp. 285 – 305

Chi, G., Diamond, L. W., Lu, H., Lai, J. and Chu, H. (2021) Common problems and pitfalls in fluid inclusion study: A review and discussion. *Minerals*, **11**, 23pp.

Clendenin, C. W., Charlesworth, E. G., Maske, S. and de Gasparis, A. A. (1988) Normal simple model for the structural evolution of the early Proterozoic Ventersdorp Supergroup, southern Africa. *Economic Geology Research Unit, University of the Witwatersrand*, information circular no. **201**, 20pp

Clendenin, C. W., Henry, G. and Charlesworth, E. G. (1991) Characteristics of and influences on the Black Reef depositional sequence in the eastern Transvaal. *South African Journal of Geology*, **94**, pp. 321 – 327

Condie, K. C. (1993) Chemical composition and evolution of the upper continental crust: contrasting results from surface samples and shales. *Chemical Geology*, **104**, pp. 1 – 37

Costa, G., Hofmann, A. and Agangi, A. (2017) Provenance of detrital pyrite in Archean sedimentary rock: Examples from the Witwatersrand Basin. In: Mazumder, R. (Ed.) *Sediment Provenance: influences on compositional change from source to sink.* Amsterdam, Elsevier., **18**, pp. 509 – 531

Costa, G., Hofmann, A. and Agangi, A. (2020) A revised classification scheme of pyrite in the Witwatersrand Basin and application to placer gold deposits. *Earth-Science Reviews*, **201**

de Kock, W. P. (1940) The Ventersdorp Contact Reef: Its nature, mode of occurrence and economic significance – with special reference to the Far West Rand. *Trans. geol. Soc. S. Afr.*, **43**, pp. 85 – 107

de Kock, W. P. (1964) The geology and economic significance of the West Wits Line. In: Haughton, S. H. (Ed.) *The geology of some ore deposits in Southern Africa*. Geological Society of South Africa, Johannesburg **(1)**, pp. 323 – 386

De Waal, S.A. and Herzberg, W. (1969) Uranium and gold mineralization of the Black Reef Series in the Kaapsehoop area, Nelspruit district, eastern Transvaal. *Ann. Geol. Surv., S. Afr.*, **7**, pp. 111 – 119

Dirks, P. H. G. M., Charlesworth, E. G., Munyai, M. R. and Wormald, R. (2013) Stress analysis, post-orogenic extension and 3.01Ga gold mineralisation in the Barberton Greenstone Belt, South Africa. *Precambrian Research*, **226**, pp. 157 – 184

Domagal-Goldman, S. D., Poirier, B. and Wing, B. (2011) Mass-Independent Fractionation of sulfur isotopes: carriers and sources. A summary report from a workshop

Drennan. G. R. (1997) Fluid inclusion microthermometry of the Witwatersrand Basin, South Africa. PhD Thesis, University of the Witwatersrand, Johannesburg, 256p (unpublished)

Drennan, G. R. and Robb, L. J. (2006) The nature of hydrocarbons and related fluids in the Witwatersrand Basin, South Africa: their role in metal redistribution. In. Reimold, W. U. and Gibson (Eds), R. L. Processes on the Early Earth, *Geological Society of America Special Paper*. **405**, pp. 353 – 385

Drennan, G. R., Boiron, M–C., Cathelineau, M. and Robb, L. J. (1999) Characteristics of post-depositional fluids in the Witwatersrand Basin. *Mineralogy and Petrology*, **66**, pp. 83 – 109

Dutkiewicz, A., Rasmussen, B. and Buik, R. (1998) Oil preserved in fluid inclusions in Archean sandstones. *Nature*, **395**, pp. 885 – 888

Els, B. G. (1987) The auriferous Middlevlei Reef depositional system, West Wits Line, Witwatersrand Supergroup. PhD (Geology) [Unpublished]: University of Johannesburg. Retrieved from https://ujdigispace.uj.ac.za (Accessed: 13 January 2020)

Els, B. G. (1998) The auriferous late Archaean sedimentation systems of South Africa: unique palaeo-environmental conditions? *Sedimentary Geology*, **120**, pp. 205 – 224

Els, B. G., van den Berg, W. A. and Mayer, J. J. (1995) The Black Reef Quartzite Formation in the western Transvaal: sedimentological and economic aspects, and significance for basin evolution. *Mineralium Deposita*, **30**, pp. 112 – 123

Engelbrecht, C. J ., Baumbach, G. W. S., Matthysen, J. L. and Fletcher, P. (1986) The West Wits Line. In: Anhaeusser, C. R., Maske, S. (Eds), Mineral Deposits in Southern Africa. *Geological Society of South Africa, Johannesburg*. **(1)**, pp. 649 – 688

England, G., L., Rasmussen, B., Krapež, B. and Groves, D. I. (2002) Archaean oil migration in the Witwatersrand Basin of South Africa. *Journal of the Geological Society, London*, **159**, pp. 189 – 201

Eriksson, P. G., Altermann, W. and Hartzer, F. J. (2006) The Transvaal supergroup and precursors. In: Johnson, M. R., Anhaeusser, C. R. and Thomas, R. J. (Eds) *The geology of South Africa. Johannesburg,* Geological Society of South Africa. pp. 237 – 26

Eriksson, P. G., Hatting, P. J. and Altermann, W. (1995) An overview of the geology of the Transvaal Sequence and Bushveld Complex, South Africa. *Mineralium Deposita*, **30**, pp. 98 – 111

Eriksson, P. G., Schweitzer, J. K., Bosch, P. J. A., Schereiber, U. M., van Deventer, J. L. and Hatton, C. J. (1993) The Transvaal Sequence: an overview. *Journal of African Earth Sciences*, **16**, pp. 25 – 51

Farquhar, J., Bao, H. and Thiemens, M. (2000) Atmospheric influence of Earth's earliest sulfur cycle. *Science*. **289**, pp. 756 – 758

Farquhar, J., Cliff, J., Zerkle, A. L., Kamyshny, A., Poulton, S. W., Claire, M., Adams, D. and Harms, B. (2013) Pathways for Neoarchean pyrite formation constrained by mass-independent sulfur isotopes. *PNAS*. **110**, pp. 17638 – 17643

Frezzotti, M. L., Tecce, F. and Casagli, A. (2012) Raman spectroscopy for fluid inclusion analysis. *Journal of Geochemical Exploration*. **112**, pp. 1 – 20

Frimmel, H. E. and Hennigh, Q. (2015) First whiffs of atmospheric oxygen triggered onset of crustal gold cycle. *Mineralium Deposita*, **50**, pp. 5 – 23

Frimmel, H. E. and Minter, W. E. L. (2002) Recent developments concerning the geological history and genesis of the Witwatersrand gold deposits, South Africa. *Society of Economic Geologists Special Publication*, **9**, pp. 17 – 45

Frimmel, H. E. (1997) Detrital origin of hydrothermal Witwatersrand gold – a review. *Terra Nova*, **9**, pp. 192 – 197

Frimmel, H. E. (2005) Archaean atmospheric evolution: evidence from the Witwatersrand goldfields, South Africa. *Earth Science Reviews,* **70**, pp. 1 – 46

Frimmel, H. E. (2014) A giant Mesoarchaean crustal gold-enrichment episode: Possible causes and consequences for exploration. *Society of Economic Geologists Special Publication,* **18**, pp. 209 – 234

Frimmel, H. E. (2018) Episodic concentration of gold to ore grade through Earth's history. *Earth-Science Reviews*, **180**, pp. 148 – 1858

Frimmel, H. E., Groves, D. I., Kirk, J., Ruiz, J., Chesley, J. and Minter, W. E. L. (2005) The formation and preservation of the Witwatersrand Goldfields, the world's largest gold province. *Economic Geology 100th Anniversary Volume*, pp. 769 – 797

Frimmel, H. E., Hallbauer, D. K. and Gartz, V. H. (1999) Gold mobilising fluids in the Witwatersrand Basin: composition and possible sources. *Mineralogy and Petrology*, **66**, pp. 55 – 81

Frimmel, H. E., Le Roex, A. P., Knight, J. and Minter, W. E. L. (1993) A case study of the post-depositional alteration of the Witwatersrand Basal Reef gold placer. *Economic Geology*, **88**, pp. 249 – 265

Frimmel, H. E., Zeh, A., Lehrmann, B., Hallbauer, D. K. and Frank, O. (2009) Geochemical and geochronological constraints on the nature of the immediate basement beneath the Mesoarchaean auriferous Witwatersrand Bain, South Africa. *Journal of Petrology*, **50**, pp. 2187 – 2220

Fuchs, S. H. J., Schuman, D., William-Jones, A. E. and Vali, H. (2015) The growth and concentration of uranium and titanium minerals in hydrocarbons of the Carbon Leader Reef, Witwatersrand Supergroup, South Africa. *Chemical Geology*, **393 – 394**, pp. 55 – 66

Fuchs, S. H. J., Schumann, D., William-Jones, A. E., Murray, A. J., Couillard, M., Lagared, K., Phaneuf, M. W. and Vali, H. (2017) Gold and uranium concentration by interaction of immiscible fluids (hydrothermal and hydrocarbon) in the Carbon Leader Reef, Witwatersrand Supergroup, South Africa. *Precambrian Research*, **239**, pp. 39 – 55

Fuchs, S. H. J., William-Jones, A. E. and Przybylowicz, W. J. (2016) The origin of the gold and uranium ores of the Black Reef Formation, Transvaal Supergroup, South Africa. *Ore Geology Reviews*, **72**, pp. 149 – 164

Gartz, H. H. and Frimmel, H. E. (1999) Complex metasomatism of an Archean placer in the Witwatersrand Basin, South Africa: The Ventersdorp Contact Reef – A hydrothermal aquifer? *Economic Geology*, **94**, pp. 689 – 706

Gauert, C. D. K., Brauns, M., Batchelor, D. and Simon, R. (2011) Gold Provenance of the Black Reef Conglomerate, West and East Rand, South Africa. *SGA conference paper*, pp. 1 – 3

Gibson, R. L. and Jones, M. Q. W. (2002) Late Archaean to Palaeoproterozoic geotherms in the Kaapvaal craton, South Africa: constraints on the thermal evolution of the Witwatersrand Basin. *Basin Research*, **14**, pp. 169 – 181

Gibson, R. L., Reimold, W. U. and Stevens, G. (1998) Thermal-metamorphic signature of an impact event in the Vredefort dome, South Africa. *Geology*. **26**,pp. 787 – 790

Gibson, R.L., Reimold, W.U., Phillips, D., and Layer, P.W. (2000), ^{40}Ar/^{39}Ar constraints on the age of metamorphism in the Witwatersrand Supergroup, Vredefort dome (South Africa). *South African Journal of Geology*, **103**, pp. 175 – 190.

Glazner, A. F. (1988) Stratigraphy, structure and potassic alteration of Miocene volcanic rocks in the Sleeping Beauty area, central Mojave Desert, California. *Geological Society of America Bulletin*. **100**, pp. 424 – 435

Gray, G. J., Lawrence, S. R., Kenyon, K. and Cornford, C. (1998) Nature and origin of carbon in the Archean Witwatersrand Basin, South Africa. *Journal of the Geological Society of London*. **155**, pp. 39 – 59

Groves, D. and Harris, C. (2010) O- and H-isotope study of the Carbon Leader Reef at the TauTona and Savuka Mines (western deep levels), South Africa: Implications for the origin and evolution of the Witwatersrand Basin fluids. *South African Journal of Geology*, **113**, pp. 1 – 14

Groves, D. I. and Phillips, G. N. (1987) The genesis and tectonic control on Archaean gold deposits of the Western Australian Shield – a metamorphic replacement model. *Ore Geology Reviews*. **2**, pp. 287 – 322

Guy, B. M., Ono, S., Gutzmer, J., Lin, Y. and Beukes, N. J. (2014) Sulfur sources of sedimentary “buckshot” pyrite in the auriferous conglomerates of the Mesoarchean Witwatersrand and Ventersdorp Supergroups, Kaapvaal Craton, South Africa. *Mineralium Deposita*. **49**, pp. 751 – 775

Hallbauer, D. K. (1975) The plant origin of Witwatersrand carbon. *Mineral Science Engineering*. **7**, pp. 111 – 131

Hallbauer, D. K. (1986) The mineralogy and geochemistry of Witwatersrand pyrite, gold, uranium and carbonaceous matter. In: Anhaeusser, C. R., Maske, S. (Eds), Mineral Deposits in Southern Africa. *Geological Society of South Africa, Johannesburg*. **(1)**, pp. 811 – 817

Hallbauer, D. K. and Kable, E. J. D. (1982) Fluid inclusion and trace element content of quartz and pyrite pebbles from the Witwatersrand conglomerates: their significance with respect to the genesis of primary deposits. *Ore Genesis*, **2**, pp. 742 – 752

Hallbauer, D. K. and von Gehlen, K. (1983) The Witwatersrand pyrites and metamorphism. *Mineralogical Magazine*, **47**, pp. 473 – 479

Hammond, N. Q. and Moore, J. M. (2006) Archaean lode gold mineralisation in banded iron formation at the Kalahari Goldridge deposit, Kraaipan Greenstone Belt, South Africa. *Mineralium Deposita*, **41**, 483 – 503

Heinrich, C. A. (2015) Witwatersrand gold deposits formed by volcanic rain, anoxic rivers and Archaean life. *Nature Geoscience*. **8**, pp. 206 – 209

Henry, G. and Master, S. (2008) Black Reef Project, internal report, *Council Scientific Industrial Research*, **31 March 2008**, 61p.

Hofmann, A., Bekker, A., Rouxel, O., Rumble, D. and Master, S. (2009) Multiple sulphur and iron isotope composition of detrital pyrite in Archaean sedimentary rocks: A new tool for provenance analysis. *Earth and Planetary Science*, **286**, pp. 436 – 445

Jones, M. Q. W. (1988) Heat flow in the Witwatersrand Basin and its environs and its significance for the South Africa shield geotherm and lithosphere thickness. *Journal of Geophysical Research*, **93**, pp. 3243 – 3260

Jones, M. Q. W. (2003) An update in virgin rock temperature analysis of the Witwatersrand Basin. *Journal of the Mine Ventilation Society of South Africa*, **56**, pp. 107 – 112

Jones, M. Q. W. (2018) Virgin rock temperatures and geothermal gradients in the Bushveld Complex. *Journal of the Southern African Institute of Mining and Metallurgy*, **118**, pp. 671 – 680

Kamo, S. L., Key, R. M. and Daniels, L. R. M. (1995) New evidence for Neoarchaean hydrothermally altered granites in south-central Botswana. *Journal Geological Society of London*, **152**, pp. 747 – 750

Kamo, S. L., Reimold, W. U., Krogh, T. E. and Colliston, W. P. (1996) A 2.023 Ga age for the Vredefort impact event and the first report of shock metamorphosed zircons in pseudotachylitic breccias and granophyre. *Earth Planetary Science Letters*, **144**, pp. 369 – 387

Kent, L. E. (1980) Stratigraphy of South Africa. I: Lithostratigraphy of the Republic of South Africa, southwest Africa, Namibia and the Republics of Bophuthatswana, Transkei and Venda. South African Committee for Stratigraphy (SACS), *Geological Survey*, Handbook 8

Killick, A. M. and Roering, C. (1995) The relative age of pseudotachylite formation in the West Rand region, Witwatersrand basin, South Africa, as deduced from structural (sic) observations. *South African Journal of Geology*. **98**, pp. 78 – 81

Kirk, J., Ruiz, J., Chesley, J., Titley, S. and Walshe, J. (2001) A detrital model for the origin of gold and sulphides in the Witwatersrand basin based on Re-Os isotopes. *Geochemica et Cosmochimica Acta*, **65**, pp. 2149 – 2159

Kirk, J., Ruiz, J., Chesley, J., Walshe, J. and England, G. (2002) A major Archaean, gold- and crust-forming event in the Kaapvaal Craton, South Africa. *Science Magazine*, **297**, pp. 1856 – 1858

Koglin, N., Frimmel, H. E., Minter, W. E. L. and Bratz, H. (2010) Trace-element characteristics of different pyrite types in Mesoarchaean to Palaeoproterozoic placer deposits. *Mineralium Deposita*, **45**, pp. 259 – 280

Kositcin, N. and Krapež, B. (2004) SHRIMP U-Pb detrital zircon geochronology of the Late Archaean Witwatersrand Basin of South Africa: relation between zircon provenance age spectra and basin evolution. *Precambrian Research*, **29**, pp. 141 – 168

Lai, J., Ju, P. J., Tao, J., Yang, B. and Wang, X. (2015) Characteristics of fluid inclusions and metallogenesis of Annage gold deposit in Qinghai Province, China. *Open Journal of Geology*, **5**, pp. 780 – 794

Large, R. R., Meffre, S., Burnett, R., Guy, B., Bull, S., Gilbert, S., Goemann, K. and Danyushevsky, L. (2013) Evidence for intrabasinal source and multiple concentration processes in the formation of the Carbon Leader Reef, Witwatersrand Supergroup, South Africa. *Economic Geology*, **108**, pp. 1215 – 1241

Laurent, O., Zeh, A., Brandl, G., Vezinet, A. and Wilson, A. (2019) Granitoids and greenstone belts of the Pietersburg Block – Witnesses of an Archaean accretionary orogen along the northern edge of the Kaapvaal Craton. In: Kröner, A. and Hofmann, A. (Eds) *The Archaean Geology of the Kaapvaal Craton, Southern Africa*, Regional Geology Reviews, Springer, Cham, pp. 83 – 107

Law, J. D. and Phillips, G. N. (2005) Hydrothermal replacement model for Witwatersrand god. *Economic Geology 100th Anniversary Volume*, **100**, pp. 799 – 811

Law, J. D. and Phillips, G. N. (2006) Witwatersrand gold- pyrite-uraninite deposits do not support a reducing Archean atmosphere. *Geological Society of America Memoir*, **198**, pp. 121 – 141

Mossmann, D. J. and Thompson-Rizer, C. L. (1993) Toward a working nomenclature and classification of organic matter in Precambrian (and Phanerozoic) sedimentary rocks. *Precambrian Research*, **61**, pp. 171 – 179

Muntean, J. L., Frimmel, H. E., Phillips, N., Law, J. and Myers, R. (2005) Controversies in the origin of world-class gold deposits, Part II: Witwatersrand gold deposits. *SEG Newsletter*, **60**, pp. 7 – 19

Mossmann, D. J., Minter, W. E. L., Dutkiewicz, A., Hallbauer, D. K., George, S. C., Hennigh, Q., Reimer, T. O. and Horscroft, F. D. (2008) The indigenous origin of Witwatersrand “carbon”. *Precambrian Research*, **164**, pp. 173 – 186

Nwaila, G. T., Durrheim, R. J., Jolayemi, O. O., Maselela, H. K., Jakaite, L. and Burnett, M. (2020) Significance of granite-greenstone terranes in the formation of Witwatersrand-type gold mineralisation – a case study of the Neoarchaean Black Reef Formation, South Africa. *Ore Geology Reviews*. **121**, 19 pp.

Nwaila, G. T., Frimmel, H. E. and Minter, W. E. L. (2017) Provenance and geochemical; variations in shales of the Mesoarchean Witwatersrand Supergroup. *The Journal of Geology*. **125**, pp. 399 – 422

Nwaila, G. T., Manzi, M. S. D., Kirk, J., Maselela, H. K., Durrheim, R. J., Rose, D. H., Nwaila, P. C., Bam, L. C. and Khumalo, T. (2019) Recycling of paleoplacer gold through mechanical and postdepositional mobilization in the Neoarchean Black Reef Formation, South Africa. *The Journal of Geology*. **127**, pp. 137 – 166

Obbes, A.M. (1995) The structure, stratigraphy and sedimentology of the Black Reef-Malmani-Rooihoogte succession of the Transvaal Supergroup southwest of Pretoria. *Bull. Counc. Geosci*. **127**, 89p.

Ore Research & Exploration, *OREAS 45e,* certificate of analysis downloaded from https://www.ore.com.au/downloads/?fileId=733, accessed: 2020-02-29

Ore Research & Exploration, *OREAS 45d,* certificate of analysis downloaded from https://www.ore.com.au/downloads/?fileId=731, accessed:2020-02-09

Ore Research & Exploration, *OREAS 25a,* certificate of analysis downloaded from https://www.ore.com.au/crm/oreas-25a/ , accessed:2020-02-09

Parnell, P. (1999) Petrographic evidence for emplacement of carbon into Witwatersrand conglomerates under high fluid pressure. *Journal of Sedimentary Research*, **69**, pp.164 – 170

Partridge, M. A., Golding, S. D., Baublys, K. A. and Young, E. (2008) Pyrite paragenesis and multiple sulphur isotope distribution in late Archean and early Paleoproterozoic Hamersley Basin sediments. *Earth and Planetary Science Letters*, **272**, pp. 41 – 49Pearton, T. and Viljoen, M. (2017) Gold on the Kaapvaal Craton, outside the Witwatersrand Basin, South Africa. *South African Journal of Geology*, **120**, pp. 101 – 132

Phillips, G. N. and Evans, K. A. (2004) Role of CO_2 in the formation of gold deposits. *Nature*, **429**, pp. 860 – 863

Phillips, G. N. and Groves, D. I. (1983) The nature of Archaean gold-bearing fluids deduced from gold deposits of Western Australia. *Journal of the Geological Society of Australia*, **30**, pp. 25 – 39

Phillips, G. N. and Powell, R. (1993) Link between Gold Provinces. *Economic Geology*, **88**, pp. 1084 – 1098

Phillips, G. N. and Powell, R. (2011) Origin of Witwatersrand gold: a metamorphic devolatilisation-hydrothermal replacement model. *Applied Earth Science*, **120**, pp. 112 – 129

Phillips, G. N., Law, J. D. M. and Myers, R. E. (1990) The role fluids in the evolution of the Witwatersrand Basin. *South African Journal of Geology*, **93**, pp. 54 – 69

Phillips, G. N. and Law, J. D. M. (1994) Metamorphism of the Witwatersrand gold fields: A review. *Ore Geology Reviews*, **9**, pp. 1 – 31

Phillips, G. N. and Law, J. D. M. (2000) Witwatersrand gold fields: Geology, genesis and exploration. *SEG Reviews*, **13**, pp. 439 – 500

Phillips, G. N. and Powell, R. (2015) Hydrothermal alteration in the Witwatersrand goldfields. *Ore Geology Reviews*, **65**, pp. 245 – 273

Potter, R. W., Clynne, M. A. and Brown, D. L. (1978) Freezing point depression of aqueous sodium chloride solutions. *Economic Geology*, **73**, pp. 284 – 285

Poujol, M. and Anhaeusser, C. R. (2001) The Johannesburg Dome, South Africa, new single zircon U-Pb isotopic evidence for early Archaean granite-greenstone development within the central Kaapvaal Craton. *Precambrian Research*, **108**, pp. 139 – 157

Poujol, M., Anhaeusser, C. R. and Armstrong, R. A. (2002) Episodic granitoid emplacement in the Archaean Amalia–Kraaipan terrane, South Africa: confirmation from single zircon U–Pb geochronology. *Journal of African Earth Science,* **35**, pp. 47 – 161

Poujol, M., Robb, L. J., Anhaeusser, C. R. and Gericke, B. (2003) A review of the geochronological constraints on the evolution of the Kaapvaal Craton, South Africa. *Precambrian Research*, **127**, pp. 181 – 213

Randive, K. R., Hari, K. R., Dora, M. L., Malpe, D. B. and Bhondwe, A. A. (2014) Study of fluid inclusions: Methods, techniques and applications. *Gondwana Geological Magazine*, **29**, pp. 19 – 28

Rasmussen, B., Fletcher, I. R., Muhling, J. R., Mueller, A. G. and Hall, G. C. (2007) Bushveld-ages fluid flow, peak metamorphism, and gold mobilization in the Witwatersrand basin, South Africa: Constraints from in situ SHRIMP U-Pb dating of monazite and xenotime. *Geology*, **35**, pp. 931 – 934

Robb, L. J. and Meyer, F. M. (1995) The Witwatersrand Basin, South Africa, South Africa: geological framework and mineralization processes. *Ore Geology Reviews*, **10**, pp. 67 – 94

Robb, L. J., Davis, D. W. and Kamo, S, L. (1990) U-Pb ages on single detrital zircon grains from the Witwatersrand Basin, South Africa: constraints on the age of sedimentation and the evolution of granites adjacent to the basin. *Journal of Geology*, **98**, pp. 311 – 328

Robb, L. J., Charlesworth, E. G., Drennan, G. R., Gibson, R. L. and Tongu, E. L. (1997) Tectonometamorphic setting and paragenetic sequence of Au-U mineralization in the Archaean Witwatersrand Basin, South Africa. *Australian Journal of Earth Science*, **44**, pp. 353 – 371

Robb, L. J., Landais, P., Meyer, F. M. and Davis, D. W. (1992) Nodular kerogen in granites: implications for the origin of carbonaceous matter in the Witwatersrand Basin, South Africa. **EGRI**, University of the Witwatersrand, **255**, 15pp.

Safonov, Y. G. and Prokof'ev, V. Y. (2006) Gold-bearing reefs of the Witwatersrand Basin: A model of synsedimetation hydrothermal formation. *Geology of Ore Deposits*, **48**, pp. 415 – 447

Seward, T. M. (1973) Thio complexes of gold and the transport of gold in hydrothermal ore solutions. *Geochimica et Cosmochimica Acta*. **37**, pp. 379 – 399

Sharpe, J. W. N. (1949) The economic auriferous bankets of the Upper Witwatersrand beds and their relationship to sedimentation features. *South African Journal of Geology*, **52**, pp. 265 – 288

Schidlowski, M. (1981) Uraniferous constituents of the Witwatersrand conglomerates: Ore-microscopic observations and implications for the Witwatersrand metallogeny. *U.S. Geological Survey Professional Paper*, **USGS-PP—1161-A-BB**

Schmitz, M. D., Bowring, S. A., de Wit, M. J. and Gartz, V. (2004) Subduction and terrane collision stabilized the Kaapvaal Craton tectosphere 2.9 billion years ago. *Earth Planetary Science Letters,* **222**, pp. 363 – 376

Selvaraja, V., Fiorentini, M. L., Jeon, H., Savard, D. D., LaFlamme, C. K., Guagliardo, P., Caruso, S. and Bui, T. (2017) Evidence of local sourcing of sulfur and gold in an Archaean sediment-hosted gold deposit. *Ore Geology Reviews,* **89**, pp. 909 – 930

Simmons, J. M. and McGloin, M. V. (2020) Sulphide δ^{34}S composition of Palaeoproterozoic mineralisation in the Aileron Province, central Australia: an igneous sulphur source? *Northern Territory Geological Survey*. **2020-005**

Söhnge, A. P. G. (1986) Mineral provinces of Southern Africa. In: Anhaeusser, C. R., Maske, S. (Eds), Mineral Deposits in Southern Africa. *Geological Society of South Africa, Johannesburg*. **(1)**, pp. 1 – 23

Spangenberg, J. E. and Frimmel, H. E. (2001) Basin-internal derivation of hydrocarbons in the Witwatersrand Basin, South Africa: evidence from bulk and molecular δ^{13}C data. *Chemical Geology,* **173**, pp. 339 – 255

Steele-MacInnis, M., Lecumberri-Sanchez, P., Bodnar, R.J.(2012) HOKIEFLINCS_H2O-NACL: A Microsoft Excel spreadsheet for interpreting microthermometric data from fluid inclusions based on the PVTX properties of H2O-NaCl. *Computers & Geosciences,* **49**, pp. 334 – 337

Stumm, N. and Morgan, N. (1981) Aquatic chemistry: and introduction emphasizing chemical equilibria in natural waters. **Ed. 2**. New York, Wiley.

Sutton, S. J. and Maynard, J. B. (1993) Sediment- and basalt-hosted regoliths in the Huronian Supergroup: role of parent lithology in middle Precambrian weathering profiles. *Canadian Journal of Earth Science*, **30**, pp. 60 – 76

Taylor, R. D. and Anderson, E. D. (2018) Quartz-pebble-conglomerate gold deposits: U.S. Geological Survey Scientific Investigations Report 2010-5070-P, 34 pp, https://doi.org/10.3133/sir20105070P

Taylor, S. R. and McLennan, S. M. (1985) The continental crust: its composition and evolution. Oxford, Blackwell, 312p.

Thébaud, N., Philippot, P., Rey, P. and Cauzid, J. (2006) Composition and origin of fluids associated with lode gold deposits in a Mesoarchean greenstone belt (Warrawoona Syncline, Pilbara Craton, Western Australia) using synchrotron radiation X-ray fluorescence. *Mineralogy and Petrology*. **152**, pp. 485 – 503

Trieloff, M., Reimold, W. U., Kunz, J., Boer, R. H. and Jessberger, E. K. (1994) ^{40}Ar-^{39}Ar thermochronology of pseudotachylite at the Ventersdorp Contact Reef, Witwatersrand Basin. *South African Journal of Geology*. **97**, pp. 365 – 384

Tucker, R. F., Viljoen, R. P. and Viljoen, M. J. (2016) A review of the Witwatersrand Basin – The world's greatest goldfield. *Episodes*, **39**, pp. 105 – 133

Wallmach, T. and Meyer, F. (1990) A petrogenetic grid for metamorphosed aluminous Witwatersrand shales. *South African Journal of Geology*, **93**, pp. 93 – 102

William-Jones, A. E., Bowell, R. J. and Migdisov, A. A. (2009) Gold in solution. *Elements*, **5**, pp. 281 – 287

USGS (2000) USGS reference materials certificate of analysis index (geochemical reference standards). http://minerals.cr.usgs.gov/geo_chem_stand/

Utter, T. (1978) Morphology and geochemistry of different pyrite types from the Upper Witwatersrand System of the Klerksdorp Goldfield, South Africa. *Geologische Rundschau*, **67**, pp.774 – 804.

Woods, T. (2017) Developing an advanced understanding of Au-U-C associations in the Witwatersrand Basin: Using traditional and experimental techniques. PhD Thesis submitted to University of the Witwatersrand 1-167

Yang, Y., Ye, L., Cheng, Z. and Bao, T. (2013) Origin of fluids in the Hetaoping Pb-Zn deposit, Baoshan-Narong-Dongzhi block metallogenic belt, Yunnan Province, SW China. *Journal of Asian Earth Sciences*. **73**, pp. 362 – 371

Zeh, A., Ovtcharova, M., Wilson, A. H. and Schaltegger, U. (2015) The Bushveld Complex was emplaced and cooled in less than one million years – results of zirconology, and geotectonic implications. *Earth Planetary Science Letters*, **418**, pp. 103 – 114

Zeh, A., Wilson, A., H. and Gerdes, A. (2020) Zircon U-Pb-Hf isotope systematics of the Transvaal Supergroup – Constraints for the geodynamic evolution of the Kaapvaal Craton and its hinterland between 2.65 and 2.06 Ga. *Precambrian Research*, **345**, pp. 1 – 20

Ziemnaik, S. E., Jones, M. E. and Combs, K. E. S. (1993) Solubility and phase behaviour of Cr(III) oxides in alkaline media at elevated temperatures. *Journal of Solution Chemistry*. **27**, pp. 33 – 66

Appendices

Appendix A: Core logging descriptions on the different boreholes

BH ID	Depth	Sample ID	Rock type	Sample description
D8P04251	14.38-14.67	TK-51-01A	Conglomerate	30 cm: very coarse grained quartzite, black colour, few scattered white and grey qtz grains that are 12 mm, sorted, polymictic with chert grains, rounded and elongated grains, weakly mineralised with pyrite along bedding plane
X= +17303 **Y= -6515** **Z=-1086.29**		TK-51-01B	Conglomerate	
	14.67-14.91	TK-51-02	Conglomerate	23 cm: poorly developed conglomerate, poorly packed and poorly sorted, black colour, sub-angular to rounded grains that are up to 25 mm, polymictic, carbon nodules present in matrix and on qtz granules, weakly mineralised as pyrite stringers
	14.91-15.18	TK-51-03	Quartzite	29 cm: very coarse grained quartzite, black colour, very few scattered qtz white qtz grains that are up to 15 mm, poorly sorted, angular grains, rounded carbon nodules, becomes finer grained from 14.5 - 29 cm, very weak pyrite mineralisation
	15.18-15.48	TK-51-04	Conglomerate	28.5 cm: 0-15.5cm=conglomerate that is poorly developed, poorly packed and poorly sorted, black colour, angular and elongated white qtz grains that are up to 20 mm, moderately mineralised with pyrite around qtz grains, minor fractures parallel to bedding. 15.5-28.5cm=quartzite that is very coarse to coarse grained, black in colour and weakly mineralised with pyrite along bedding
	15.48-16.76	TK-51-05	Conglomerate	30 cm: very coarse grained quartzite, black colour, few scattered white and grey qtz grains that are 12 mm, sorted, polymictic with chert grains, rounded and elongated grains, weakly mineralised with pyrite along bedding plane
	17.06-17.30	TK-51-07	Conglomerate	34 cm: not properly aligned but qtz granules are rounded and up to 20 mm with carbon nodules, well mineralised around qtz granules

	19.00-19.23	TK-51-08	Conglomerate	20 cm: 0-7.5cm and 14.5-20cm=quartzite is coarse grained, dark grey colour, sorted and mineralised with pyrite on bedding plane. 7.5-14.5cm=conglomerate that is poorly developed, poorly packed and poorly sorted, rounded to sub-angular grains that are up to 25 mm, polymictic, well mineralised with pyrite around qtz granules.
	21.53-21.78	TK-51-09	Conglomerate	27 cm: well developed conglomerate, packed, poorly sorted, black colour, rounded to sub-angular, grains are up to 27 mm, polymictic, carbon nodules in qtz granules, chert grains have fractures in them, mineralisation as pyrite stringers and around qtz granules
	22.23-22.55	TK-51-11A	Quartzite	36 cm: 0-7.5cm and 15-23cm and 25.5-36cm= quartzite that is coarse to medium grained, black colour, well sorted and very weakly mineralised. 7.5-15cm and 23-25.5cm=conglomerate that is poorly packed, poorly sorted, with rounded and angular grains up to 14 mm, polymictic, cracked qtz and chert granules, carbon nodules in qtz grains, changes to graphitic quartzite.
		TK-51-11B	Conglomerate	
	24.47-24.73	TK-51-12	Quartzite	27.5 cm: 0-14cm=conglomerate that is poorly developed, poorly packed, poorly sorted, black colour, sub-angular to angular and elongate white qtz grains that are up to 23 mm, mineralised with pyrite along bedding and around qtz granules. 14.5-27=quartzite that is medium grained, black colour, sorted, weak stringer pyrite mineralisation in bedding planes
	24.73-27.92	TK-51-13	Quartzite	20 cm: coarse grained quartzite, black colour, weakly mineralised with pyrite, 2.5cm thick conglomerate bed that is developed, packed, sorted, angular and fractured white qtz grains that are up to 18 mm, monomictic, well mineralised with pyrite as stringers
	26.36-26.62	TK-51-14	Conglomerate	29 cm: coarse grained quartzite, black colour, with qtz granules that are 32 mm, rounded and cracked, well packed and well sorted, weakly mineralised with pyrite
	28.00-28.27	TK-51-15	Quartzite	27 cm: very coarse grained quartzite, dark grey colour, scattered white qtz grains that are up to 21 mm, poorly sorted and angular, carbon nodules in qtz grain cracks, very well mineralised with pyrite grains ~5mm next to qtz granules.

	28.31-28.54	TK-51-16	Conglomerate	26.5 cm: well developed conglomerate, moderately packed, poorly sorted, black colour, elongate and rounded to sub-rounded white and grey qtz grains that are 27 mm, polymictic, fractured qtz granules some with carbon nodules in them, well mineralised with pyrite around qtz granules
	28.74-28.97	TK-51-17A	Conglomerate	24 cm: very well developed conglomerate, well packed, sorted, black colour, sub-rounded to sub-angular white qtz grains that are more than 34 mm, cracked qtz pebbles infilled with carbon nodules, very well mineralised with pyrite around qtz pebbles, pyrite is ~7mm
		TK-51-17B	Conglomerate	
	28.97-29.27	TK-51-18	Quartzite	30 cm: very coarse grained quartzite, black colour, scattered qtz and chert grains that are up to 32 mm, elongated, sub-rounded to sub-angular, polymictic, carbon nodules in qtz granules, well mineralised with pyrite as stringers close to qtz granules
	29.27-29.47	TK-51-19	Conglomerate	16.5 cm: very well developed conglomerate, well packed, poorly sorted, black colour, sub-rounded to angular qtz grains that are 24 mm, monomictic, some qtz granules are cracked in half and fractured half-way
	29.47-29.74	TK-51-21	Quartzite	25 cm: very coarse grained quartzite, black colour, few scattered rounded white and greyish-green grains that are 18 mm, polymictic, gradually fines to a graphitic shale with a sub-metallic lustre and black streak
	30.03-30.30	TK-51-23A	Conglomerate	28 cm: very well developed conglomerate, moderately packed, poorly sorted, black colour, sub-angular to sub-rounded gains that are up to 28 mm, monomictic, shows some carbon nodules as fluid movement, well mineralised with pyrite some on qtz granules
		TK-51-23B	Conglomerate	
	30.60-30.87	TK-51-25	Quartzite	23 cm: very coarse grained quartzite, black colour, few scattered white qtz grains that are 12 mm, monomictic, angular qtz grains, mineralised with pyrite as stringers on bedding plane
	30.87-31.17	TK-51-26A	Conglomerate	29 cm: 0-9cm=coarse grained quartzite that black colour, sorted, mineralised with pyrite as stringers. 9-20cm=conglomerate that is poorly developed, moderately packed, poorly sorted, rounded to sub-rounded white qtz grains with cracks and fractures and are up to 14 mm, monomictic, very well mineralised around qtz grains. 20-29cm=black shale interbedded with quartzite, black colour, black streak, very weakly mineralised along bedding plane

		TK-51-26B	Conglomerate	
	33.47-33.72	TK-51-27	Conglomerate	24cm: very well developed conglomerate, well packed, moderately sorted, black colour, clast supported, rounded to sub-angular white and dark grey grains that are more than 34 mm, polymictic, qtz pebbles have cracks, very well mineralised with pyrite around qtz and chert pebbles

BH ID	**Depth**	**Sample ID**	**Rock type**	**Sample description**
D8P04252	15.08-15.34	TK-52-09	Quartzite	18 cm: very coarse grained quartzite, dark grey, poorly sorted, few scattered white qtz pebbles that are angular and are up to 13 mm
X=+17303 **Y=-6515** **Z=-1086.29**	15.34-15.64	TK-52-10	Conglomerate	15 cm: poorly developed conglomerate, poorly packed, poorly sorted, matrix supported, dark grey, sub-rounded to sub-angular white and black grains that are up to 21 mm, polymictic, long black carbon nodule, moderately mineralised with pyrite
	15.64-15.93	TK-52-11A	Quartzite	32.5 cm: moderately developed conglomerate, well packed, poorly sorted, matrix and clast supported, black, sub-rounded to angular white and grey grains that are 27 mm, polymictic, qtz grains are rimmed and have cracks in them, very well mineralised around qtz grains
		TK-52-11B	Quartzite	
	15.93-16.16	TK-52-13	Conglomerate	22 cm: 0-11cm=coarse grained quartzite, black, sorted, weakly mineralised with pyrite. 11-22cm=well developed conglomerate, well packed, well sorted, clast supported, black, rounded to sub-angular grains that are up to 25 mm, monomictic, well mineralised with pyrite around qtz grains
	19.00-19.27	TK-52-14	Quartzite	29 cm: 0-14cm=coarse to medium grained quartzite, black, sorted, weakly mineralised with pyrite along bedding planes. 14-29cm=well developed conglomerate, well packed, well sorted, matrix supported, black, rounded white grains that are up to 35 mm, monomictic, has some dark greenish grey veinlet in matrix, moderately mineralised with pyrite around qtz grains

	19.27-19.54	TK-52-15	Quartzite	24 cm: 0-10cm and 21-24cm= medium grained quartzite, black, sorted, weakly mineralised with pyrite. 10-21cm=well developed conglomerate, moderately packed, poorly sorted, matrix supported, black, rounded to sub-rounded grains that are up to 30 mm, polymictic, very weakly mineralised with pyrite
	21.01-21.27	TK-52-16	Quartzite	30 cm: medium grading to coarse grained quartzite, black, very weakly mineralised with pyrite, interbedded with thin layers of shale and ~3cm thick conglomerate beds with sub-rounded 18 mm qtz grains, poorly sorted, poorly developed and is moderately mineralised with pyrite
	21.27-21.57	TK-52-17	Quartzite	29.5 cm: coarse to medium grained quartzite, black, moderately sorted, weakly mineralised with pyrite, few scattered white qtz grains that are rounded to sub-angular, 26 mm, with cracked and with carbon nodules in the cracks
	21.57-21.85	TK-52-18	Conglomerate	29 cm: 0-14cm=well developed conglomerate, well packed, well sorted, clast supported, black, well rounded to sub-angular white and black grains that are up to 35 mm, polymictic, qtz grains are cracked, rounded carbon nodules, well mineralised with pyrite around qtz granules. 14-28cm=coarse grained quartzite, black, moderately sorted, weakly mineralised
	21.82-22.09	TK-52-19	Quartzite	25 cm: 0-11.5cm=well developed conglomerate, well packed, well sorted, matrix supported, black, well rounded to sub-angular white and black grains that are up to 31 mm, polymictic, moderately mineralised with pyrite around qtz granules. 11.5-25cm=coarse grained quartzite, black, moderately sorted, very weakly mineralised
	22.22-22.50	TK-52-20	Conglomerate	25 cm: 0-3cm and 15-25cm=coarse grained quartzite, black, sorted, very weakly mineralised with pyrite. 3-15cm=poorly developed conglomerate, poorly packed, moderately sorted, matrix supported, black, sub-rounded to sub-angular white grains that are up to 23 mm, monomictic, well mineralised with pyrite around qtz granules
	26.24-26.44	TK-52-22	Quartzite	21 cm: coarse grained quartzite, black, sorted, weakly mineralised with pyrite. 8-15cm=poorly developed conglomerate, poorly packed, poorly sorted, matrix supported, rounded white qtz grains, very weakly mineralised
	28.12-28.37	TK-52-23	Conglomerate	41 cm: 0-5cm and 25-41cm=coarse to medium grained quartzite, black, sorted, very weakly mineralised with pyrite. 5-25cm=moderately developed conglomerate, well packed, moderately sorted, matrix supported, black, sub-rounded to sub-angular and elongate white, black and greenish grains that are up to 23 mm, polymictic, moderately mineralised with pyrite around qtz granules

	30.91-31.23	TK-52-24	Quartzite	31 cm: 0-11cm and 26-31cm=poorly developed conglomerate, poorly packed, poorly sorted, matrix supported, black, sub-rounded to sub-angular white and grey grains that are up to 30 mm, monomictic, cracked qtz granules, weakly mineralised with pyrite. 11-26cm=coarse grained quartzite, black, sorted, very weakly mineralised with pyrite
	32.33-32.58	TK-52-25	Conglomerate	25 cm: 0-9.5cm=coarse grained quartzite, black, sorted, well mineralised with pyrite in bedding planes. Gradational contact at 9.5-25cm=moderately developed conglomerate, moderately packed, poorly sorted, matrix supported, black, sub-rounded to sub-angular and elongate white and dark grey grains that are up to 30 mm, monomictic, moderately mineralised with pyrite around qtz granules and along bedding
	32.58-32.85	TK-52-27	Conglomerate	31 cm: 0-14cm and 16-31cm=poorly developed conglomerate, poorly packed, poorly sorted, matrix supported, black, sub-rounded to angular white and grey grains that are up to 20 mm, monomictic, cracked qtz granules, rimmed qtz grains, very well mineralised with pyrite in matrix around qtz grains and following bedding. 14-16cm=medium grained quartzite interbedded in conglomerate, black, sorted, coarsens to 31cm
	32.85-33.16	TK-52-28	Quartzite	27 cm: very coarse grained quartzite, dark grey, poorly sorted, very few 12 mm, angular qtz grains, weakly mineralised with pyrite.
	33.16-33.45	TK-52-29	Quartzite	42.5 cm: very coarse grained quartzite, dark grey, poorly sorted, very few 15 mm, angular qtz grains, weakly mineralised with pyrite.
	33.71-33.97	TK-52-30	Quartzite	27 cm: very coarse grained quartzite, black, poorly sorted, very few 13 mm, angular qtz grains, weakly mineralised with pyrite along bedding planes.
	33.97-34.24	TK-52-31	Quartzite	29 cm: very coarse grained quartzite, black, poorly sorted, very few 10 mm, angular qtz grains, weakly mineralised with pyrite.
	34.24-34.54	TK-52-32	Quartzite	25.5 cm: very coarse grained quartzite, dark grey, poorly sorted, interbedded with thin shale beds at partings where quartzite becomes medium grained
	34.89-35.18	TK-52-33	Conglomerate	28 cm: 0-6.5cm=coarse grained quartzite, black, sorted, poorly mineralised with pyrite in bedding planes. 6.5-25=8cm=well developed conglomerate, well packed, moderately sorted, matrix supported, black, sub-rounded to sub-angular white and dark grey grains that are up to 38 mm, monomictic, qtz granules have cracks in them and carbon nodules in the cracks, moderately mineralised with pyrite around qtz granules

	38-58-38.88	TK-52-35	Conglomerate	28 cm: 0-12.5cm and 19-28cm=poorly developed conglomerate, poorly packed, poorly sorted, matrix supported, black, sub-rounded to angular white and black grains that are up to 25 mm, monomictic, moderately mineralised with pyrite along bedding. 12.5-19cm=very fine grained quartzite to shale, black, graphite shiny lustre, mineralised with pyrite
	38.88-40.18	TK-52-36A	Conglomerate	25 cm: 0-20cm=poorly developed conglomerate, poorly packed, poorly sorted, matrix supported, matrix is a shale that has graphite with a black streak, black, rounded to sub-angular white and black grains that are up to 25 mm, polymictic, qtz grains have a black rim and also cracked and have wiggly fractures, well mineralised with pyrite grains that are ~2.5 mm and also around qtz granules. 20-25cm=coarse to medium grained quartzite to shale, black, graphite shiny lustre, mineralised with pyrite
		TK-52-36B	Shale	

BH ID	**Depth**	**Sample ID**	**Rock type**	**Sample description**
D8P04281	22.85-23.14	HM-81-01A	Conglomerate	36 cm: well developed conglomerate, well packed, moderately sorted, matrix supported, black colour, rounded to sub-rounded white and black grains that are up to 37 mm, polymictic, small scale fractures in qtz granules, some qtz granules infilled with carbon nodules, weakly mineralised with pyrite around granules
X=+17303 **Y=-6415** **Z=-1086.29**		HM-81-01B	Conglomerate	
	23.14-23.44	HM-81-02	Conglomerate	31 cm: moderately developed conglomerate, moderately packed, poorly sorted, matrix supported, black colour, rounded to sub-rounded white and black grains that are up to 40 mm, polymictic, fractured qtz pebbles on the edges, weakly mineralised with pyrite around qtz pebbles
	23.44-23.74	HM-81-03A	Conglomerate	52 cm: coarse grained quartzite, black matrix, sorted, interbedded with 2-3cm thick conglomerate beds that are poorly packed, moderately sorted, matrix supported, black colour, sub-angular to angular grains that are up to 15 mm, polymictic. Moderately mineralised with pyrite as stringers in bedding planes
		HM-81-03B	Quartzite	
	23.74-24.02	HM-81-04	Conglomerate	42 cm: poorly developed conglomerate, moderately packed, moderately sorted, matrix and clast supported, black colour, sub-rounded to sub-angular white and grey grains that are 32 mm, polymictic, fractures in qtz pebbles, qtz veins in matrix, qtz overgrowth seen, moderately mineralised with pyrite around granules

	24.02-24.30	HM-81-05	Quartzite	26.5 cm: 0-10cm=conglomerate that is poorly developed, poorly packed, poorly sorted, matrix supported, black colour, sub-angular white grains that are up to 20 mm, monomictic. 10-26.5cm=coarse grained quartzite, black colour, sorted, very weakly mineralised with pyrite
	24.30-24.60	HM-81-06	Quartzite	22.5 cm: very coarse grained quartzite, black colour, few scattered grey qt grains that are up to 11 mm, angular grains, very weakly mineralised with pyrite
	32.48-32.76	HM-81-07A	Conglomerate	43 cm: moderately developed conglomerate, poorly packed, moderately sorted, matrix supported, back colour, rounded to angular white grains that are up to 40 mm, polymictic, carbon nodules in cracks of qtz pebbles, weakly mineralised with pyrite and some in chert pebbles, 11-23cm=course to medium grained quartzite black, unsorted, very weakly mineralised
		HM-81-07B	Conglomerate	
	35.29-35.54	HM-81-08	Conglomerate	22 cm: well developed conglomerate, well packed, moderately sorted, clast and matrix supported, black colour, rounded white and dark grey grains that are up to 45 mm, polymictic, qtz pebbles are fractured, well mineralise with pyrite around qtz grains
	35.78-36.10	HM-81-09	Quartzite	24.5 cm: course to medium grained quartzite, black colour, few scattered white qtz grains that are sub-angular and have fractures in them, weakly mineralised with pyrite
	36.29-36.53	HM-81-10	Conglomerate	50 cm: well developed conglomerate, well packed, well sorted, matrix supported, black colour, polymictic, rounded and elongate white and black grains that are up to 43 mm, qtz pebbles have multiple fractures, moderately mineralised with pyrite around qtz pebbles
	36.57-36.78	HM-81-11	Conglomerate	34.5 cm: poorly developed conglomerate, poorly packed, poorly sorted, matrix supported, dark grey colour, sub-rounded to angular white, grey and black grains that are up to 42 mm, polymictic, fractures in qtz pebbles, very weakly mineralised with pyrite
		HM-81-12	Quartzite	20 cm: coarse grained quartzite, dark grey colour, some white qtz grains with fractures infilled with carbon nodules, very weakly mineralised
	37.22-37.46	HM-81-13	Conglomerate	37 cm: weakly developed conglomerate, moderately packed, poorly sorted, matrix supported, black colour, rounded to sub-angular white grains that are up to 30 mm, monomictic, moderately mineralised with pyrite around qtz granules
	37.58-37.78	HM-81-14	Conglomerate	40.5 cm: well developed conglomerate, well packed, moderately sorted, matrix supported, black colour, rounded to sub-angular grains that are up to 31 mm, polymictic, qtz granules have minor fractures, weakly mineralised with pyrite

	37.78-38.02	HM-81-15	Conglomerate	30.5 cm: poorly developed conglomerate, poorly packed, poorly sorted, matrix supported, black colour, rounded to sub-rounded white, grey and black grains that are up to 37 mm, polymictic, fractures in the qtz granules, very well mineralised with pyrite in the matrix and in qtz granules
	38.02-38.41	HM-81-16	Conglomerate	26.5 cm: 0-8cm=medium grained quartzite, black colour, very weakly mineralised with pyrite. 8-26.5cm=poorly develop conglomerate, poorly packed, poorly sorted, matrix supported, black colour, sub-angular white grains that are 20 mm, polymictic, qtz granules are fractured with carbon nodules infilling the fractures, well mineralised with pyrite following cross-beds
	38.76-39.07	HM-81-17	Quartzite	33 cm: 0-11cm and 24-33cm=medium to fine grained quartzite, black colour, moderately mineralised with pyrite parallel to bedding plane. 11-24cm=poorly developed conglomerate, poorly packed, poorly sorted, matrix supported, black colour, angular white and grey grains that are up to 35 mm, monomictic, well mineralised around qtz granules parallel to bedding
	40.35-40.59	HM-81-18	Quartzite	29 cm: course to medium grained quartzite, black colour, well sorted, weakly mineralised with pyrite, few scattered qtz grains that are white and up to 33 mm
	47.75-48.00	HM-81-19	Quartzite	31 cm: course to medium grained quartzite, black colour, weakly mineralised with pyrite, scattered white qtz grains that are up to 40 mm and have cracks along the grains and are rounded, the qtz grains have white spots in them
	48.18-48.45	HM-81-20A	Conglomerate	29.5 cm: 0-6.5cm=medium grained quartzite, lack colour, very weakly mineralised. 6.5-29.5cm=well developed conglomerate, moderately packed, poorly sorted, matrix supported, black colour, rounded to sub-angular white and black grains that are more than 45 mm, polymictic, some qtz pebbles have a black rim, some are cracked, some have carbon nodules in the pebbles, very well mineralised in matrix around pebbles
		HM-81-20B	Conglomerate	
	48.45-48.74	HM-81-21A	Conglomerate	41 cm: 0-32cm= course grained quartzite, black, mature, sorted, weakly mineralised with pyrite. 32-41cmmoderately developed conglomerate, poorly packed, sorted, matrix supported, black colour, angular to sub-rounded white grains that are up to 23 mm, monomictic, well mineralised with pyrite around qtz grains
		HM-81-21B	Quartzite	
		HM-81-22	Conglomerate	64 cm: moderately developed conglomerate, moderately packed, poorly sorted, matrix supported, black colour, sub-rounded to sub-angular white and grey grains that are up to 42 mm, polymictic, some qtz pebbles have a rim, very well mineralise with pyrite around qtz pebbles

BH ID	Depth	Sample name	Rock type	Sample description
D8P04299	11.80-12.13	HM-99-05	Conglomerate	33 cm: weakly developed conglomerate, top and bottom loaded, matrix supported, light grey, poor-moderately sorted, sub-rounded white qtz grains, moderately mineralised
X=+17636 **Y=-6154** **Z=-1030**	12.47-12.73	HM-99-07	Quartzite	26 cm: very coarse grained quartzite, light grey, poorly sorted, few scattered white qtz pebbles that are angular and are up to 9 mm
		HM-99-11	Conglomerate	
	18.39-18.66	HM-99-13A	Conglomerate	27 cm: poorly developed conglomerate, matrix supported, light grey, poor-moderately sorted, sub-rounded white qtz grains, moderately mineralised
		HM-99-13B	Quartzite	

BH ID	Depth	Sample name	Rock type	Sample description
D7P5047	37.00-37.14	TK-Sh-37A	Shale	14 cm: silty, light grey, dull lustre but occasionally shiny, no visible mineralisation
	37.14-38.97	TK-Sh-38A	Shale	183 cm: black shale, silty, dark grey to black, interbedded with quartzite (sand-sized grains), has multiple microfractures, pyrite mineralisation occurs along bedding planes
		TK-Sh-38B	Shale	
		TK-Sh-39C	Shale	
	45.85-46.98	TK-Sh-46A	Dolomitic Shale	113 cm: 48.85-46.31 cm = black shale, well mineralised with pyrite. 46.31-46.98 cm = grey shale, poorly mineralised, calcite veinlets that ate micro faulted
	46.97-47.87	TK-Sh-47A	Dolomitic Shale	46.97-47.39cm: grey shale, poorly mineralised, calcite veinlets that are micro faulted
		TK-Sh-47B	Dolomitic Shale	
		TK-Sh-47C	Dolomitic Shale	47.39-47.87cm: shale interbedded with mudstone, mineralised with pyrite along bedding plane
	49.29-49.90	TK-Sh-49A	Dolomitic Shale	61cm: very fine grain sand to silt sized grains, fracture that is filled with calcite vein
		TK-Sh-49B	Dolomitic Shale	

Appendix B: SEM images of ore minerals and carbon nodules

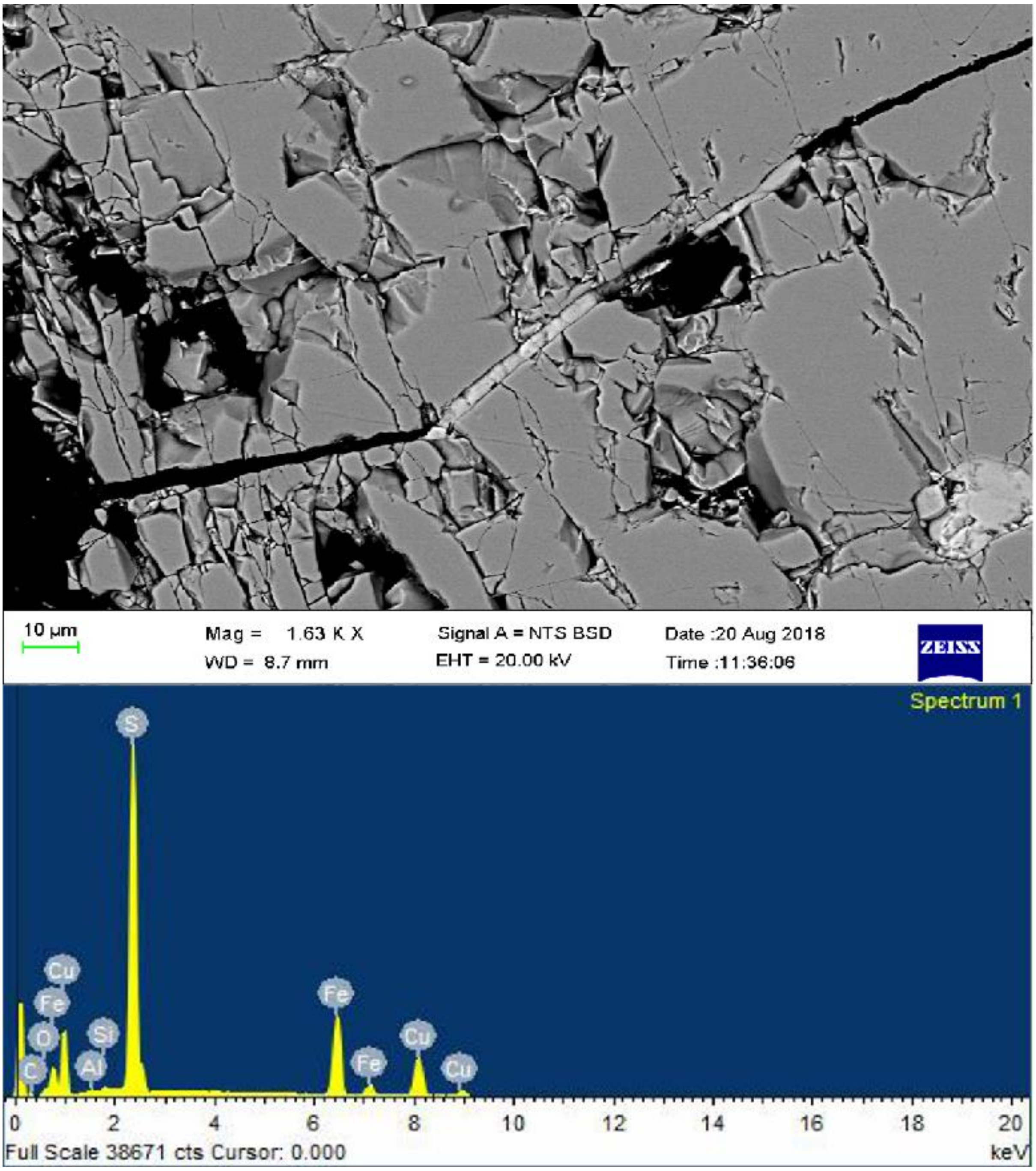

Chalcopyrite vein in a pyrite grain

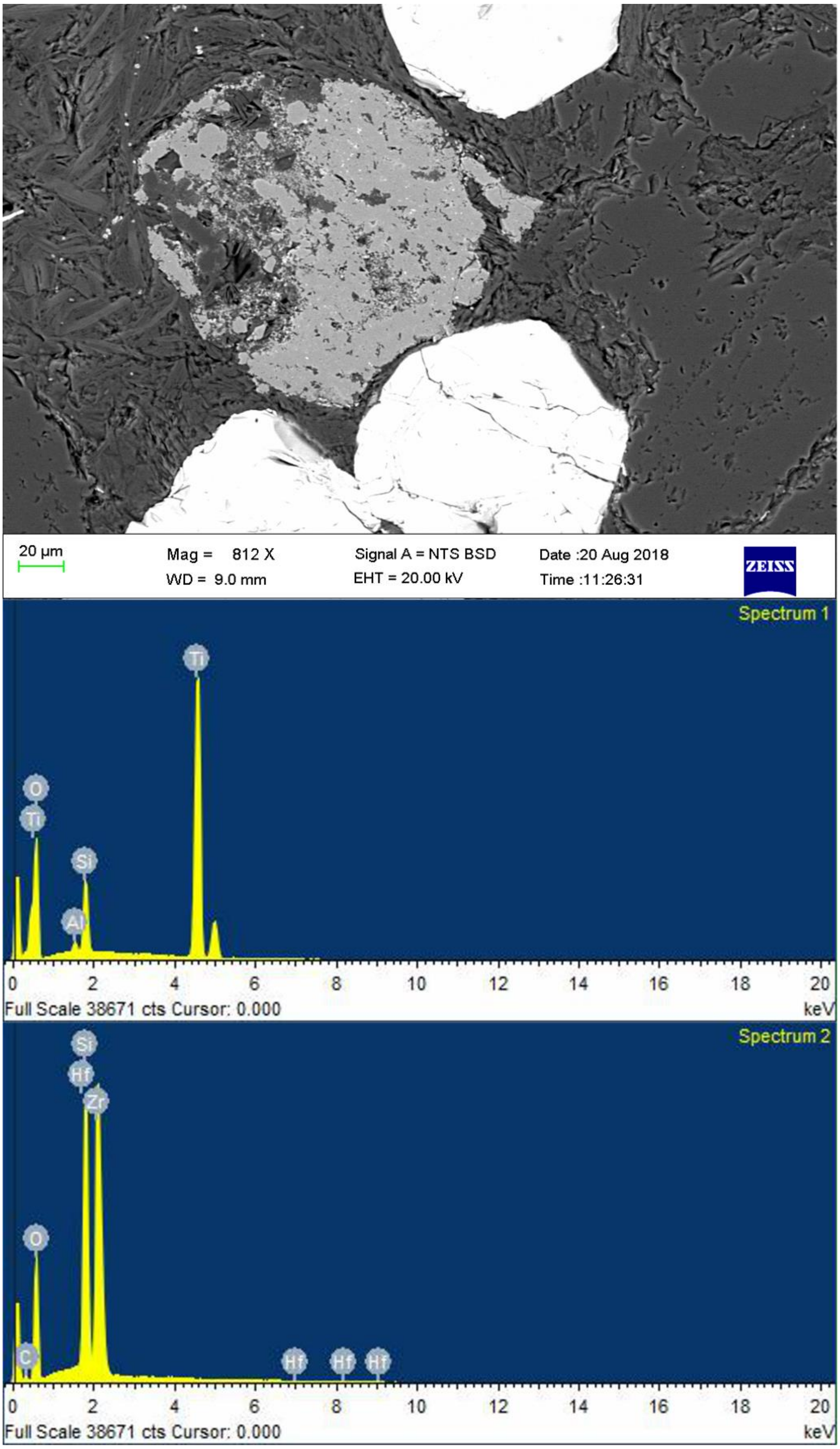

Rutile (medium phase) and zircon (bright euhedral phases) grains

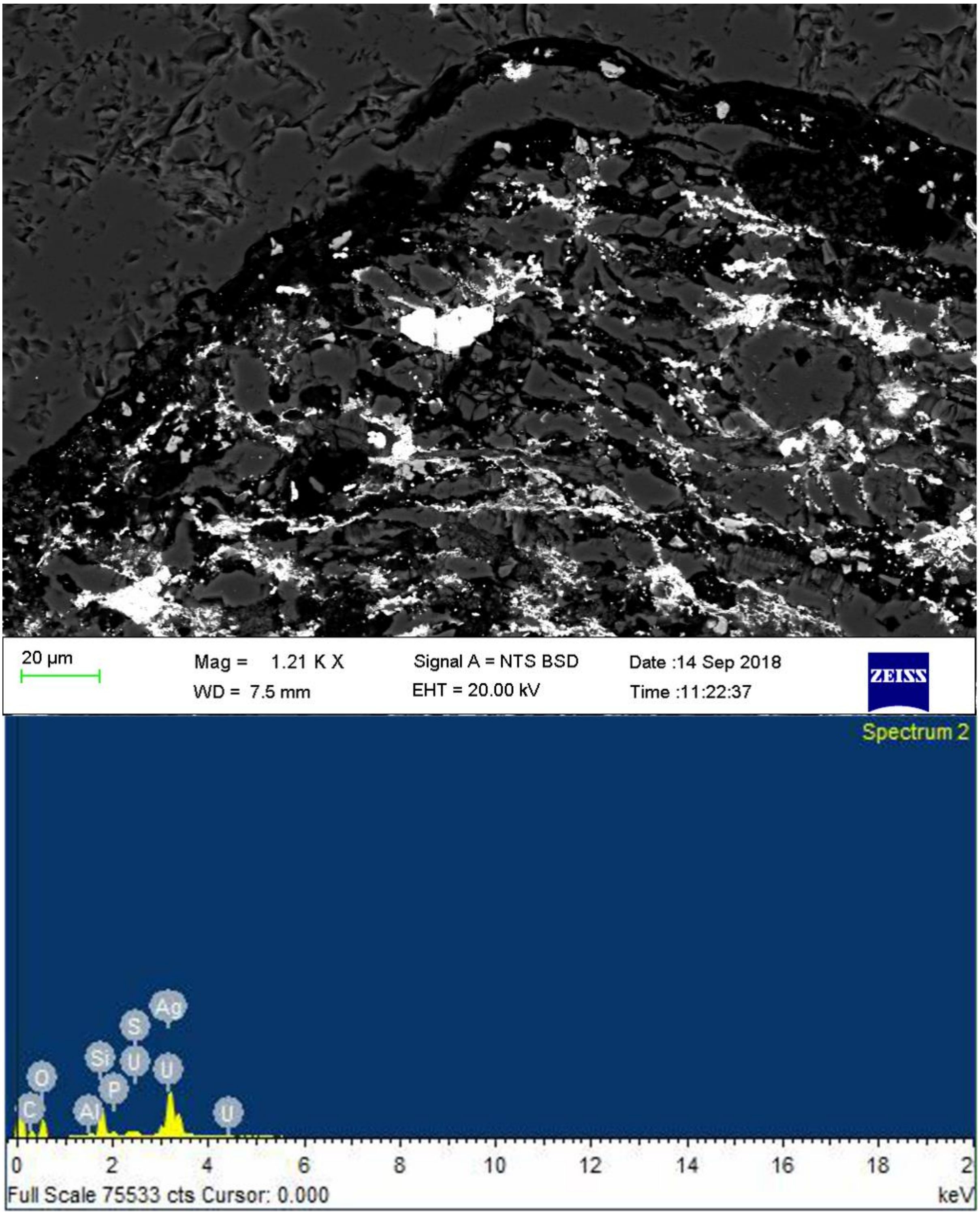

Carbon nodule with uranium- and silver-bearing phases

Appendix C: Microthermometry data

Sample ID	***Incl type***	***Av Size (μm)***	***T_{mf} (°C)***	***T_h (°C)***	***Salinity (wt% eNaCl)***	***Density (g/cm^3)***	***dP/dT (bar/°C)***
TK-52-25	I	20	-8.2	161.2	11.93	0.994	20.0
	I	5	-1.2	165.8	2.07	0.920	17.1
	I	10	-0.4	172.5	0.70	0.904	16.8
	II	10	-5	269.7	7.86	0.840	12.6
	I	7	-0.7	152.9	1.22	0.927	17.5
	I	5	-1.6	130.6	2.74	0.957	18.5
TK-52-19	I	15	-3.3	182.9	5.41	0.926	16.8
	I	12	-2.8	192.4	4.65	0.910	16.2
	I	5	-3.4	153.4	5.56	0.956	18.3
	I	7	-2.4	148.7	4.03	0.949	18.1
	I	3	-7.7	172.2	11.34	0.980	19.1
	I	2	-2.7	169.3	4.49	0.933	17.3
	I	10	-3.3	178.2	5.41	0.931	17.0
	I	10	-3.5	212.6	5.71	0.895	15.3
	I	15	-2.9	233.9	4.80	0.861	14.0
HM-81-05	I	25	-2.7	154.5	4.49	0.947	18.0
	I	20	-15.5	147.6	19.05	1.060	22.8
	I	10	-7.6	160.8	11.22	0.989	19.8
	I	8	-2.9	146.7	4.80	0.956	18.4
	I	15	-7.2	171.7	10.73	0.976	18.9
	I	8	-6.7	158.4	10.11	0.983	19.6
	III	17	-56.2	19.5	59.30	1.24	83.1
	I	10	-8.3	165.2	12.05	0.991	19.8
	I	9	-8.3	153.2	12.05	1.002	20.6
	I	12	-5.8	156.6	8.95	0.976	19.3
	I	7	-0.9	159.3	1.57	0.923	17.3
	I	5	-8	166.7	11.70	0.987	19.5
	I	8	-1.3	158.6	2.24	0.929	17.4
HM-81-08	I	11	-7.5	162.4	11.10	0.987	19.6
HM-81-14	II	5	-0.7	258.1	1.22	0.792	12.5
	I	5	-5.4	267.5	8.41	0.848	12.8
	I	5	-5.9	235.7	9.08	0.895	14.6
	I	10	-0.3	210.2	0.53	0.857	15.2
	I	7	-1	147.6	1.74	0.936	17.7
	I	13	-2.1	202	3.55	0.891	15.5
	I	8	-1.5	171.8	2.57	0.917	16.9
	I	15	-0.3	169.3	0.53	0.906	16.9
	I	5	-1.4	172.9	2.41	0.915	16.8

	I	3	-1.9	160.1	3.23	0.934	17.5
	I	8	-3.6	145.6	5.86	0.965	18.8
	I	5	-6.8	157.3	10.24	0.985	19.7
	I	7	-3.9	152.5	6.30	0.961	18.6
	I	6	-2.8	165.2	4.65	0.938	17.5
TK-51-02	I	7	-11.2	113.9	15.17	1.057	24.6
	I	3	-10.2	189.5	14.15	0.985	18.7
	I	10	-10.8	163.7	14.77	1.013	20.7
	I	8	-2.7	172.8	4.49	0.930	17.1
	I	13	-7.9	170	11.58	0.983	19.3
	II	19	-8.7	177.8	12.51	0.983	19.0
	I	7	-8.1	163.3	11.81	0.991	19.8
	I	4	-9.1	142.9	12.96	1.017	21.6
	I	15	-13.3	166.8	17.17	1.029	21.0
	I	10	-9.8	172	13.72	0.998	19.8
	III	20	-30	18	28.66	1.21	30.8
	I	8	-6.9	169.2	10.36	0.975	18.9
	I	4	-3.8	131.8	6.16	0.978	19.7
	I	10	-1	123.8	1.74	0.956	18.5
	I	11	-5.7	145.4	8.81	0.985	19.9
	I	8	-5.1	164.1	8.00	0.963	18.5
	I	4	-0.7	146.7	1.22	0.933	17.7
	I	9	-3.3	169.3	5.41	0.940	17.5
TK-51-18	I	16	-1.2	175.1	2.07	0.911	16.7
	I	10	-1	142.7	1.74	0.940	17.9
	I	6	-6.3	189.8	9.60	0.949	17.4
	I	15	-5.7	205.9	8.81	0.927	16.3
	I	13	-0.5	184.3	0.88	0.892	16.3
	I	15	-2.9	210	4.80	0.891	15.3
	I	5	-1.9	172.9	3.23	0.921	16.9
	I	6	-5.6	167.7	8.68	0.964	18.5
	I	4	-8.8	172	12.62	0.989	19.5
TK-51-27	I	12	-5.9	124.4	9.08	1.004	21.4
	I	7	-11.4	228.6	15.37	0.955	16.4
	III	10	-25.1	23.6	25.64	1.19	32.0
	III	5	-22.5	21.9	24.02	1.71	32.8
	I	4	-9.2	145.8	13.07	1.016	21.5
	I	7	-1.6	177.2	2.74	0.913	16.6
	I	8	-0.7	163.8	1.22	0.917	17.1
	I	6	-2.3	191.9	3.87	0.905	16.1

Appendix D: XRD graphs

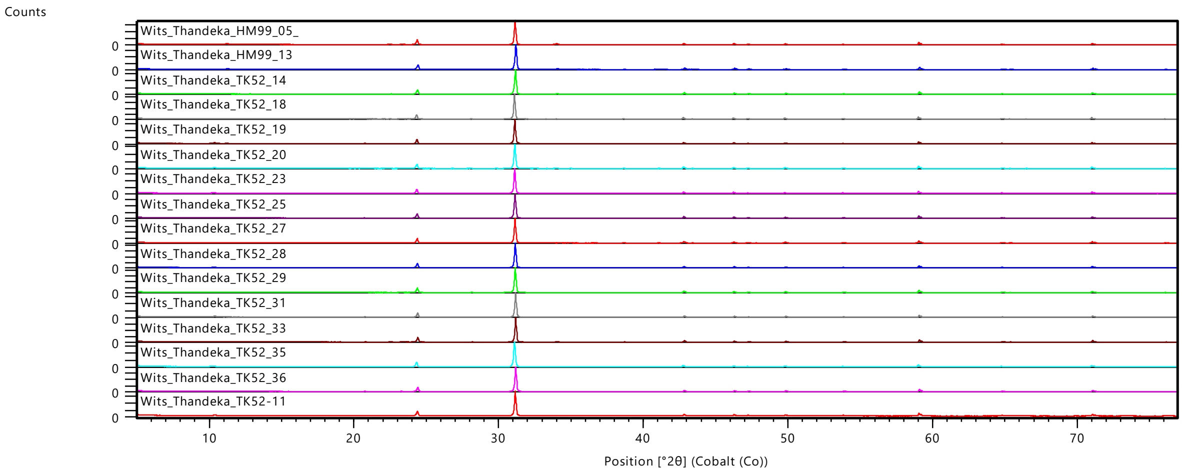

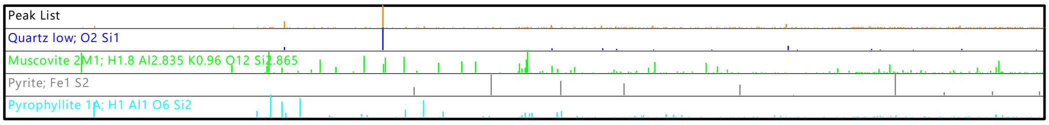

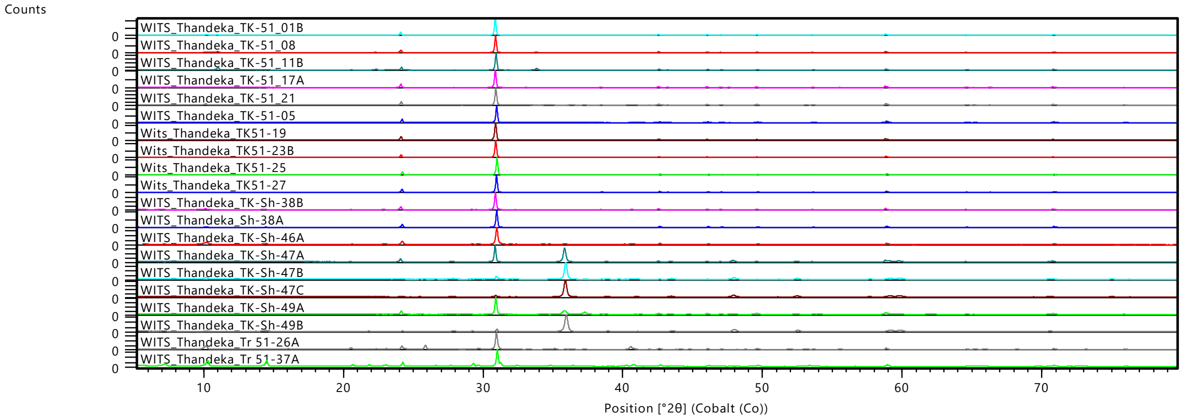

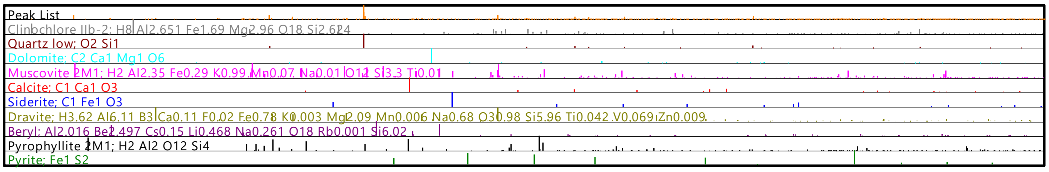

Appendix E: Major and trace elements

1. Major elements

Rock Type	Shale						
Sample ID	TK-SH-37A	TK-SH-38B	D8BRF001	D8BRF019	D8BRF003	D8BRF011	HM-81-17
SiO2 (wt%)	61.19	78.35	73.83	71.02	73.08	82.21	72.23
Al2O3	17.57	8.99	16.69	17.83	17.05	12.14	18.79
TiO2	0.79	0.48	1.41	0.91	0.85	0.58	0.70
Fe2O3 T	6.97	3.87	1.52	1.28	1.07	1.37	0.59
MgO	3.28	1.58	0.52	0.37	0.42	0.36	0.12
CaO	0.07	0.34	0.07	0.06	0.06	0.04	0.09
Na2O	0.04	0.02	0.23	0.29	0.25	0.22	0.90
K2O	5.22	2.75	5.13	5.5	5.3	3.64	4.00
P2O5	0.04	0.11	0.04	0.03	0.04	0.02	0.04
MnO	0.06	0.05					0.01
Total Organic Carbon (TOC)			0.84	1.08	1.28	0.74	
Total Sulphur (TS)			0.32	0.39	0.34	0.34	

Rock Type	Quartz arenite						
Sample ID	D8BRF007	D8BRF008	D8BRF012	D8BRF013	D8BRF014	D8BRF017	D8BRF018
SiO2 (wt%)	91.44	94.83	94.71	91.79	93.61	94.17	92.28
Al2O3	4.04	4.31	3.15	3.1	3.68	3.01	2.78
TiO2	0.17	0.19	0.1	0.12	0.14	0.14	0.12
Fe2O3 T	3.01	0.86	1.76	1.99	2.78	1.46	1.61
MgO	0.1	0.1	0.2	0.27	0.59	0.08	0.07
CaO	0.03	0.03	0.03	0.04	0.03	0.03	0.03
Na2O	0.09	0.12	0.1	0.08	0.07	0.1	0.08
K2O	1.26	1.39	0.96	0.91	0.89	1.02	0.91
P2O5	0.02	0.01	0.02	0.02	0.02	0.02	0.02
MnO	0.01		0.02	0.01	0.03		0.02
Total Organic Carbon (TOC)	0.24	0.18	0.14	0.14	0.33	0.14	0.15
Total Sulphur (TS)	1.73	0.22	0.15	0.28	0.14	0.34	0.29

Rock Type	**Quartz arenite**						
Sample ID	**TK52-27**	**TK52-28**	**TK52-29**	**HM81-12**	**HM81-18**	**HM99-05**	**HM99-13**
SiO2 (wt%)	92.64	93.63	93.17	92.04	90.79	90.22	91.43
Al2O3	2.35	2.95	2.53	4.59	5.45	5.93	4.83
TiO2	0.12	0.12	0.10	0.12	0.14	0.17	0.11
Fe2O3 T	1.72	0.93	0.87	0.69	0.66	0.94	0.76
MgO	0.04	0.05	0.05	0.02	0.03	0.04	0.02
CaO	0.04	0.04	0.04	0.06	0.05	0.04	0.04
Na2O	0.04	0.03	0.03	0.20	0.47	0.07	0.05
K2O	0.62	0.78	0.68	0.38	1.13	0.27	0.13
P2O5	0.02	0.02	0.02	0.02	0.02	0.03	0.03
MnO	0.01	0.01	0.01	0.01	0.00	0.01	0.01
Total Organic Carbon (TOC)	0.14	0.11	0.1			0.06	0.04
Total Sulphur (TS)	0.9	0.18	0.23			0.5	0.23

Rock Type	**Conglomerate**						
Sample ID	**TK52-11**	**TK52-14**	**TK52-18**	**TK52-19**	**TK52-20**	**TK52-23**	**TK52-25**
SiO2 (wt%)	83.87	88.96	89.62	84.07	83.89	84.53	88.72
Al2O3	5.34	5.30	3.75	10.25	7.83	6.66	4.41
TiO2	0.32	0.22	0.17	0.32	0.38	0.27	0.20
Fe2O3 T	4.49	2.20	2.55	0.63	2.96	3.52	2.20
MgO	0.05	0.03	0.02	0.05	0.04	0.06	0.07
CaO	0.06	0.05	0.04	0.06	0.05	0.05	0.04
Na2O	0.24	0.18	0.18	0.59	0.36	0.15	0.06
K2O	1.10	0.32	0.61	1.72	1.29	1.65	1.17
P2O5	0.06	0.03	0.03	0.03	0.03	0.03	0.02
MnO	0.01	0.01	0.01	0.01	0.01	0.01	0.01
Total Organic Carbon (TOC)	0.11	0.06	0.06	0.07	0.06	0.04	0.24
Total Sulphur (TS)	3.15	1.21	1.71	0.1	2.07	2.54	1.33

Rock Type	**Conglomerate**						
Sample ID	**TK52-31**	**TK52-33**	**TK52-35**	**TK52-36**	**TKSH-38A**	**D8BRF004**	**D8BRF021**
SiO2 (wt%)	83.37	89.65	85.26	85.94	88.21	88.11	88.11
Al2O3	8.49	4.54	7.16	5.21	3.74	8.03	6.09
TiO2	0.45	0.21	0.60	0.38	0.19	0.39	0.31
Fe2O3 T	1.86	1.93	1.50	2.27	2.15	0.94	1.35
MgO	0.15	0.03	0.14	0.21	0.69	0.21	0.19
CaO	0.05	0.05	0.04	0.05	0.89	0.03	0.04
Na2O	0.12	0.16	0.04	0.02	0.00	0.16	0.12

K2O	2.35	0.41	2.11	1.64	1.15	2.49	1.94
P2O5	0.03	0.04	0.02	0.03	0.04	0.02	0.02
MnO	0.01	0.01	0.01	0.01	0.05		
Total Organic Carbon (TOC)	0.54	0.18	0.45	0.37		0.63	0.24
Total Sulphur (TS)	1.06	1.21	0.81	1.22		0.24	0.44

Rock Type	**Conglomerate**						
Sample ID	**D8BRF002**	**D8BRF005**	**D8BRF006**	**D8BRF006**	**D8BRF010**	**D8BRF016**	**D8BRF020**
SiO2 (wt%)	90.12	90.46	92.61	86.26	91.5	89.9	88.41
Al2O3	4.5	2.37	2.69	5.45	1.96	2.76	5.76
TiO2	0.32	0.12	0.14	0.12	0.09	0.12	0.29
Fe2O3 T	1	3.2	3.27	6.41	3.49	5.23	2.81
MgO	0.13	0.15	0.31	0.08	0.26	0.14	0.12
CaO	0.04	0.03	0.04	0.03	0.03	0.03	0.04
Na2O	0.09	0.12	0.07	0.08	0.07	0.08	0.12
K2O	1.36	0.72	0.71	0.75	0.51	0.85	1.83
P2O5	0.03	0.02	0.02	0.02	0.02	0.02	0.03
MnO		0.01	0.01			0.02	0.01
Total Organic Carbon (TOC)	0.12	0.14	0.12	0.15	0.13	0.17	0.36
Total Sulphur (TS)	0.37	1.84	1.62	4.38	2.02	2.29	1.42

Rock Type	**Conglomerate**						
Sample ID	**HM81-01**	**HM81-02**	**HM81-03**	**HM81-07**	**HM81-09**	**HM81-15**	**HM81-20**
SiO2 (wt%)	89.65	87.7	89.33	89.74	89.86	79.34	82.45
Al2O3	6.03	5.9	6.5	5.74	6.48	5.55	8.95
TiO2	0.31	0.4	0.23	0.18	0.18	0.39	0.4
Fe2O3 T	1.81	2.79	1.07	1.39	0.66	8.78	2.96
MgO	0.06	0.06	0.05	0.04	0.03	0.06	0.08
CaO	0.17	0.1	0.08	0.1	0.09	0.07	0.07
Na2O	0.21	0.26	1.01	0.85	0.65	0.46	0.28
K2O	0.43	0.55	0.82	0.49	0.5	1.23	2.09
P2O5	0.07	0.03	0.04	0.03	0.02	0.06	0.05
MnO	0.01	0.01	0.01	0	0	0.01	0.01
Total Organic Carbon (TOC)							
Total Sulphur (TS)							

2. Trace elements

	Shale						
Sample ID	**TKSH-37A**	**TKSH-38B**	**D8BRF001**	**D8BRF019**	**D8BRF003**	**D8BRF011**	**HM81-17**
Rb (ppm)	76	88	114	106	115	72	116
Ba	139	134	311	99	248	201	214
Sr	7.615	13.186	35.5	37.7	32.1	30.3	216.211
Pb	2.916	14.756	16.4	31.3	24.1	25.5	7.167
Cs	8.061	6.96	3.6	4.1	3.7	2.7	5.326
Co	23.595	26.388	162.8	69.4	69.3	116.6	21.752
Cr	571.734	336.468	285	618	369	264	457.229
Cu	37	65	163	24	57	28	15
Ni	108	84	275	80	116	150	54
V	140	71	174	128	124	78	106
Sc	9.654	10.633	22	14	17	11	6.36
Sn	2.677	1.332	3	2	1	2	2.459
Zn	134.195	180.533	193	7	10	486	13.55
Ga	20.992	11.379	18.8	14.6	18.4	10.5	22.092
Zr	279.97	215.99	247	285	194	156	193.507
Nb	10.972	6.535	10.4	11.2	9.8	7.1	9.429
Hf	7.235	5.453	6.3	7.8	5.6	4.5	5.11
Ta	0.882	0.551	0.9	1	0.9	0.7	0.79
Tl			0.74	0.75	0.76	0.49	
Mo			5.3	16.7	2.4	2.6	
Th	3.665	4.251	7.8	8.9	8.1	6.1	3.885
U	2.603	2.304	12.6	23.6	26.9	14.1	12.25
W	1.655	1.209	2	3	1	1	1.174
Y	8.87	15.259	17.9	20.3	19.9	11.3	1.986
La (ppm)	21.322	20.745	33.7	41.1	34	32.4	11.144
Ce	36.744	36.603	67.3	84.1	66.3	61.6	43.379
Pr	4.307	4.32	6.9	8.9	6.7	6.2	1.843
Nd	16.489	17.711	25.5	31.6	23.4	21.1	6.692
Sm	2.5	3.565	5.5	5.9	4.8	4.3	1.198
Eu	0.606	0.88	1.1	1.1	1	0.8	0.314
Gd	2.369	3.809	4.2	3.5	4.6	2.8	1.398
Tb	0.285	0.488	0.5	0.6	0.6	0.4	0.101
Dy	1.618	2.923	3.7	3.4	3.3	2.2	0.467
Ho	0.334	0.585	0.7	0.7	0.7	0.4	0.093
Er	1.022	1.636	2.3	2.5	2.2	1.1	0.299
Tm	0.163	0.252	0.3	0.3	0.3	0.2	0.055
Yb	1.133	1.711	2.3	2.1	1.8	1.2	0.43
Lu	0.172	0.261	0.3	0.4	0.3	0.2	0.066
Au (ppm)			2.664	0.696	0.533	0.573	

Rock Type	Quartz arenite						
Sample ID	D8BRF007	D8BRF008	D8BRF012	D8BRF013	D8BRF014	D8BRF017	D8BRF018
Rb (ppm)	26	27	18	16	18	18	18
Ba	70	66	48	52	134	52	50
Sr	10.1	9.7	8.2	9.2	10.7	7.6	6.5
Pb	41.8	21.4	34.2	33.6	52.2	30.6	26.9
Cs	0.9	1.2	0.8	0.8	0.8	0.8	0.7
Co	112.5	40.8	41.2	51.4	50.7	32.8	28.6
Cr	155	79	64	538	93	444	74
Cu	53	28	40	85	41	22	25
Ni	128	61	54	66	89	44	37
V	21	29	11	54	30	52	17
Sc							
Sn	2	2	2	2	2	4	1
Zn	12	8	24	22	62	10	5
Ga	3.7	4	3.2	2.6	4	2.2	2.5
Zr	97	64	49	53	58	61	64
Nb	2.8	2.4	1.6	1.7	2.1	2.1	1.9
Hf	2.3	1.8	1.2	1.6	1.6	1.8	1.6
Ta	0.3	0.3	0.2	0.3	0.3	0.2	0.2
Tl	0.21	0.19	0.12	0.12	0.13	0.14	0.14
Mo	2.6	0.7	3.2	35.2	3.9	28.2	3.5
Th	4	2.3	1.9	2.1	2.4	2.1	2.2
U	24.7	5.1	4	6.2	5.8	6.7	5.6
W				4		3	
Y	7.7	6.7	3.7	4.5	7	4.6	4.3
La (ppm)	13.6	11.9	10.3	10.7	12	9.6	9.6
Ce	25	22.1	18.5	19.6	23	19.5	18.4
Pr	2.7	2	1.9	2	2.3	1.8	1.7
Nd	9	7.4	5.7	7	8.1	6.1	6.7
Sm	1.8	1.5	0.9	1.1	1.4	1.4	1.3
Eu	0.3	0.3	0.2	0.3	0.3	0.3	0.2
Gd	1.6	1.2	1.1	0.9	1	0.7	1
Tb	0.3	0.2	0.1	0.2	0.2	0.2	0.1
Dy	1.5	1.5	0.9	0.9	1.5	0.8	1.1
Ho	0.3	0.2	0.2	0.2	0.3	0.2	0.1
Er	0.9	0.5	0.3	0.6	0.7	0.5	0.4
Tm	0.1	0.1		0.1			
Yb	0.7	0.5	0.3	0.4	0.6	0.4	0.5
Lu	0.2	0.1	0.1	0.1	0.1	0.1	0.1
Au (ppm)	3.309	0.274	0.304	1.403	0.747	1.401	0.182

Rock Type	Quartz arenite						
Sample ID	**TK52-27**	**TK52-28**	**TK52-29**	**HM-81-12**	**HM-81-18**	**HM99-05**	**HM99-13**
Rb (ppm)	9	4	14	17	15	12	30
Ba	32	17	26	26	23	23	57
Sr	21.655	16.269	6.89	6.824	5.921	45.951	96.181
Pb	5.146	2.709	7.537	4.701	6.878	3.358	6.278
Cs	1.549	0.768	1.214	1.454	1.213	0.949	1.714
Co	19.631	6.686	31.719	8.326	13.033	9.603	9.081
Cr	96.04	52.884	101.271	60.503	54.818	84.242	69.553
Cu	17	37	15	10	31	22	13
Ni	50	18	41	15	18	21	25
V	22	15	10	12	11	20	20
Sc	4.328	2.911	2.093	2.257	2.098	4.1	3.941
Sn	1.028	0.593	0.524	0.501	0.507	0.505	0.847
Zn	9.91	23.436	12.715	6.65	6.784	8.636	12.901
Ga	6.679	5.371	2.352	2.877	2.597	5.064	5.764
Zr	81.61	55.561	104.432	69.886	71.341	78.068	65.027
Nb	4.212	2.193	2.35	1.972	1.554	2.309	3.984
Hf	2.361	1.681	2.855	2.026	2.007	2.266	1.879
Ta	0.5	0.294	0.332	0.239	0.226	0.205	0.421
Tl							
Mo							
Th	8.102	4.013	4.461	2.241	2.182	2.879	3.116
U	60.178	19.207	30.501	7.259	6.708	8.9	17.588
W	0.354	0.278	0.37	0.417	0.267	0.317	0.389
Y	9.324	5.006	5.467	3.885	4.058	6.77	5.557
La (ppm)	24.817	18.963	10.764	11.269	10.116	20.809	18.164
Ce	42.488	34.446	17.547	19.44	17.844	32.517	32.884
Pr	4.788	3.849	1.989	2.059	1.929	3.585	3.145
Nd	18.258	13.58	7.325	7.304	6.925	12.577	12.189
Sm	2.955	2.214	1.286	1.149	1.078	2.007	1.891
Eu	0.606	0.461	0.342	0.325	0.304	0.477	0.428
Gd	2.856	1.956	1.319	1.126	1.078	2.055	1.945
Tb	0.37	0.225	0.204	0.145	0.148	0.257	0.231
Dy	2.2	1.223	1.257	0.888	0.904	1.572	1.334
Ho	0.408	0.229	0.25	0.171	0.175	0.292	0.253
Er	1.181	0.675	0.693	0.499	0.515	0.806	0.834
Tm	0.182	0.095	0.105	0.071	0.078	0.119	0.108
Yb	1.165	0.599	0.669	0.494	0.512	0.743	0.693
Lu	0.164	0.088	0.103	0.074	0.08	0.116	0.103
Au (ppm)	2.01	0.257	0.884	0.314	0.303		

Rock Type	**Conglomerate**						
Sample ID	**TK52-11**	**TK52-14**	**TK52-18**	**TK52-19**	**TK52-20**	**TK52-23**	**TK52-25**
Rb (ppm)	32	9	16	37	33	39	27
Ba	73	21	27	54	48	61	48
Sr	149.227	41.044	45.815	78.863	69.352	18.442	12.511
Pb	14.929	3.945	4.936	3.319	5.901	15.122	9.296
Cs	2.288	1.098	1.226	2.664	2.275	3.147	2.092
Co	79.789	29.884	53.183	6.206	52.506	74.272	44.058
Cr	238.654	132.971	109.57	177.538	365.736	163.714	156.649
Cu	52	153	37	52	121	38	51
Ni	103	51	114	26	73	142	53
V	33	27	20	49	43	30	20
Sc	7.736	6.484	4.715	6.607	8.176	6.555	3.336
Sn	2.094	0.722	0.648	1.675	1.03	0.986	0.702
Zn	11.599	6.654	9.139	10.735	17.632	18.278	18.825
Ga	8.246	5.951	4.571	9.969	9.799	8.069	4.36
Zr	176.175	125.295	100.871	86.368	120.783	179.233	146.439
Nb	9.627	8.649	4.057	12.781	8.531	6.943	3.125
Hf	4.999	5.445	4.979	2.603	3.386	5.111	4.046
Ta	1.68	2.403	0.458	1.172	0.629	0.827	0.365
Tl							
Mo							
Th	18.026	7.204	6.717	3.526	9.241	18.164	5.727
U	88.62	20.961	34.606	5.174	41.593	129.359	46.907
W	0.853	0.512	0.451	1.202	0.808	0.676	0.684
Y	20.697	16	10.243	3.819	7.55	13.499	6.758
La (ppm)	88.774	27.951	20.532	8.078	27.649	36.607	20.642
Ce	153.259	44.641	35.26	32.65	54.079	65.03	35.604
Pr	17.997	5.104	3.973	1.689	5.601	7.485	3.946
Nd	65.544	18.928	14.753	6.199	20.477	27.745	14.402
Sm	10.392	3.292	2.644	1.117	3.308	4.984	2.381
Eu	1.494	0.725	0.511	0.261	0.728	1.17	0.571
Gd	9.638	3.764	2.887	1.212	3.088	4.642	2.312
Tb	1.109	0.573	0.414	0.14	0.384	0.652	0.305
Dy	5.655	3.587	2.521	0.905	2.016	3.726	1.742
Ho	0.979	0.716	0.473	0.178	0.375	0.69	0.335
Er	2.654	1.906	1.314	0.531	1.104	1.897	0.927
Tm	0.349	0.295	0.194	0.086	0.17	0.292	0.137
Yb	2.241	1.927	1.286	0.604	1.128	1.906	0.926
Lu	0.303	0.286	0.179	0.086	0.17	0.267	0.139
Au (ppm)			3.992	0.075	0.622	4.233	1.961

Rock Type	**Conglomerate**						
Sample ID	**TK52-31**	**TK52-33**	**TK52-35**	**TK52-36**	**TK-SH-38A**	**D8BRF004**	**D8BRF021**
Rb (ppm)	57	12	52	50	44	50	45
Ba	87	21	84	94	67	127	112
Sr	17.471	37.902	10.069	7.404	11.572	19.4	14.1
Pb	4.601	3.171	12.088	15.687	14.27	20.3	11.1
Cs	3.226	0.964	2.327	1.881	2.742	1.8	1.5
Co	29.401	26.762	33.807	42.265	14.036	109.7	187.5
Cr	236.153	164.275	283.164	627.859	101.921	185	426
Cu	13	57	9	34	57	45	91
Ni	35	46	48	57	43	135	245
V	49	30	50	43	29	57	72
Sc	9.083	5.68	9.337	10.126	5.795		
Sn	1.106	0.96	1.059	1.194	0.73	2	1
Zn	16.05	13.394	12.937	37.762	36.731	16	25
Ga	10.434	5.57	7.51	6.616	4.672	6.2	7.9
Zr	207.065	66.162	237.811	487.022	68.067	109	101
Nb	7.162	9.936	8.249	6.902	2.792	5.1	3.4
Hf	5.44	1.967	6.306	12.108	1.773	2.8	2.6
Ta	0.734	0.962	0.785	0.73	0.242	0.6	0.5
Tl						0.37	0.28
Mo						2.3	22.7
Th	4.314	5.806	3.436	9.264	2.055	4.3	3.2
U	14.61	20.121	9.708	43.648	0.891	8	14.2
W	0.929	0.924	1.13	1.272	0.41	1	3
Y	7.989	9.294	11.063	24.521	7.921	8.9	9.6
La (ppm)	15.984	24.991	15.223	19.236	10.662	23.1	12.7
Ce	29.559	42.342	27.429	33.178	17.793	44.1	24
Pr	3.06	5.104	3.042	3.967	2.162	4.4	2.3
Nd	11.83	19.437	11.679	15.395	8.845	15.3	9.7
Sm	1.986	3.14	2.196	3.424	1.646	3	1.6
Eu	0.612	0.639	0.549	0.87	0.413	0.5	0.3
Gd	2.053	3.06	2.043	3.889	1.809	1.8	1.7
Tb	0.253	0.377	0.287	0.633	0.246	0.2	0.3
Dy	1.513	2.054	1.963	4.55	1.468	1.9	1.7
Ho	0.309	0.371	0.403	0.963	0.289	0.3	0.3
Er	0.939	1.064	1.245	2.84	0.858	1	0.9
Tm	0.151	0.15	0.209	0.467	0.135	0.1	0.1
Yb	1.094	0.943	1.475	3.074	0.832	0.8	0.8
Lu	0.159	0.139	0.211	0.462	0.126	0.2	0.2
Au (ppm)	0.513	2.189	0.209	2.414		0.231	0.352

Rock Type	Conglomerate						
Sample ID	**D8BRF002**	**D8BRF005**	**D8BRF006**	**D8BRF006**	**D8BRF010**	**D8BRF016**	**D8BRF020**
Rb (ppm)	30	14	16	61	10	18	37
Ba	74	79	43	174	248	53	107
Sr	10.7	7.3	9	9.3	8.8	7.3	12.9
Pb	8.8	154.9	242.4	65.8	85.3	166.3	37
Cs	1	0.4	0.6	0.6	0.5	1	1.5
Co	146.3	123.6	104.1	119	211.9	124.6	102.5
Cr	90	121	156	155	164	194	209
Cu	53	126	195	51	75	148	113
Ni	194	118	121	109	239	131	119
V	38	28	26	21	11	21	28
Sc							
Sn			1	2	2	1	
Zn	21	108	60	31	32	29	5
Ga	4.7	2.1	2.7	2.2	1.6	3	6.2
Zr	82	67	75	102	99	128	139
Nb	4	1.4	1.7	1.9	1.8	1.8	3.9
Hf	2.2	1.5	1.9	2.7	2.7	3	3.6
Ta	0.5	0.3	0.3	0.3	0.3	0.3	0.4
Tl	0.2	0.14	0.15	0.2	0.13	0.19	0.28
Mo	1.2	1.7	1	2.3	2.6	4.4	3.3
Th	3.6	3.6	2.9	3	3	4.3	4.8
U	10.8	37.7	16.6	16.8	27.6	42.4	34.3
W							1
Y	6.7	5.5	5.2	5.5	4.9	6	10.4
La (ppm)	14.8	13.9	12.6	12.3	8.9	11.1	16.6
Ce	28.3	27.1	22.3	22.8	15.9	21	31.9
Pr	2.9	2.9	2.5	2.3	1.6	2.1	3.3
Nd	10.1	10.9	7.9	7.4	5.5	7.8	11.8
Sm	1.9	2	1.2	1.7	0.9	1.5	1.9
Eu	0.5	0.4	0.4	0.2	0.3	0.3	0.5
Gd	1.6	1.3	1.1	0.9	1.1	1.2	2.3
Tb	0.3	0.2	0.2	0.2	0.2	0.2	0.3
Dy	1.5	1.4	1	1.1	0.8	1.2	2.5
Ho	0.3	0.2	0.2	0.2	0.2	0.2	0.5
Er	0.8	0.7	0.6	0.7	0.5	0.7	1.1
Tm	0.1	0.1	0.1			0.1	0.2
Yb	0.7	0.5	0.6	0.5	0.5	0.6	1.2
Lu	0.1	0.1	0.2	0.2	0.1	0.1	0.2
Au (ppm)	0.55	11.452	2.634	2.941	7.425	6.244	5.059

Rock Type	Conglomerate						
Sample ID	HM81-01	HM81-02	HM81-03	HM81-07	HM81-09	HM81-15	HM81-20
Rb (ppm)	12.919	17.547	25.296	15.151	15.776	38.104	54.132
Ba	34.567	73.174	68.283	34.265	33.291	121.263	107.827
Sr	67.912	71.928	105.469	116.235	80.763	88.398	66.695
Pb	72.396	42.827	13.736	10.929	4.717	27.763	14.278
Cs	1.285	1.984	1.681	2.032	1.899	3.687	2.567
Co	43.992	45.075	24.979	97.721	6.527	178.58	71.296
Cr	108.787	150.32	138.851	118.233	106.284	337.011	221.79
Cu	80.025	38.339	34.539	174.805	6.331	103.899	38.686
Ni	103.587	77.882	48.049	194.042	13.953	283.496	85.943
V	30.95	31.107	27.649	24.165	30.254	35.484	44.286
Sc	8.4	7.055	5.827	5.06	5.357	9.58	6.633
Sn	1.193	1.274	0.935	0.848	0.879	1.639	1.466
Zn	14.389	19.413	10.937	18.935	5.377	50.019	25.76
Ga	7.689	7.887	7.926	6.202	7.476	7.45	10.129
Zr	155.605	120.313	94.44	101.219	70.786	270.66	140.01
Nb	9.909	5.094	5.028	3.023	4.116	14.689	6.758
Hf	4.277	3.431	2.595	3.187	2.016	7.833	3.979
Ta	0.874	0.761	0.401	0.306	0.252	3.015	0.609
Tl							
Mo							
Th	5.34	8.323	6.616	3.495	2.625	27.231	9.971
U	23.815	37.543	30.211	12.619	8.975	149.423	51.233
W	0.812	1.349	0.369	0.345	0.485	1.062	0.772
Y	23.488	10.092	8.826	9.78	7.134	25.22	10.455
La (ppm)	69.154	41.691	40.815	27.074	31.461	73.21	70.8
Ce	122.067	60.26	65.68	41.099	27.494	119.716	70.976
Pr	12.824	6.709	7.101	4.513	3.01	13.307	7.632
Nd	47	25.313	25.914	16.903	10.95	50.993	28.462
Sm	6.932	3.719	4.026	2.575	1.648	8.85	4.774
Eu	1.548	0.852	0.849	0.643	0.475	1.48	1.196
Gd	7.426	3.825	3.749	2.854	1.912	8.872	4.791
Tb	0.878	0.465	0.406	0.371	0.255	1.147	0.552
Dy	4.908	2.457	2.1	2.197	1.543	6.487	2.835
Ho	0.993	0.455	0.374	0.413	0.298	1.2	0.502
Er	2.898	1.318	1.059	1.163	0.873	3.342	1.412
Tm	0.44	0.184	0.149	0.173	0.131	0.473	0.208
Yb	2.83	1.185	0.956	1.208	0.811	3.048	1.292
Lu	0.434	0.183	0.147	0.167	0.127	0.429	0.182
Au (ppm)							

Appendix F: S-isotope data

Rock Type	**Sample ID**	**$\delta^{34}S$ ‰ (CDT)**
Carbonaceous shale	TK-Sh-37A	2.70
	TK-52-36B	Not enough Py
	HM-81-17	3.70
Conglomerate	HM-81-01	3.20
	HM-81-02	3.30
	HM-81-03	3.10
	HM-81-07	3.10
	HM-81-15	3.20
	TK-52-11	2.90
	TK-52-14	3.40
	TK-52-18	2.90
	TK-52-20	3.10
	TK-52-23	2.90
	TK-52-25	3.00
	TK-52-31	3.50
	TK-52-33	2.80
	TK-52-35	3.20
	TK-52-36A	3.50
Analytical Precision, 1σ		*0.20*